2011

Utilization of structural and biochemical cues to enhance peripheral nerve regeneration

Balendu Shekhar Jha
Virginia Commonwealth University

UTILIZATION OF STRUCTURAL & BIOCHEMICAL CUES TO ENHANCE PERIPHERAL NERVE REGENERATION

A dissertation submitted in partial fulfillment of the requirements for the degree of Doctor of Philosophy at Virginia Commonwealth University.

by

BALENDU SHEKHAR JHA

B.Sc. (Hons.) Physical Therapy, Delhi University, 2003.

Director: David G. Simpson, PhD

Associate Professor

Department of Anatomy & Neurobiology

Virginia Commonwealth University

Richmond, Virginia

August, 2011.

Acknowledgement

Earning a PhD degree is truly a marathon event, and I would not have been able to complete this journey without the aid and support of countless people over these years. I must first express my gratitude towards my advisor, Dr. David Simpson for his help and guidance. With his enthusiasm, inspiration, and great new ideas, he helped to make research work fun for me. I always considered him as Mr. Fixit. He has a solution to each and every problem, and can make sense out anything (literally any data). His way of seeing things and handling situations have set an example I hope to match someday.

I would like to express my appreciation to my committee members: Dr. Raymond Colello, Dr. Scott Henderson, Dr. Babette Fuss, Dr. Bob Diegelmann, and Dr. Gary Bowlin for their guidance towards completion of my bench work, and for the taking time for careful reading and commenting of my dissertation. Your expectations and concerns have always been right to the point.

This work would not have been possible without the constant assistance, guidance, and inputs provided by Dr. John Bigbee and Dr. Michael Fox. Both of them have been my regular consultants, training me how to interpret science.

I would like to thank the past and present Simpson lab fellows. Rusty Bowman has always been a second mentor after my advisor. I am sure he has a big brain with more than 50% hippocampus where he has a huge knowledge database stored. He has an answer to any question with statistical and demographic figures. I huge thanks goes out to Thomas Turner for being the fun guy in the lab, keeping the lab alive with his jokes and funny online videos; you kept things light and smiling. I would also like to thank Chantal Ayres for making me realize every now and then, that I should work in an organized fashion, keep the lab clean (glutaraldehyde-free), eat healthy and exercise regularly. A special thanks to Casey Grey for dealing with me every day now, and who has been always there for editing and proof-reading my work. Thank you for your encouragement, support, and most of all your humor.

I would like to thank all my friends; thank you for being the surrogate family during my years at the VCU and for your continued moral support.

Most importantly, I am forever indebted to my parents and my wife, Vandana for their understanding, endless patience and encouragement when it was most required. I would also like to thank my younger sister, Pragya for being there with my parents, and taking care of them when needed, in my absence during the course of my PhD training.

Table of Contents

List of Tables

List of Figures

Page

Page

List of Abbreviations

3D	Three-dimensional
ANOVA	Analysis of variance
BDNF	Brain-derived neurotrophic factor
BSA	Bovine serum albumin
CNTF	Ciliary neurotrophic factor
DRG	Dorsal root ganglion
ECM	Extracellular matrix
ELISA	Enzyme-linked immunosorbent assay
esC	Electrospun collagen
esG	Electrospun gelatin
FBS	Fetal bovine serum
FFT	Fast fourier transform
GAPDH	Glyceraldehyde 3-phosphate dehydrogenase
GDNF	Glial cell line derived neurotrophic factor
HDF	Human dermal fibroblasts
HFP	1,1,1,3,3,3-hexafluoro-2-propanol
MEM	Minimum essential media
N-CAM	Neural cell adhesion molecule
NGF	Nerve growth factor
PBS	Phosphate buffered saline
PCL	Poly-ε-caprolactone
PGA/PLA	Polylactic acid / Polyglycolic acid
PNS	Peripheral nervous system
rEC	Recovered electrospun collagen
rEG	Recovered electrospun gelatin
RGD	Arginine-glycine-aspartate
SDS	Sodium dodecyl sulfate
SEM	Scanning electron microscopy
SFI	Sciatic functional index
TEM	Transmission electron microscopy
TFE	1,1,1-trifluoroethanol
TGF	Transforming growth factor

Abstract

UTILIZATION OF STRUCTURAL & BIOCHEMICAL CUES TO ENHANCE PERIPHERAL NERVE REGENERATION.

By Balendu Shekhar Jha, PMP, PT

A dissertation submitted in partial fulfillment of the requirements for the degree of Doctor of Philosophy at Virginia Commonwealth University.

Virginia Commonwealth University, 2011

Major Director: David G. Simpson, Ph.D.
Associate Professor, Department of Anatomy and Neurobiology

This study examines the prospects of using the electrospinning process to fabricate tissue engineering scaffolds targeting a variety of regenerative applications, with a primary focus on the production of nerve guides for the treatment of long-defect nerve injuries in the peripheral nervous system. A basic overview of the conventional electrospinning process is provided, and the utility of this fabrication scheme in the production of collagen-based tissue engineering scaffolds is demonstrated. Next, a novel modification of the basic electrospinning process is

presented. This process, called two pole air gap electrospinning, was developed to produce nerve guides that exhibit an anisotropic structure that mimics the extracellular matrix of native peripheral nerve tissue. This electrospinning process makes it possible to produce macroscopic nerve guides that are cylindrical in shape and composed of dense arrays of nano- to micron-scale diameter fibers. Unlike, conventional hollow core nerve guides, these electrospun constructs lack a central lumen, hence the designation 3D (for three-dimensional) nerve guide. The fibers are nearly exclusively arrayed in parallel with the long axis of the construct. This architectural feature provides thousands of individual channels, and aligned fibers that provide guidance cues that are designed to drive regenerating axons to grow in a highly directed fashion down the longitudinal axis of the guide. To supplement the structural cues provided by the fibrillar arrays of the electrospun 3D nerve guides, an alginate-based platform designed to deliver therapeutic reagents was developed and characterized. This platform makes it possible to fabricate gradients of therapeutic reagents within the fibrillar arrays of an electrospun nerve guide. Functional and structural analyses of these constructs supplemented with or without a gradient of NGF, in a long-defect nerve injury in the rodent sciatic nerve indicate that the 3D design is superior to the gold standard treatment, the autologous nerve graft. Animals treated with the 3D grafts recovered motor and sensory function faster and exhibited far higher nerve-to-nerve and nerve-to-muscle signal amplitudes in electrophysiological studies than animals treated with autologous grafts or conventional hollow core cylindrical grafts.

CHAPTER 1

Chapter 1. Overview

The central hypothesis of this study states that tissue regeneration after injury can be maximized by identifying and recapitulating key features of the native extracellular matrix (ECM) [1]. In this study the central role that scaffold structure and composition play in the tissue engineering paradigm is explored. Tissue engineering is an evolving multidisciplinary field that has the potential to revolutionize medical practice and improve the health and quality of life for millions of people worldwide by restoring the structure and function to diseased or damaged tissues and organs. As a science, tissue engineering encompasses a broad range of potential applications including the repair, augmentation, or replacement of body tissues such as bone, muscle, skin, blood vessels, nerve, cartilage, and other connective tissues such as ligaments and tendons. Fundamental to nearly all tissue engineering processes is the scaffold used to establish the three-dimensional space necessary for cell attachment and growth at the injury site [1]. Typically, these scaffolds biodegrade or integrate themselves into the host tissue as the nascent ECM regenerates at the injury site. In effect, the scaffolds represent a template that act to guide the regenerative process and in most applications these structures are designed to be remodeled and completely replaced by native tissues. These scaffolds may or may not be supplemented with various types of cells designed to promote the reconstitution of functional tissue.

A primary assumption of the tissue engineering paradigm is the notion that functional tissue will develop if the proper biological, guidance and or positional cues are provided by the tissue engineering scaffold [1]. It is becoming increasingly clear that each specific tissue requires its own unique set of these signals. The cues to be used in any specific application may be driven by biological, clinical, commercial and / or regulatory considerations. In the example of

peripheral nervous tissue, it may be guidance and / or positional cues that are paramount in design of the regenerative template. Superimposed on these basic considerations are the processing limitations that limit the ability to fabricate different materials into scaffolds with the features suitable to function as a regenerative template for the reconstruction of organs and tissue.

Tissue engineering scaffolds, fabricated by the process of electrospinning, can be produced with fibers that closely resemble the size range of fibrils found in native ECM [1], and thus, have been presented as a potential avenue to the development of physiologically relevant scaffolds for the fabrication of tissue engineered organs and tissues, wound dressings, and drug delivery platforms. Electrospun polymers, natural, synthetic, and blends of natural and synthetic polymers, have been explored as tissue engineering scaffolds [1]. This study will examine how the composition and architecture of electrospun materials interact to define the functional properties of this unique class of nano-materials.

Chapter 2 of this thesis provides a primer to the fundamentals of the electrospinning process. This chapter examines how the electric field effect is exploited in the fabrication of electrospun scaffolds. Chapter 3 provides a consideration of how the molecular organization and composition of a scaffold interact to dictate its biological and functional properties. This chapter was published as a review [1], and represents the culmination of several studies and specifically describes the use scaffolds produced from electrospun collagen in various tissue engineering applications. The results presented in this particular paper underscore the critical roles that scaffold composition and the molecular organization of electrospun fibers of collagen, play in many tissue engineering applications.

Chapter 4 is also a published manuscript, and it describes the use of a novel electrospinning strategy called two pole air gap electrospinning that was developed in our laboratory to produce scaffolds that mimic the anisotropic structure of the native ECM present in peripheral nerves [2]. In this tissue engineering application, the development of a regenerative scaffold with potent guidance cues, sufficient material strength, and the appropriate architectural features is critical to the success of any implant used to reconstruct a damaged segment of peripheral nerve. This manuscript is a comprehensive analysis of the variables that impact the alignment of electrospun fibers in the two pole air gap electrospinning system. Preliminary *in vitro* and *in vivo* observations reported in this chapter provide evidence that scaffolds produced by this electrospinning process recapitulate key architectural features of the native sciatic nerve and are very efficient at supporting the regeneration of damaged peripheral nerve.

Chapter 5 discusses the development of a sustained release platform for the delivery of growth factor gradients within a nerve graft. In long gap nerve injuries bridged with a nerve guide, neurotrophic factors and various biochemical cues released from the cells present in the native tissues adjacent to the implant site may be insufficient to fully drive regeneration. This is especially true in the rodent sciatic nerve after introducing a 15 mm gap in this tissue; the remaining nerve stumps adjacent to the injury site are quite small in area in comparison to the area of the implanted graft. The alginate delivery system described in Chapter 5 was developed to overcome this potential limitation. The alginate polymer can be polymerized and used to trap therapeutic reagents; this carbohydrate is highly biocompatible and can be fabricated into a variety of shapes and configurations. It undergoes gradual dissolution under physiological conditions, making it suitable for use as carrier for the sustained release and delivery of growth factors and other therapeutic reagents at precise locations.

Chapter 6 is a study that builds on the results reported in Chapter 4. It provides a more in depth analysis of the grafts produced by two pole air gap electrospinning in the reconstruction of peripheral nerve injuries. This study compares the efficacy of this unique design with respect to the performance of autologous grafts and the more classic hollow core graft design presently in clinical use. In this comparative study, the 3D nerve guides characterized in Chapter 4 are supplemented with or without a gradient of Nerve Growth Factor (NGF) using the alginate system discussed in Chapter 5. A battery of functional and structural metrics is used to evaluate the performance of each graft design.

The discussion provided in Chapter 6 synthesizes the results of the individual chapters presented in this thesis into a coherent whole and discusses some potential avenues for future research.

CHAPTER 2

Chapter 2. Introduction to Electrospinning

ELECTROSPINNING PROCESS

Electrospinning is a non-mechanical process that uses an electrical field to induce the formation of nano- to micron-scale diameter fibers from a charged polymer solution or a polymer melt [3-5]. In practice, fibers produced by electrospinning are targeted to deposit onto an oppositely charged target or collector to form a scaffold. Figure 2.1 illustrates a schematic of the process of electrospinning.

In a typical bench scale electrospinning setup, a polymer solution is placed into a syringe that has been installed into a syringe pump. While in many electrospinning systems, the pump is not necessary, one is usually used to promote more uniform fiber formation through the constant delivery of material to the tip of the electrospinning needle [6]. The electrospinning needle, usually blunt tipped, is attached to an electrode of a high voltage power supply (for this thesis, unless mentioned, it will be assumed that the needle is attached to the positive electrode, as in the illustration on the next page). The negative electrode is attached to a collecting surface (or placed behind a collecting surface in some cases). Electrospinning voltages vary with the polymer and solvent system to be processed, in routine spinning, 16-22 kV is a commonly used range of voltages [3-7].

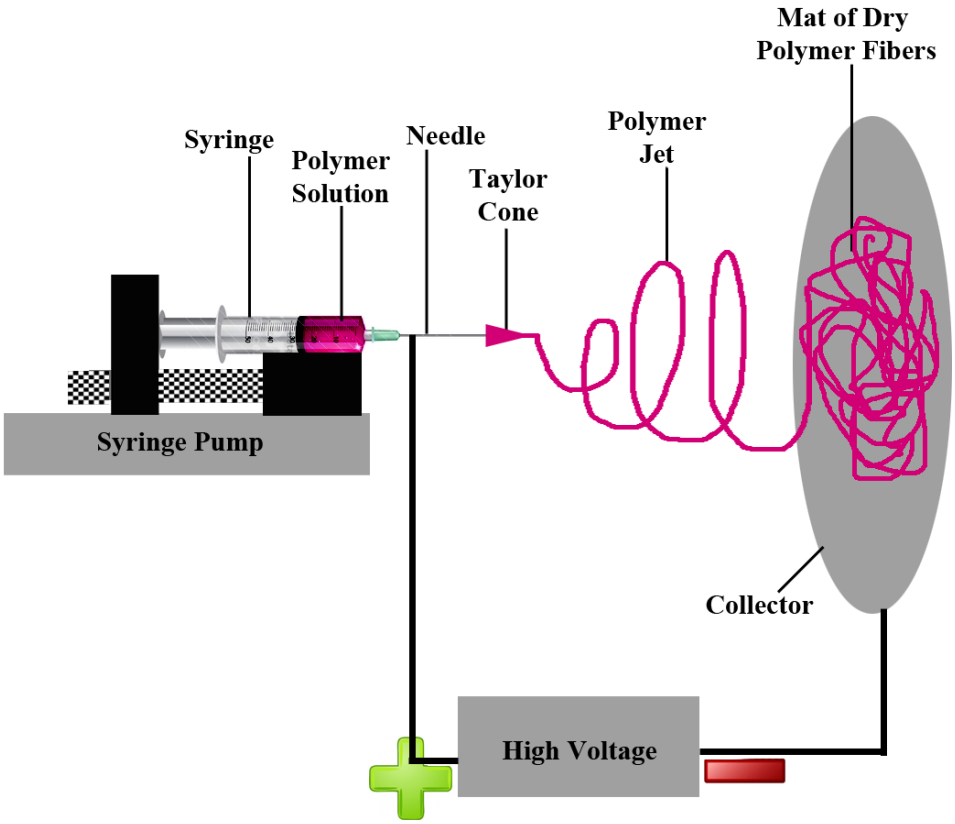

Figure 2.1: Schematic of the process of electrospinning. In this image, the polymer solution in the syringe is positively charged with a high voltage, low amperage power supply. The injection of this charge leads to formation of a liquid jet that dries to form fibers which are deposited onto a negatively charged collector. The nature of the polymer(s) to be spun determines the polarity of the system.

In electrospinning, there are three forces that can be identified acting on the polymer solution at the tip of the needle: (i) the surface tension of the polymer solution which holds the solution at the tip of the needle in a spherical shape; (ii) the viscoelastic forces of the polymer solution; and (iii) Coulomb forces of charge repulsion which originate with the positively charged ions in the polymer solution. As noted, surface tension tends to give the polymer solution a spherical shape at the tip of the needle. The electrostatic Coulombic forces counter the surface tension to some extent and distort the spherical shape of the polymer drop at the needle tip, thereby increasing the surface area of the droplet [3, 7].

When an electric charge is injected into the polymer solution via the positive electrode placed onto the needle, the stray ionic charges present in the solution are neutralized (*e.g.* injection of a positive charge neutralizes negative ions). With the application of increased electric potential the Coulombic forces begin to dominate the surface tension forces and the polymer droplet collapses to assume a conical shape, this structure is referred to as the Taylor cone [8, 9]. Once the electrostatic forces exceed the surface tension forces, a jet of the polymer solution is ejected from the tip of the syringe and towards the grounded target. In the theoretical electrospinning setup under discussion, the electric potential created by the negatively charged collector that is placed in front of the positively charged needle attracts the positively charged polymer jet. Viscoelastic forces, which are a product of the polymer chain entanglements present in the electrospinning solution, resist the distorting electrostatic force and serve to maintain a smooth continuous polymer jet [9]. As the jet travels to the collecting target the solvent evaporates and a fiber is formed, the fiber deposits on the surface of the collector in the form of a non-woven mat [3, 7, 9].

The configuration of the grounded target array determines the gross architectural organization of the resulting scaffold. Simple to complex shapes can be produced in a seamless fashion. For example, if the ground target is stationary flat surface the spun fibers will collect on that surface as a flat sheet. Spinning onto a slowly rotating mandrel can be used to produce cylindrical and or rectangular constructs. As the rate of rotation of these targets is increased varying degrees of fiber alignment in can be induced in the spun scaffolds [10, 11]. Overall, the electrospinning process is directly related to the more familiar electrostatic painting processes used in many industries, such as processes used in the automobile industry to paint car bodies. The fundamental difference lies in the use of polymers with chain entanglements that result in the formation of a fiber instead of a charged droplet.

The forces that dictate the path of the polymer jet from the needle tip to the collector play a critical role in fiber formation and the pattern in which they deposit onto the ground target. At electrostatic equilibrium, the electric field inside a conducting fluid is zero. Once sufficient charge has been injected into an electrospinning system to form a Taylor cone and a charged jet, the Coulombic repulsion forces within the jet cause the like charged ions to radiate towards and against the surface of the jet [9], as shown in Figure 2.2A.

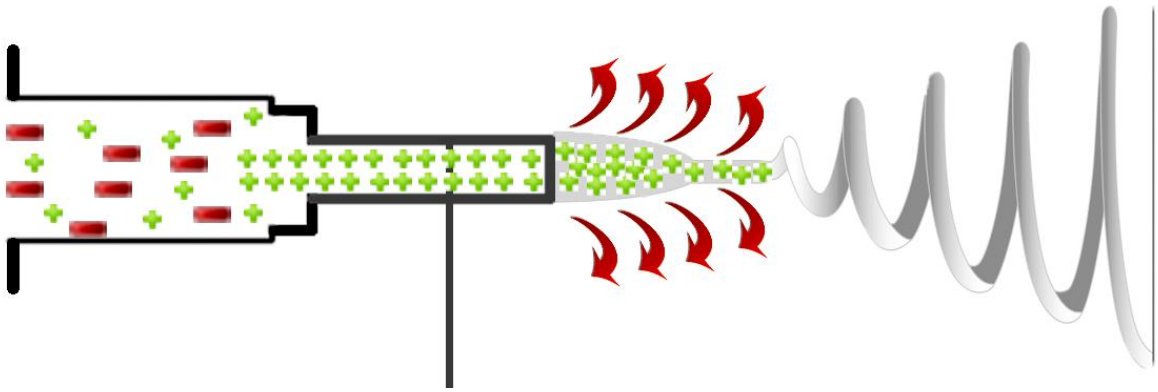

Figure 2.2A: Effect of Coulombic repulsion forces. The injection of a positive electric charge into the syringe of an electrospinning system neutralizes the negative ions present in a polymer solution. This leads to a charge imbalance and the formation of Coulombic repulsive forces. The Coulombic forces cause the positively charged ions to migrate towards the surface of the polymer solution, once sufficient force is present to overcome the intrinsic surface tension of the solution a charged jet is formed and ejected from the syringe tip.

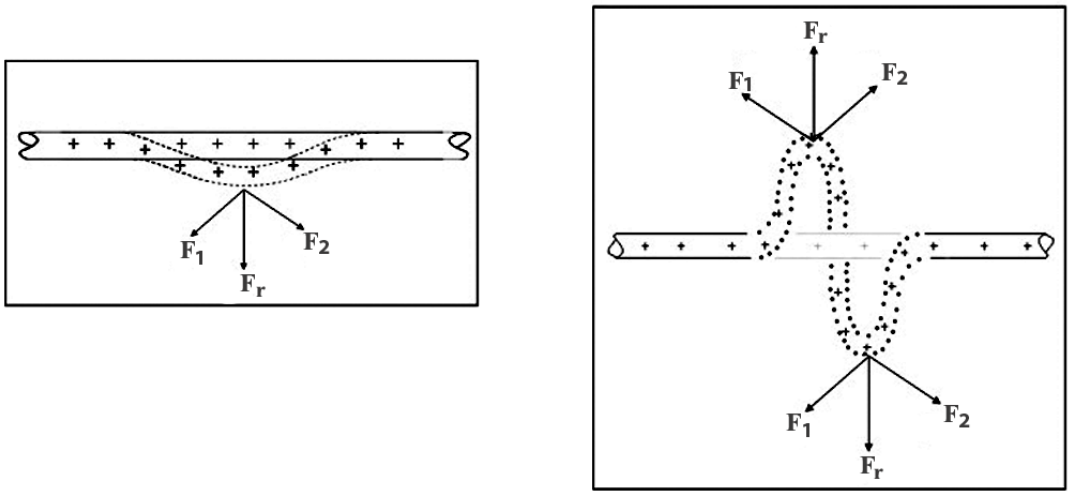

Figure 2.2B: Coiling of the electrospun jet. As the charged polymer jet travels some distance away from the needle tip, its diameter decreases because of drying. This leads to an increased concentration of the repulsive ionic charge forces (F_1, F_2, F_3, and so on) inside the polymer jet. The net resultant repulsive force (F_r) is in the direction perpendicular to the orientation of the jet. The cumulative effect of these perpendicular perturbations results in fiber coiling, fiber whipping and fiber elongation. *(Adapted from Reneker and Yarin, 2008* [9]*.)*

As the charged jet travels away from the Taylor cone, its diameter decreases because of the simultaneous effects of the jet stretching against the surface tension and the evaporation of the electrospinning solvent [3]. This decrease in jet diameter further increases the repulsive charge density. After a small straight segment, bending perturbations and many other forces leading to instabilities [9] result in the formation of polymer jet. As shown in Figure 2.2B, there are many repulsive forces in the jet in varied directions (F_1, F_2) with the resultant summation of all the forces F_r, being in the radial direction to the straight jet [9]. This radial force ultimately results in a three-dimensional coiled trajectory of the jet with the coil diameter growing larger as the jet moves away from the Taylor cone. This process is largely driven by the increased charge density associated with the constantly decreasing jet diameter. Reductions in jet diameter are produced though the processes of solvent evaporation and fiber stretching. Together, these forces result in the formation of nano- to micron-scale diameter fibers.

Motion along the straight axis of the trajectory from the Taylor cone towards the collector is driven by the potential difference between the positively charged needle tip and the negatively charged or grounded collector. After several turns of the coiled trajectory, the elongation stops, usually as a consequence of the solidification of the polymer fiber jet. The position where solidification occurs, essentially "flash-lyophilization", largely determines the placement of the collector on which non-woven mat / scaffold of polymer fibers are to be deposited. Placing the collecting target in a position where it collects the charged polymer jet prior to its solidification process results in the deposition of wet fibers and solvent welding (partial melting of fibers against one another).

REGULATING ELECTROSPINNING – TWEAKING ITS VARIABLES

The morphology and diameter of an electrospun fiber is modulated by a variety of electrospinning parameters, including the intrinsic properties of the polymer solution, the electrospinning setup, and environmental variables.

The intrinsic properties of a polymer include the polymer concentration and the viscosity of the solution, the extent of chain entanglements, the surface tension of the solvent/polymer solution, and overall electrical conductivity of the solution (or melt). In practice, the relationship between polymer concentration (solution viscosity which increases with polymer concentration) and fiber diameter is relatively simple. At very low polymer concentrations, i.e. below the electrospinning threshold, aerosol droplets will form in the electrospinning field. As the concentration of polymer increases the droplets transition into fibers; increasing the polymer concentration still further will result in ever larger diameter fibers [2, 5, 10, 12]. Once the concentration of polymer becomes too high, the surface tension of the system cannot be overcome. The charged jet becomes more inelastic, the Taylor cone becomes unstable and the polymer may be ejected as short fragmented fibers or beads. Increasing the polymer concentration still further results in the extrusion of the polymer from the needle tip as a large diameter thread which fragments; the mass of this material may be too large for it to reach the collecting target and it drops off the needle. These relationships assume that sufficient chain entanglements exist within the electrospinning solution to allow fiber formation to take place. In the absence of chain entanglements, fiber formation is non-existent or very limited. Spinning is precluded for some polymers if they are present in a very high molecular weight form that has

extensive chain entanglements; this results in a solution with a very high surface tension and the electrospinning jet may be too inelastic to support fiber formation.

The conductivity of the spinning solution may originate from the charge properties of the polymer and solvent and or from any stray "contaminating" ions that are present in the system. Manipulating the conductivity of the solution can make it possible to produce fibers from a given polymer that may otherwise not be possible to produce. For example, for some polymer systems it can be difficult to produce very small diameter fibers (e.g. < 100-200 nm). At low polymer concentrations the intrinsic charge of the solution may be insufficient to drive fiber formation, under these conditions an aerosol, rather than a fiber, may form in the electrospinning field. Alternatively, fibers with bead defects can also develop; these scaffolds look as if they are composed of fibers interspersed with beads (commonly resembles a fiber composed of "beads on a string"). These structures can compromise the mechanical properties of the scaffold. For many polymer systems, these limitations can be compensated for by simply adding exogenous salts to increase the charge density present in the electrospinning solution [12].

The surface tension of the polymer solvent solution is intrinsic to the specific system in use. Altering the solvent of a system can be used to manipulate this property under some circumstances; however, the solvent system to be used is largely dictated by the solubility properties of the polymer to be spun. This may limit the selection of solvents that are available for the spinning process. If it is not possible to change solvent system it may be possible to alter surface tension by adding or mixing additional solvents into the electrospinning solutions to alter the surface tension; in general a reduction in surface tension favors the formation of fibers over droplets [12].

The physical arrangement of the electrospinning setup also can be varied to modulate fiber diameter and scaffold properties. For example, increasing the flow rate of the syringe pump can increase the diameter of the resulting fibers. Conversely, and within limits, a decrease in flow rate, a manipulation that "starves" the electrospinning field of polymer (effectively reducing "polymer concentration" in the electrospinning field) results in a reduction in fiber diameter. Similar effects can be achieved, again within limits, by altering the electric forces that drive the spinning process. Here, increasing the voltages used in the spinning process results in the accelerated depletion of polymer from the Taylor cone. This will usually result in a decrease in fiber diameter. If a high voltage is required for electrospinning because of the intrinsic properties of the polymer solution, one way to overcome the reduction in fiber diameter normally observed in response to increased electrospinning voltages is to increase the delivery of polymer into the electric field. This can be achieved by increasing the rate at which the polymer is delivered to the syringe tip (increasing the rate of the pump).

It should be noted that changes in the flow rate and the electric field are usually limited in nature and by extension are also limited in the extent to which they can impact fiber formation. These electrospinning variables are tightly linked in a fundamental manner and the constraints placed on manipulating these processing variables are perhaps best illustrated by theoretical examples. At one extreme it is obvious if there is zero flow rate of polymer to the syringe tip no electrospinning can take place! Once sufficient polymer is delivered and the resulting fibers lack "bead defects" further increases in the flow rate will tend to drive fiber diameter somewhat larger. This process is limited in nature because increasing the flow rate too high results in the formation of very wet fibers and solvent welding (occurs when fibers wet with solvent collect on the target and the excess solvent literally melts adjacent fibers together). Increasing the electric

field decreases fiber diameter. If this is taken to an extreme, the polymer is depleted from the Taylor cone so quickly that an aerosol spray forms or fiber defects in the guise of beads may appear. Counteracting this effect by increasing flow rate may, once again, result in wet fibers and a solvent welded scaffold. In some systems the evolving solvent vapors may be present at such a high concentration that fiber formation is completely inhibited. Together, these observations underscore the interconnected nature of the variables that drive the electrospinning process.

Decreasing the distance between syringe needle and the collector can increase the fiber diameter. Reducing this distance reduces the interval of time that a fiber can undergo whipping and elongation within the electric field. As with changes in the strength of the electric field and or polymer flow rates there are limits to the extent to which this manipulation can be effective. Moving the target too close to the electrospinning source will not allow the fibers to fully dry prior to collecting on the target, once again resulting in solvent welding. Moving the target further way can allow for additional fiber thinning during the flight path of the jet-fiber thinning will cease once the fiber is dry. However, moving the target too far beyond the site in the trajectory where fiber drying occurs reduces the efficiency of fiber collection.

Environmental variables like temperature and humidity also affect fiber diameter. For example, increasing the temperature of the local environment will increase the rate at which solvent evaporates from the electrospinning jet while increasing the humidity can be expected to retard the loss of solvent from the jet.

Owing to the coiling and bending instabilities present within the charged polymer jet as it travels towards a static collecting plate (literally a flat sheet of material in this circumstance), electrospun fibers are typically deposited as coils of randomly oriented fibers. This type of scaffold is suitable for many applications where the native extracellular matrix appears to be

composed of random elements. However, a variety of tissue engineering applications ostensibly require scaffolds composed of fibers deposited into parallel arrays. Examples of where such anisotropic features might be desirable include tissue engineered ligaments, muscle and substrates for nerve growth. Efforts to induce alignment have generally focused on using some type of rotating target mandrel [5, 13, 14]. In a simple system a rotating cylindrical, rectangular or square mandrel can be used to induce fiber alignment. Once sufficient surface velocity has been achieved with the collecting mandrel, the coils of the charged electrospinning jet are caught and pulled onto the rotating surface. This allows for the collection of aligned, parallel segments of electrospun fibers that are oriented along the circumferential direction of the rotating target. While this method is effective at inducing anisotropy, it has inherent limitations. The extent to which fibers can be aligned is somewhat limited and larger diameter fibers can be induced to align more readily and more uniformly than smaller diameter fibers in this type of system.

In contrast to the above mentioned method of conventional electrospinning using a rotating target mandrel to deposit aligned fibers, our laboratory has develop of novel technique of electrospinning highly aligned fibers in a cylindrical construct with fibers oriented along the longitudinal axis of the construct [2]. This method will be discussed in detail in Chapter 4.

By regulating the various, above mentioned, electrospinning parameters, the fibers of the electrospun scaffold can be tailored as per the requirements of specific tissue engineering applications. The following chapters will elaborate on some of the applications of the tissue engineered electrospun scaffolds and how the electrospinning variables can be regulated to fabricate such scaffolds.

CHAPTER 3

Chapter 3. Electrospun Collagen: A Tissue Engineering Scaffold with Unique Functional Properties in a Wide Variety of Applications

***Preface**: The following manuscript appeared in the Journal of Nanomaterials, Volume 2011 [1]. The work included demonstrates the exploitation of the biological and functional properties of electrospun scaffolds for various tissue engineering applications. As noted there are a variety of electrospinning variables that can be manipulated to fabricate scaffolds with distinct characteristics. This chapter explores how the identity of the starting polymer solution, variations in electrospinning conditions and post electrospinning manipulations can be used to regulate and or alter the functional properties of electrospun scaffolds. Aspects of the materials and methods section of this published manuscript have been augmented with additional details.*

The functional properties of electrospun collage are explored; the native form of this polymer represents the most abundant extracellular protein of the mammalian system. This protein functions to establish the basic architectural organization of the structural body tissues. Collagen in the form of sponges has long been used in tissue engineering applications for the reconstruction of skin injuries. The results of our experiments indicate that fibers of electrospun collagen mimic many of the structural and functional properties of the native collagen fiber. And, as a result appear to represent a superior form of the protein for tissue engineering products. The quality of starting collagen polymer solution, electrospinning variables, and the post processing manipulations used to prepare this natural polymer for use in tissue engineering applications, all effect the structure and function of the resulting scaffold. This chapter demonstrates how these distinct properties, caused by slight process-modifications, can be exploited to develop distinct and potentially clinically relevant products.

Electrospun Collagen: A Tissue Engineering Scaffold with Unique Functional Properties in a Wide Variety of Applications

Balendu Shekhar Jha[1], Chantal E. Ayres[2], James R. Bowman[3], Todd A. Telemeco[4], Scott A. Sell[5], Gary L. Bowlin[2] and David G. Simpson[1]

[1]Department of Anatomy and Neurobiology
Virginia Commonwealth University
Richmond, VA 23298, USA

[2]Department of Biomedical Engineering
Virginia Commonwealth University
Richmond, VA 23298, USA

[3]School of Medicine
Virginia Commonwealth University
Richmond, VA 23298, USA

[4]Division of Physical Therapy
Shenandoah University
Winchester, VA 22601, USA

[5]Physical Medicine and Rehabilitation Service
Hunter Holmes McGuire VA Medical Center
Richmond, VA 23249, USA

ABSTRACT

Type I collagen and gelatin, a derivative of Type I collagen that has been denatured, can each be electrospun into tissue engineering scaffolds composed of nano- to micron-scale diameter fibers. We characterize the biological activity of these materials in a variety of tissue engineering applications, including endothelial cell-scaffold interactions, the onset of bone mineralization, dermal reconstruction, and the fabrication of skeletal muscle prosthetics. Electrospun collagen (esC) consistently exhibited unique biological properties in these functional assays. Even though gelatin can be spun into fibrillar scaffolds that resemble scaffolds of esC, our assays reveal that electrospun gelatin (esG) lacks intact α chains and is composed of proinflammatory peptide fragments. In contrast, esC retains intact α chains and is enriched in the α 2(I) subunit. The distinct fundamental properties of the constituent subunits that make up esC and esG appear to define their biological and functional properties.

INTRODUCTION

Electrospinning has been used to fabricate a variety of polymers, including natural proteins [4, 15, 16], sugars [17], synthetic polymers [18], and blends of native and synthetic polymers [13, 19, 20] into tissue engineering scaffolds composed of nano- to micron-scale diameter fibers, a size-scale that approaches the fiber diameters observed in the native extracellular matrix (ECM). The physical, biochemical, and biological properties of these unique biomaterials can be regulated at several sites in the electrospinning process. As this technology has matured, it has become apparent that many electrospun nanomaterials exhibit unusual, and often surprising, properties.

For many polymers, physical properties, including fiber diameter, pore dimension, and degree of scaffold anisotropy, can be regulated by controlling the composition of the electrospinning solvent, the air gap distance, accelerating voltage, mandrel properties, and/or the identity, concentration, and degree of chain entanglements (viscosity) present in the starting solutions [10, 11, 21]. The ability to directly manipulate these fundamental variables can have a dramatic impact on the structural and functional properties of electrospun materials. This is especially true when considering native proteins and blends of synthetic polymers and native proteins.

Collagen represents the most abundant protein of the mammalian ECM. As such, this natural polymer has long been used as a biomaterial in a variety of tissue engineering applications. This crucial ECM protein, as well as a variety of other native proteins, can be electrospun into fibers that resemble the native state [4]. Not surprisingly, the fibers of electrospun collagen do not appear to fully reconstitute the structural or mechanical properties of

the parent material [21]. Simultaneously, it is unclear to what extent the electrospun analog "must" recapitulate the native material to be a functional tissue engineering scaffold. The nature of the electrospun collagen fiber is the subject of debate and there are conflicting reports in the literature concerning its structural and functional properties [19, 21-24]. In this study, we compare and contrast the functional characteristics of electrospun collagen and electrospun gelatin (denatured collagen) in a variety of tissue engineering applications. We then explore how the procedures used to isolate and prepare collagen for the electrospinning process might ultimately impact its functional profile once it has been processed into a tissue engineering scaffold. We believe that it is essential to develop a more complete functional map of these novel materials to fully exploit them in the development of clinically relevant products.

MATERIALS AND METHODS

Collagen Preparation

Collagen was isolated at 4°C. Calfskin corium (Lampire Biologics, Pipersville, PA) was cut into 1 mm^2 blocks and stirred for 24 hr in acetic acid (0.5 M), processed in a blender into a slurry, and stirred for an additional 24 hr. Solutions were filtered through cheesecloth, centrifuged at 10,000× g for 12 hr; supernatant was recovered and dialyzed three times in ten-fold volume ice cold (4 ºC), ultra-pure 18 MΩ-cm water. Collagen isolates were frozen at -70 ºC and lyophilized. Bovine gelatin Type B isolated from skin was purchased from Sigma-Aldrich (75 or 225 bloom).

Electrospinning: Collagen and Gelatin

Materials were purchased through Sigma-Aldrich unless noted. Lyophilized collagen (at 55 mg mL^{-1}) and gelatin (225 bloom at 110 mg mL^{-1}) were solubilized for 12 hr in 1,1,1,3,3,3-hexafluoro-2-propanol (HFP) and electrospun [4, 10, 19]. Conditions were adjusted to produce scaffolds composed of fiber diameters that were nominally 1 μm in cross-sectional diameter. Solutions were charged to 22 kV and delivered (3–7 mL hr^{-1}) across a 25 cm air gap onto various target arrays. Electrospun samples, designated "recovered" electrospun collagen (rEC) or "recovered" electrospun gelatin (rEG) were produced by dissolving uncross-linked electrospun scaffolds immediately after spinning in ice cold (4 ºC), 18 MΩ-cm water; the final protein concentration was adjusted in these solutions to 1.5 mg mL^{-1}. In some experiments collagen and gelatin starting electrospinning concentrations were manipulated to produce fibers of varying diameters. Where indicated, scaffolds were vapor cross-linked (1–12 hr) in glutaraldehyde,

blocked in 0.1 M glycine, rinsed in Phosphate buffered saline (PBS), and disinfected in 70% alcohol prior to culture experimentation or implantation.

Cell Culture: Endothelial Cells

Electrospun scaffolds were cut into 12 mm diameter circular disks using a punch and cross-linked. A sterile 6 mm diameter glass cloning ring was placed on top of each disk and the inner portion of the disks were supplemented with 3,000 adult human microvascular endothelial cells (Invitrogen, C-011-5C) in a total volume of 100 μL. After 20 min the culture dishes were flooded with media to ensure that the cells were fully immersed. Cloning rings were removed after 24 hr of culture. The rings serve to confine the cells to a known surface area volume and help to insure a more uniform plating density across all treatment groups.

Cell Culture: Osteoblasts

Type I collagen and gelatin were electrospun across a 25 cm gap and directed at a grounded 6 inch diameter circular steel plate. Tissue culture dishes were placed between the source electrospinning solutions and the grounded target to directly collect fibers on the culture surfaces. After cross-linking, equal numbers of osteoblasts (Clonetics, CC-2538) were plated onto each surface and cultured for 10 days in OBM basal media (CC-3208). As controls, cells were plated onto native tissue culture plastic or random gels composed of Type I collagen (Vitrogen: Cohesion Technologies) after the methods of Simpson et al. [25]. For scanning electron microscope (SEM) imaging, osteoblasts were cultured directly on 6 mm diameter × 500 μm thick circular disks of electrospun collagen or gelatin (conditions optimized for 1 μm diameter fibers).

Dermal Reconstruction

Adult guinea pigs (Dunkin Hartely guinea pig; Harlan laboratories) were brought to a surgical plane, fur was shaved and skin swabbed in betadine. Four 1 cm^2 full-thickness dermal injuries (complete removal of the dermis and hypodermis and bordered by the superficial fascia of the panniculus adiposus) were prepared on the dorsum of each animal. Injuries were treated with scaffolds composed of electrospun Type I collagen or electrospun gelatin (electrospinning conditions adjusted to produce scaffolds composed of fibers ranging from 250 nm to > 2000 nm in average cross-sectional diameter). Scaffolds were vapor cross-linked to varying degrees as noted in the body of this study. Each wound was treated with a candidate scaffold and covered with a piece of silver gauze that was sutured in place. Silver gauze remained in place for 5–7 days. Animals recovered on a warming pad after surgery and were provided with pain mitigation (Buprenorphine 0.05 mg kg^{-1} SQ every 12 hours). Injuries were photographed at intervals. Data on wound closure was expressed as the percent injury surface area observed at the time of implantation. Representative samples were recovered for histological evaluation.

Muscle Fabrication

Three-day-old neonatal rats (Harlan laboratories) were decapitated, skin was removed. Skeletal muscle was removed from the limbs and body wall, minced into 1 mm^2 pieces in sterile PBS and rinsed until clear of blood. Tissue was incubated in a sterile flask supplemented with 0.25% trypsin (Invitrogen) in a shaking (100 RPM) 37 °C water bath. At 10 min intervals, tissue was cannulated and allowed to settle, and supernatant was removed and centrifuged at 800× g for 6 min. Cell pellets were pooled in DMEM plus 10% Fetal Bovine Serum (FBS) and 1.2% Antibiotic/Antimycotic (Invitrogen, 15240). A 60 min interval of differential adhesion to tissue

culture plastic was used to reduce fibroblast contamination in the pooled samples. Myoblasts were cultured for 3–5 days under conditions that minimized cell to cell contacts. In cell labeling assays, myoblast cultures were incubated in DiO (Invitrogen, L-7781) overnight according to manufacturer's recommendations.

Electrospun scaffolds were prepared on a 4 mm diameter round mandrel. With conditions optimized to produce 1 μm diameter fibers, cylindrical constructs were fabricated with a wall thickness of 200–400 μm [26]. Scaffolds were cross-linked, blocked and rinsed as described under the materials and methods section of this study discussing the electrospinning of collagen and gelatin. Myoblasts were trypsinized from the culture dishes and rinsed 2× in PBS by centrifugation (800× g, 6 min). Disinfected electrospun cylinders of collagen and gelatin were sutured shut on one end (5-0 silk) and suspended myoblasts were injected into the lumen of the constructs. Once the cylinders were supplemented with the cells, the constructs were sutured shut. Adult 150–180 g Sprague Dawley rats (Harlan laboratories) were brought to a surgical plane. Fur on the hind limb was shaved and skin was swabbed in betadine. In short-term studies (3 wks), a 4 mm × 15 mm long cylinder supplemented with cells was inserted directly into a channel ("intramuscular" position) prepared in the vastus lateralis muscle after the methods of Telemeco et al. [19]. In long term studies, a hemostat was passed deep to the quadriceps muscle group; engineered tissue (4 mm × 40 mm) was passed under the existing muscle mass and sutured (in an extramuscular position) to the proximal and distal tendons of origin and insertion for the quadriceps. Incisions were repaired, skin was stapled, and animals recovered on a warming pad.

Electrospinning: Nylon

To separate the fiber-forming properties of the different protein fractions from their fundamental biological properties, we applied acid soluble collagen and gelatin fractions to electrospun scaffolds composed of nylon 66 (Ambion). Nylon 66 as supplied by Ambion is engineered and designed for protein and nucleic acid blotting assays. Processing this material into electrospun fibers yields a unique blotting platform. Electrospun nylon has a high surface area and as a result exhibits high protein binding capacity. Nylon was spun after the methods of Manis et al. [26]. Conditions were optimized to produce charged nylon fibers ranging 1.0–1.5 μm in diameter.

Cell Culture: Adult Human Dermal Fibroblasts

Dermal fibroblasts (HDF), (Cascade Biologics: C-013-5C) were passaged 3–5 times in basal dermal fibroblast medium 106 supplemented with a low serum growth kit (Cascade Biologics, S-003-K) prior to experimentation.

Cell Adhesion Assays

Electrospun nylon scaffolds were immersed in 20% methanol/phosphate buffered saline (PBS) [26], rinsed 3× in PBS and installed in a dot blotter manifold (Topac Model DHM-48). Wells were supplemented with 50 μL of acid soluble calf skin collagen (control samples or fractions thermally denatured at 50, 60, 70, 80 or 90 ºC for 1 hr) or gelatin fractions containing equal amounts of protein. Samples of collagen were thermally denatured by incubating and holding acid soluble fractions in aliquots at various temperatures in a calibrated heating block. After 5 min of exposure to the electrospun nylon, solutions were sucked through the membrane

using a vacuum pump. Scaffolds coated with 1% bovine serum albumin (BSA) were used as controls. All wells were blocked with 100 μL of 1% BSA solution for 5 min and rinsed in PBS prior to use. In each assay, 3000 HDFs were suspended in 100 μL of media and applied to each surface for 1 hr at 37 ºC (dot blotter was used as a culture vessel; no vacuum was applied to the cell suspensions).

After the plating interval, the dot blotter was inverted to remove non-adherent cells; scaffolds were removed, rinsed in PBS, and fixed in ice cold methanol (20 min). For analysis, scaffolds were rinsed 5× in PBS plus 0.5% Triton x-100, and incubated overnight at 4 ºC in primary goat anti-rabbit GAPDH antibody (Sigma-Aldrich # G9545, 1:5000). All antibodies were diluted in LiCor Odyssey Blocking Buffer (L-OiBB), and L-OiBB plus 0.1% Tween-20 was used in all rinses. Cultures were rinsed 5× in L-OiBB, counter-stained with goat anti-rabbit IRDye 800 secondary antibody (LiCor 1:1000) for 1 hr and rinsed 5×. Data sets were captured at a line resolution of 169 μm using a Li-Cor Odyssey Infrared Imager. Adhesion was expressed as "Integrated Intensity" (signal-mm^2). Integrated intensity values were extrapolated to cell number using a standard curve of cells plated in parallel on 96 well culture dishes with the unknowns. Data sets were screened by one-way ANOVA ($p < 0.01$), Dunn's Method ($p < 0.05$), and a Mann-Whitney Rank Sum test ($p < 0.001$) was used in *post hoc* analysis. In cyclic RGD competition experiments, HDFs (10,000 cells per treatment) were incubated for 15 min at 37 ºC with 0.01, 0.1, or 1 μg mL^{-1} cyclic RGD peptide (Bachem, H-2574) or 1 μg mL^{-1} control RGD peptide (Bachem, H-4088). The cells were then plated for 1 hr on the different surfaces and were processed to image GAPDH as described.

Alpha Chain Analysis

Collagen samples were diluted to 0.15 mg protein mL^{-1} in Laemmli sample buffer (63 mM Tris HCL, 10% glycerol, 2% SDS, 0.0025% Bromophenol blue; pH 6.8) and separated by SDS interrupted gel electrophoresis using 10% polyacrylamide gels. Gels were run under non-reducing conditions until the dye front reached the base of the stacking gel, 1 mL of Laemmli buffer supplemented with 20% β-mercaptoethanol was added to the gel stacker and incubated for 30 min at room temperature. The separation run was then completed. Gels were stained with Coomassie brilliant blue overnight, de-stained and photographed. Densitometric analysis was conducted with the ImageJ software.

Cross-Linking Assays

See Newton et al. [21] for details of this colorimetric assay. In this assay samples were incubated in 2 mL of a solution of 4.0% (w/v) of sodium bicarbonate and 0.5% 2,4,6-trinitrobenzenesulfonic acid (TNBS) prepared in distilled water and incubated for 2 hr at 40 ºC. At the conclusion of this incubation samples were supplemented with 1.5 mL of 6 M HCl and held for 1.5 hr at 60 ºC. Aliquots of equal volume were placed into 96-well plates and read at 345 nm using a Spectramax Plus microplate spectrophotometer (Molecular Devices). Percent cross-linking was calculated from the formula

$$\%\ \text{cross} - \text{linked} = 1 - \frac{\text{AbsC}/\text{massC}}{\text{AbsNC}/\text{massNC}}$$

where AbsC = absorbance of the controls at 345 nm; massC = mass of controls in mg. AbsNC = absorbance of the unknowns at 345 nm; massNC = mass of unknowns in mg. All data is expressed as percent of cross-linking observed in dry, unprocessed electrospun scaffolds (controls) that have not been exposed to cross-linking reagents.

Scanning Electron Microscopy

Samples were fixed in 2% glutaraldehyde (Sigma) overnight, rinsed in PBS and dried for imaging with hexamethyldisilazane (Electron Microscopy Sciences). Samples were sputter-coated with gold for 2 min and imaged with a Zeiss EVO 50 XVP scanning electron microscope (SEM) equipped with digital image acquisition. Average fiber diameter and pore area data was determined from representative samples using ImageTool (UTHSCSA version 3.0). All fiber diameter measurements were taken perpendicular to the long axis of electrospun fibers [10].

Transmission Electron Microscopy

Samples were immersed in 2% glutaraldehyde prepared in 0.1 M Cacodylate buffer for 12 hr at 4 ºC. They were washed 3× in 0.1 M Cacodylate buffer and post-fixed in 1.0% osmium plus or minus 2.5% potassium ferricyanide for 1 hr [2, 19]. All samples were subjected to a graded series of alcohol dehydration (starting with 50% ethanol for 15 min, then 70% ethanol for 15 min, next 95% ethanol for 15 min, then 100% ethanol 2× for 15 min). Samples were next embedded in 1:1 Poly/Bed(Polysciences):Propylene oxide for 2 hr, followed by embedding in 2:1 Poly/Bed:Propylene oxide overnight in dessicator.

Histological Studies

Unless stated, for light microscopic histological studies the samples were stained with a solution of 0.1% Toluidine Blue, 0.1% Methylene Blue, 0.1% Azure II in 1% sodium borate.

RESULTS

Functional Performance of Electrospun Collagen

To compare and contrast the biological properties of electrospun collagen and electrospun gelatin, we conducted a series of *in vitro* and *in vivo* functional assays.

Endothelial Cell Growth

Critical to the bioengineering paradigm is the development of tissue engineering scaffolds that can support the proliferation and penetration of vascular elements. To evaluate this characteristic *in vitro,* we plated microvascular endothelial cells onto electrospun scaffolds of Type I collagen and electrospun gelatin composed of varying fiber diameters. During the initial plating phase, and over time in culture, cell shape, on both surfaces (collagen and gelatin), was modulated by the fiber size (and likely the pore characteristics that "travel" with the fiber size that is present in the electrospun scaffolds [10]) (Figure 3.1). Electrospun scaffolds of collagen and gelatin composed of small diameter fibers induced the expression of a highly flattened and stellate cell shape. This cell shape was retained throughout the culture interval on both surfaces (*e.g.*, Figure 3.1 compare (a) = day 1 with (b) = day 7 as well as (i) and (j)). With increasing fiber diameter, the cells assumed a more rounded and elongated phenotype. After 10 days, microvascular endothelial cells cultured on collagen- or gelatin-based scaffolds with average cross-sectional fiber diameter less than about 1.0–1.50 μm remained on the dorsal surfaces of the constructs (Figure 3.1 (q), (r), (u) and (v)). As fiber size exceeded this threshold value and pore size increased to about 10,000 nm^2, the cells began to penetrate into the scaffolds (Figure 3.1 (s), (t), (w) and (x)). These results suggest that the physical arrangement of fibers (i.e., the pore

characteristics) plays a role in regulating the infiltration of endothelial cells into an electrospun scaffold.

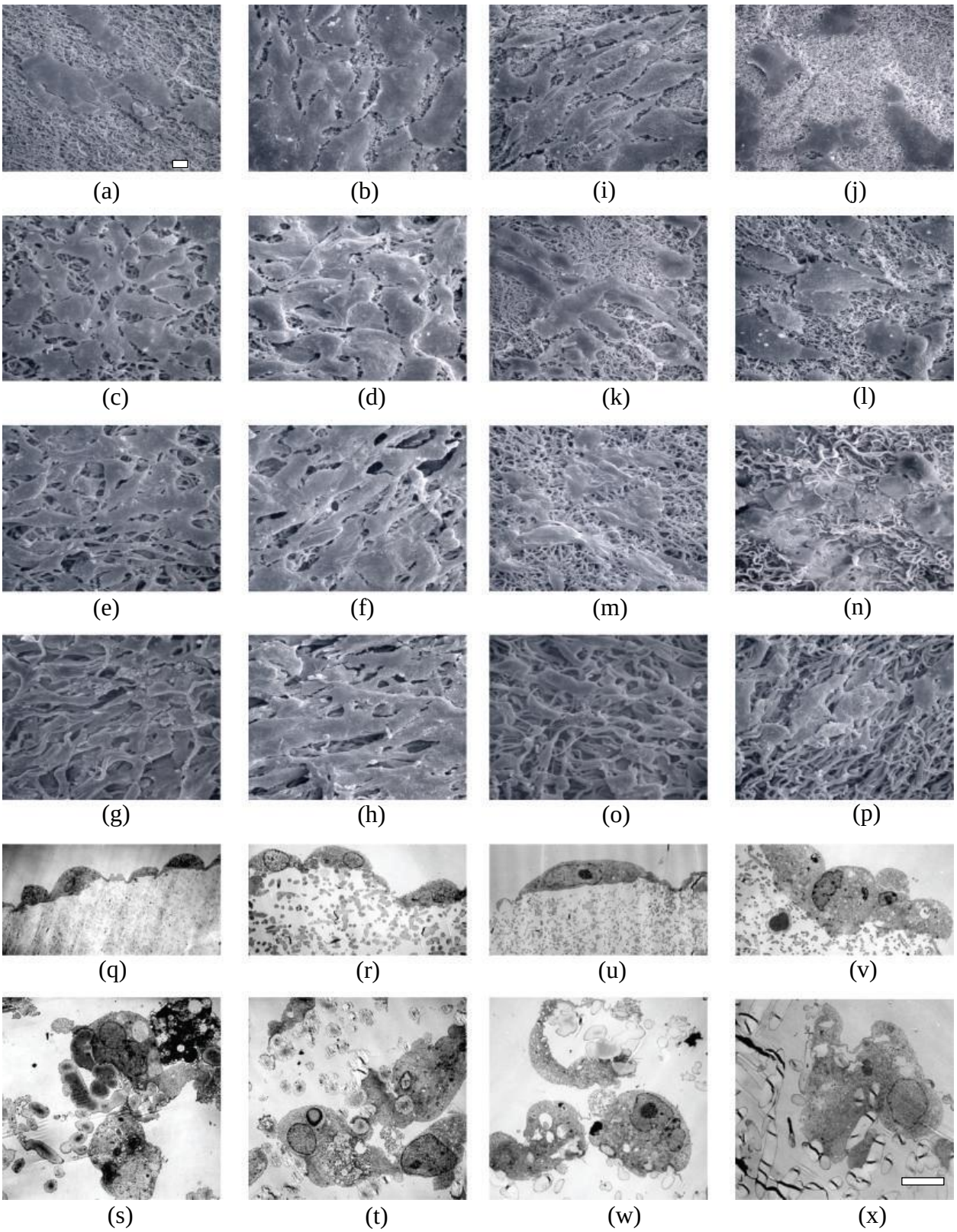

Figure 3.1: Endothelial interactions with electrospun collagen and gelatin.

Figure 3.1: Endothelial interactions with electrospun collagen ((a)–(h)) and gelatin ((i)–(p)). Endothelial cell shape varied as a function of increasing fiber diameter on both electrospun collagen (Day 1: (a), (c), (e), (g) & Day 7: (b), (d), (f), (h)) and electrospun gelatin (Day 1: (i), (k), (m), (o) & Day 7: (j), (l), (n), (p)). Cell shape established during the early stages of plating persisted throughout the entire culture interval (*e.g.*, for each scaffold cells at day 1 appeared to exhibit a similar cell shape after 7 days of culture). Cells expressed and retained a highly flattened and stellate shape when plated onto scaffolds composed of fibers less than 1,500 nm ((a)–(l)). At larger fiber sizes the cells exhibited a more elongated phenotype, this was especially evident on the collagen-based scaffolds ((e), (f), (g) and (h)). Penetration into the scaffolds was primarily regulated by average fiber diameter and pore size. TEMs of cross-sectional images of cells plated onto electrospun collagen ((q)–(t)) and electrospun gelatin ((u)–(x)) for 10 days. Average fiber diameters for collagen (a) & (q) = 449 ± 122 nm, (c) & (r) = 1,187 ± 297 nm, (e) & (s) = 1,886 ± 513 nm and (g) & (t) = 2,756 ± 855 nm. In gelatin (i) & (u) = 198 ± 50 nm, (k) & (v) = 491 ± 114 nm, (m) & (w) = 1,252 ± 302 nm, and (o) & (x) = 1,619 ± 414 nm (all fiber measurements from dry scaffolds prior to processing for cross-linking). Note that penetration was not evident until a nominal average fiber diameter of about 1,800 nm was achieved in the scaffolds (arrows in (r), (t), (x) indicate fibers in cross section). Scale bar in (a) for (a-p) = 20 μm, scale bar in (x) for (q-x) = 5 μm.

Osteoblast Differentiation

The 67 nm banding pattern typical of native Type I collagen is associated with the formation of nucleation and binding sites critical to the mineralization process in bone [27]. Superficially, electrospun fibers of collagen exhibit a similar structural motif. To examine the potential functional consequences of this motif, we plated osteoblasts onto surfaces coated with electrospun collagen and electrospun gelatin. Cultures plated onto surfaces coated with electrospun collagen exhibited low rates of proliferation and failed to form a confluent cell layer, even after 8 days. Phase bright crystals were present throughout these cultures (Figure 3.2). Cells plated onto surfaces coated with electrospun gelatin, Type I collagen gels, or native tissue culture plastic proliferated and formed a confluent cell layer over this same culture interval. Phase bright crystals were infrequently observed in any of these cultures. These data suggest electrospun collagen contains structural motifs necessary and sufficient to induce osteoblast differentiation and subsequent formation of hydroxyapatite crystals.

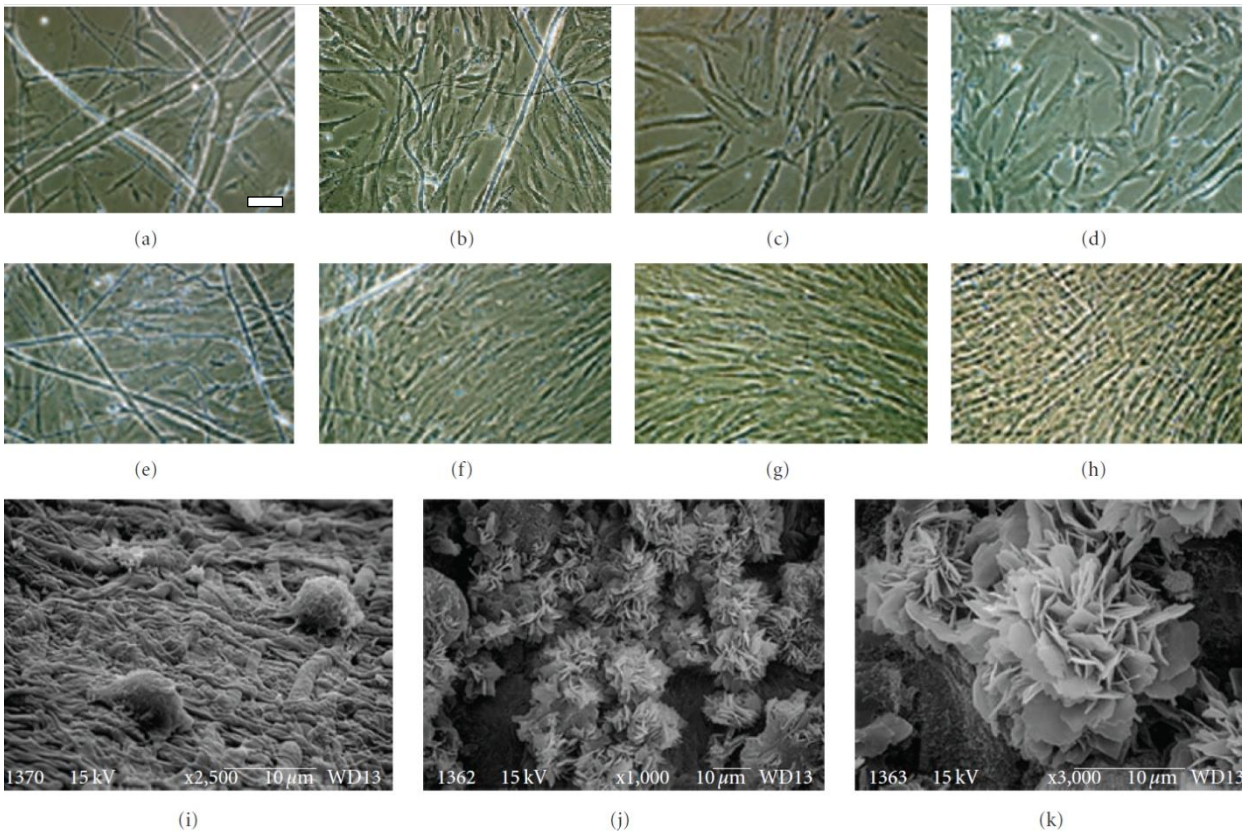

Figure 3.2: Osteoblast interactions with electrospun collagen and electrospun gelatin. Human osteoblasts plated for 1 (a)–(d) or 8 days (e)–(h). Cells plated on electrospun collagen ((a), (e)), electrospun gelatin ((b), (f)), collagen gel ((c), (g)), or tissue culture plastic ((d), (h)). Cells plated onto electrospun collagen remain sub-confluent after 8 days of culture (e) and accumulated phase bright crystals. At the ultrastructural level, osteoblasts plated onto electrospun gelatin expressed a rounded cell shape (i); when plated onto electrospun collagen, the cells were covered with elaborate arrays of plate-like structures typical of hydroxyapatite crystals ((j), (k)). Scale bar in (a) for (a-h) = 10 μm.

Dermal Reconstruction

From an architectural standpoint, tissue engineering electrospun scaffolds are theoretically very well suited for applications in dermal reconstruction. These constructs are deposited as nonwoven, fibrillar structures that exhibit an extensive void volume and pores that are completely interconnected with one another. To evaluate the efficacy of using electrospun collagen as a dermal template, we treated full thickness dermal injuries with various permutations of this material. To track the healing process, we measured total wound surface area as a function of treatment and time. We have used this metric because interventions that reduce wound contraction (as measured by an *increased* retention of wound surface area once the injury is healed) are associated with less scarring and more complete tissue regeneration [28].

In the first series of experiments, we treated wounds (1 cm^2) with dermal templates fabricated from electrospun collagen under conditions that produced fibers ranging 750–1,000 nm. These scaffolds were post processed to cross-link approximately 50% of the available sites. Wound closure took place in 16 days with these constructs (Figure 3.3(a)). When the extent of cross-linking was increased to 70% in these constructs, wound healing was delayed modestly and wound surface area was dramatically increased, a feature indicative of increased regeneration (Figures 3.3(a) and 3.3(c)). Histological examination of the tissue reconstituted with templates composed of electrospun collagen consistently revealed a smooth continuum of infiltrating cells. There were no overt signs of inflammation or fibrosis along the interface of the implanted templates and the adjacent uninjured tissue, regardless of the fiber diameter composition present in electrospun constructs of Type I collagen (Figures 3.4(a)–3.4(c)). Our tissue culture experiments demonstrated that the intrinsic architectural features present in an electrospun scaffold can modulate the extent to which endothelial cells can penetrate into these

constructs. We observed a similar trend in our dermal reconstruction experiments. Injuries treated with templates composed of fibers less than 500 nm in diameter were less densely populated than templates composed of fibers greater than 750–1000 nm in diameter (Figure 3.4).

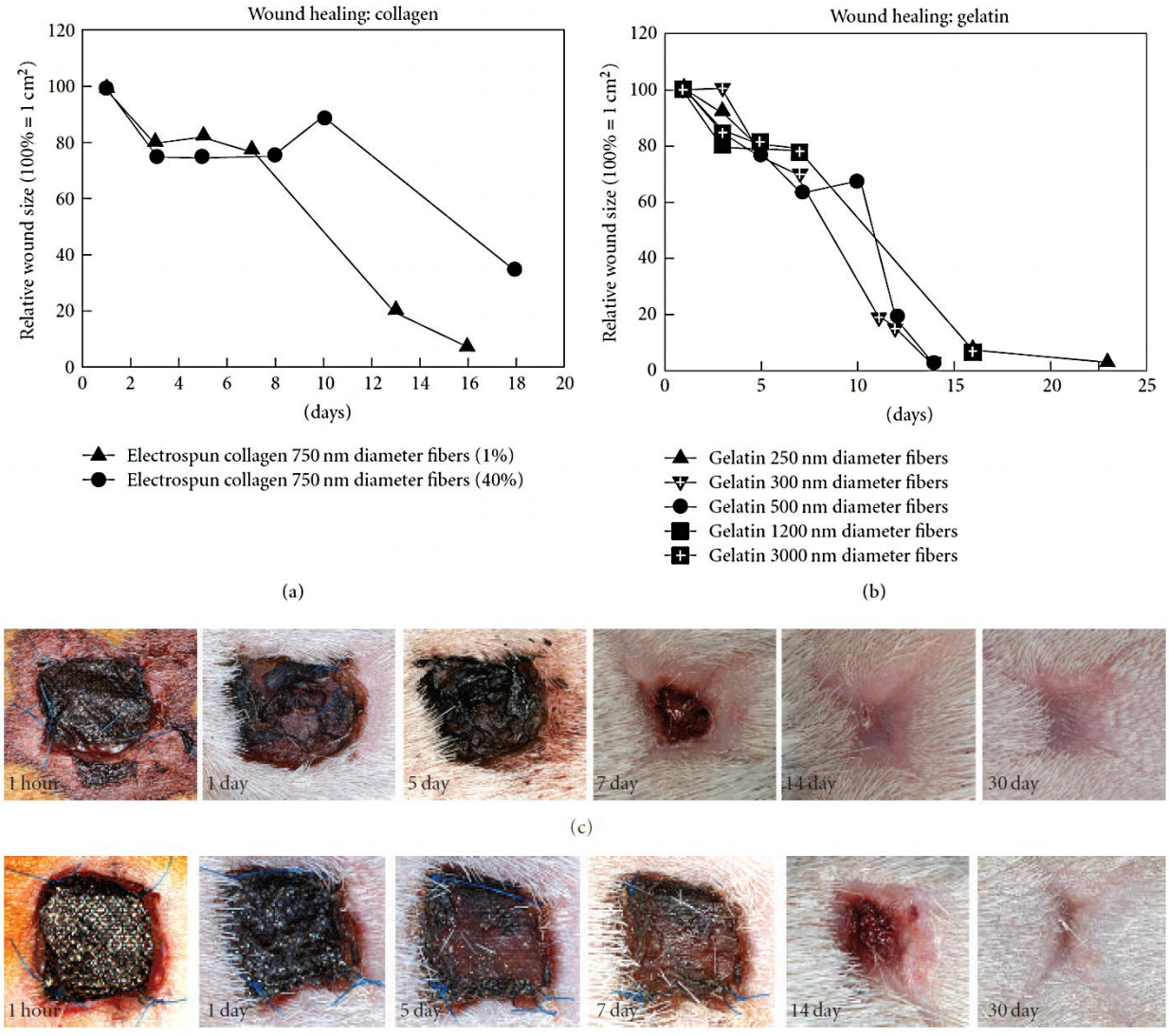

Figure 3.3: Dermal Reconstruction. Rates of wound closure in lesions treated with electrospun collagen (a) or electrospun gelatin (b). Note that increasing the extent of cross-linking has a modest effect on slowing wound closure and greatly increases total wound surface area in animals treated with electrospun collagen (a) and (c). Rates of wound closure were similar when injuries were treated with a wide variety of gelatin-based constructs (b) and (d). Panel (c) depicts the typical wound healing course for injuries treated with electrospun collagen in which approximately 70% of the available sites are cross-linked. Note the retention of wound surface area in this example. Panel (d) depicts the typical wound healing course for injuries treated with electrospun gelatin in which approximately 70% of the available sites are cross-linked. Note the classically X-shaped wound typical of a lesion that has undergone contraction.

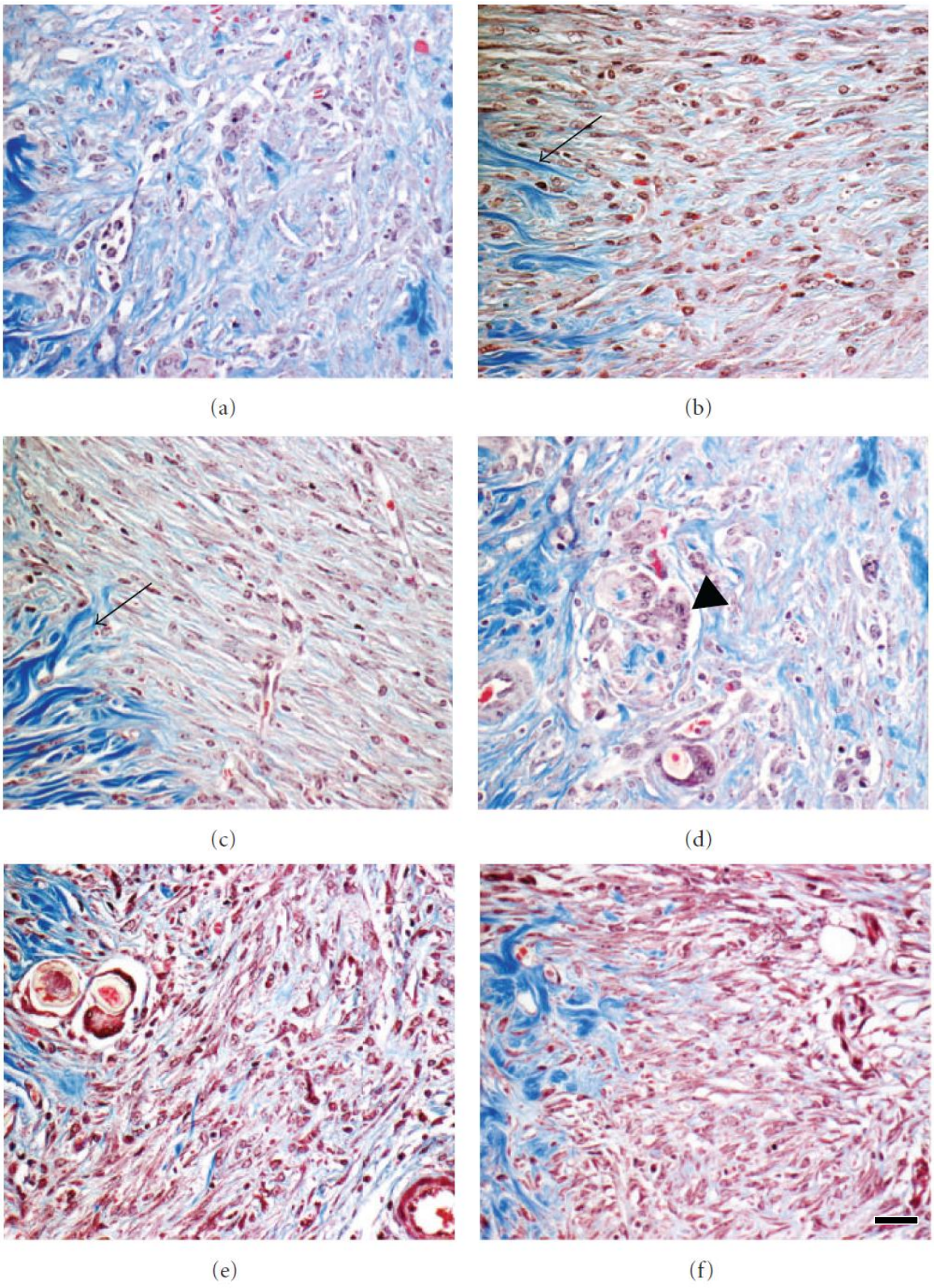

Figure 3.4: Dermal Reconstruction. Healing response to electrospun collagen and electrospun gelatin as a function of fiber diameter and pore dimension.

Figure 3.4: Dermal Reconstruction. Healing response to electrospun collagen (a)–(c) and electrospun gelatin (d)–(f) as a function of fiber diameter and pore dimension. Collagen-based implants exhibited a smooth continuum of cells at the interface of the lesion and the surrounding tissue. In each of the images depicted in this figure, native, uninjured tissue appears to the left of each data image (delineated by the large blue staining collagen bundles in the histological preparations, arrows (b) and (c)). Gelatin based-scaffolds were consistently less heavily infiltrated and exhibited evidence of an inflammatory response and accumulated foreign body giant cells (arrow head (d)). (a) and (d) average fiber diameter = 240–280 nm, average pore dimension =1500–2000 nm^2, (b) and (e) average fiber diameter 500–600 nm, average pore dimension 3000–5000 nm^2, (c) and (f) average fiber diameter 800–1000 nm, average pore dimension 4000–5000 nm^2. Scale bar in (f) for (a-f) = 20 μm.

In parallel experiments conducted with a wide variety of electrospun scaffolds composed of gelatin (average fiber diameters ranging from 250 nm to approximately 3000 nm), we were unable to replicate these results. Wounds treated with electrospun gelatin consistently healed in the classic X shaped configuration (Figure 3.3(d)) that develops in response to wound contraction, this feature developed regardless of the fiber diameter or the degree of cross-linking present in the gelatin-based scaffolds. These scaffolds were consistently infiltrated by foreign body giant cells (multi-nucleated macrophages), indicating an inflammatory response to the implanted electrospun gelatin (Figures 3.4(d)–3.4(f)). These data indicate that architectural features and the biochemical identity of an electrospun scaffold composed of collagen interact to define its unique functional characteristics.

Muscle Engineering

To evaluate the efficacy of using electrospun collagen in a cell-based tissue engineering application, we used an *in situ* strategy to fabricate skeletal muscle prosthetics. In these experiments, we electrospun Type I collagen onto a rotating 4 mm diameter mandrel; this resulted in the formation of a hollow cylinder with walls composed of 1 μm diameter fibers of electrospun collagen. These cylinders were then supplemented with myoblasts and implanted directly into the vastus lateralis muscle. After 3 weeks, tissue fabricated with electrospun collagen was densely populated with cells. Nascent myotubes and functional blood vessels were evident throughout these implants (Figure 3.5). As with the dermal-templates, we observed a smooth continuum between the surrounding tissue and the engineered muscle with no evidence of fibrosis. In contrast to these results, tissue fabricated with gelatin based materials was

necrotic, exhibited extensive fibrosis at the tissue interface and a massive infiltration of lymphocytes.

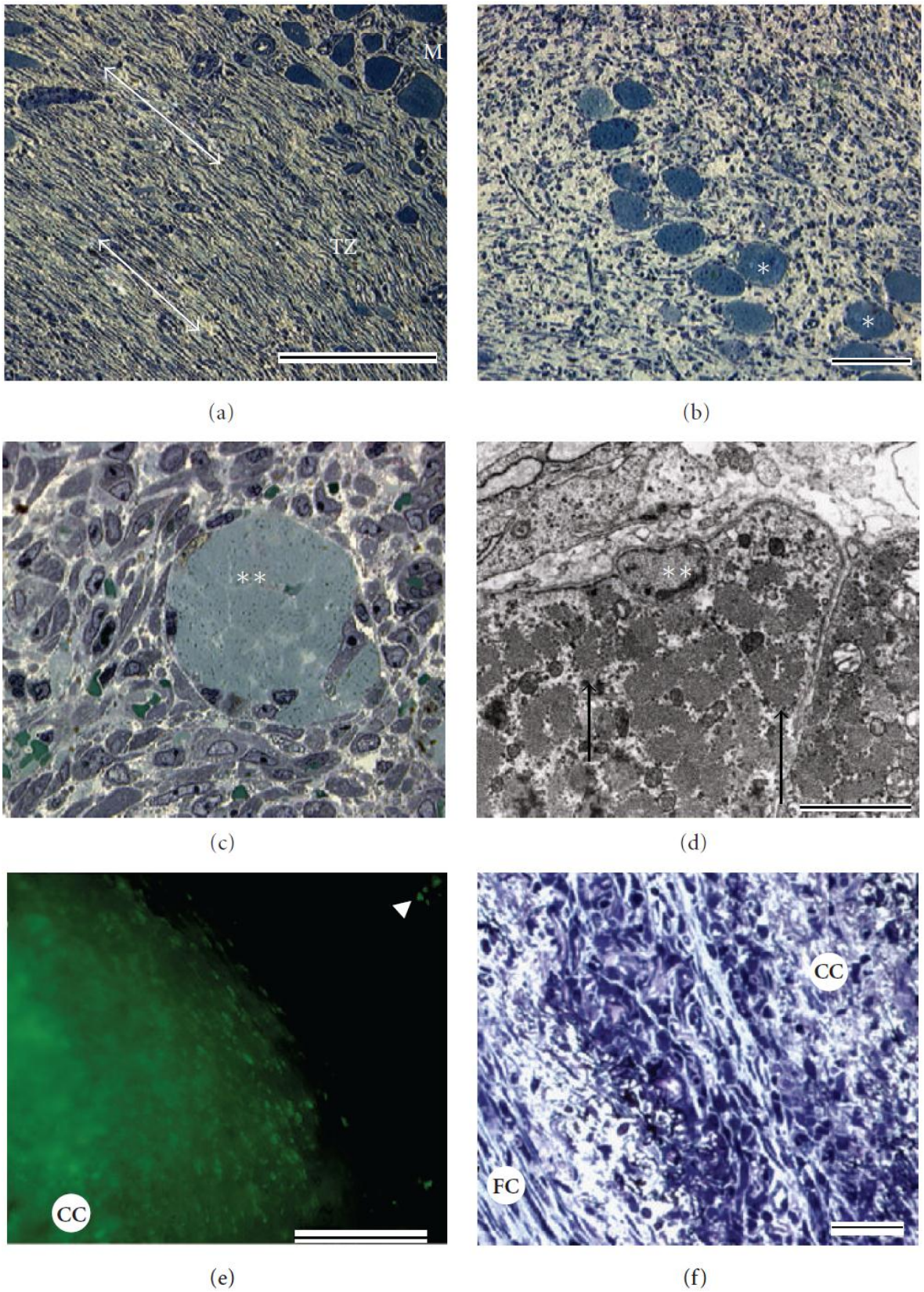

Figure 3.5: Muscle Fabrication: 3 Weeks.

Figure 3.5: Muscle Fabrication: 3 Weeks. (a) Cross-section through the wall of cylindrical construct placed within the tissue of the rat vastus lateralis. M = endogenous host muscle tissue, TZ = transitional zone occupied by the wall of the electrospun construct. Note the lack of a fibrotic capsule. ((b), (c)) Sections taken from within the lumen of the tissue, dense cell populations are evident as are nascent myotubes (*). Scattered vascular elements are apparent and intermingle with the surrounding cell population. (d) TEM cross-section of developing myotube with forming myofibrillar elements (arrows). (e) Cell labeling experiments (with DiO) indicate that few cells migrate out of the implanted tissues (arrowhead). The bulk of the labeled cells are retained within the lumen of the electrospun constructs. (f) Tissue fabricated from gelatin undergoes necrosis and develops a fibrotic capsule (FC). CC = central core of implant. Scale bar in (a) = 100 µm, (b) = 50 µm, (c) & (f) = 10 µm, (d) = 5 µm, and (e) = 25 µm.

Given these results, we next prepared engineered muscle tissue fabricated with electrospun collagen and directly sutured the constructs to the tendons of origin and insertion for the quadriceps muscle. These constructs were placed in an extramuscular position; in effect we are converting the quadriceps muscle into a “quintriceps” muscle. After 8 weeks, the engineered muscle was densely packed with fully differentiated myotubes that were distributed into stacked and linear parallel arrays that mimicked native tissue (Figure 3.6). This developing muscle tissue displayed well-formed myofibrillar elements. However, a range of cytoskeletal structural patterns was observed. For example, some areas of the tissue displayed loosely packed arrays of myofibrils (Figures 3.6(d) and 3.6(e)); other domains differentially took up the stains used to enhance contrast for light (Figure 3.6(g)) and transmission electron microscopy (Figure 3.6(h)). We suspect this differential staining is a reflection of protein density or protein identity with respect to the myofibrillar subunits. Collagen bundles were evident along the borders of the implanted tissue.

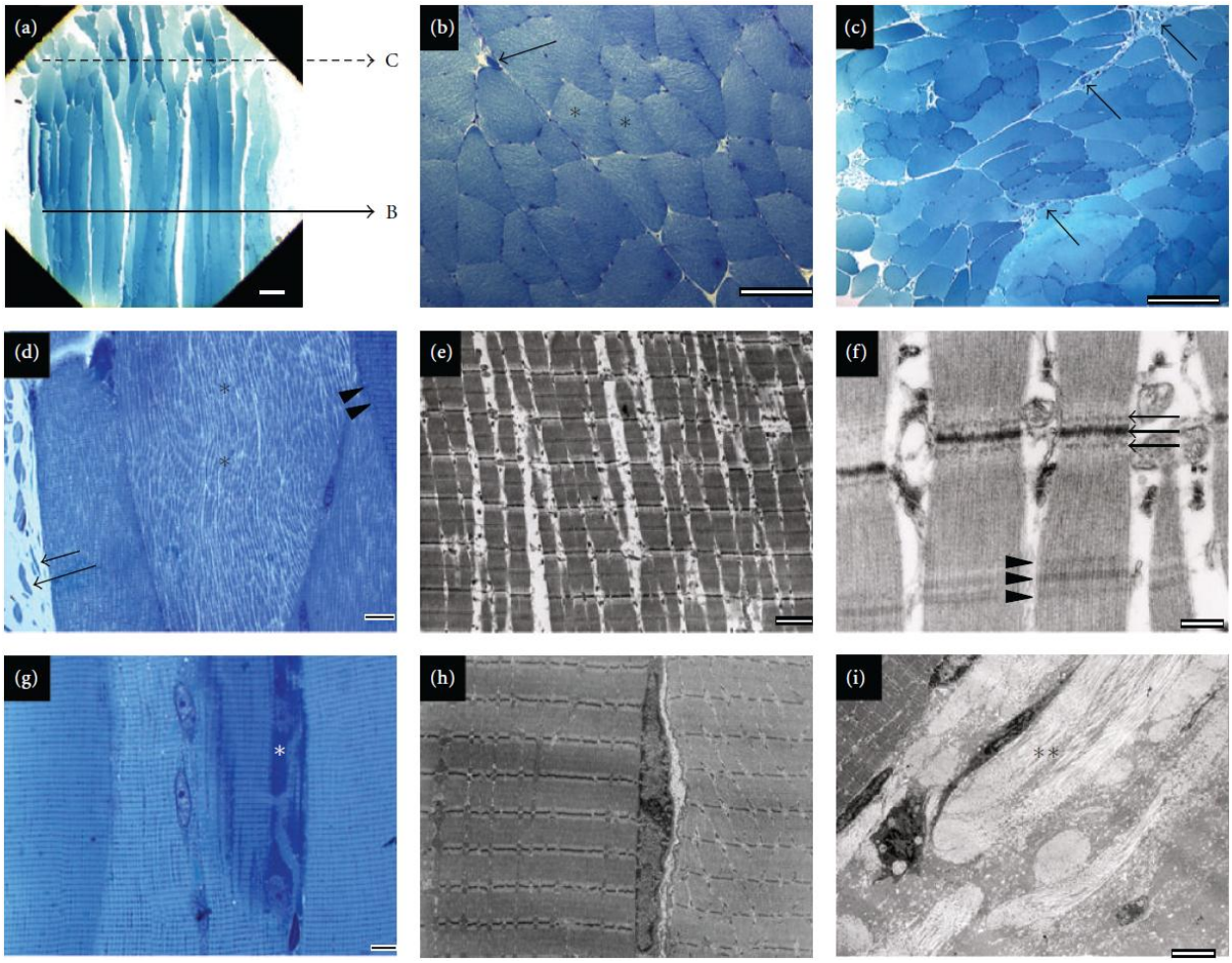

Figure 3.6: Muscle Fabrication: 8 Weeks. (a) Low magnification survey image depicting the terminal portions of muscle tissue engineered *in situ*. Images depicted in panels (b) and (c) were taken from the cross-sectional area denoted as "B" and "C", respectively in panel (a). The tissue distal to the attachment sites exhibited stacked arrays of myotubes ((b), asterisks). Tissue alignment is disrupted to some degree at the distal attachment sites as a consequence of the sutures used to place the tissue ((c), arrows indicate functional blood vessels). Myofibril density is observed to vary within cells that are in close proximity to one another ((d), arrowheads and asterisk; also the myofibrillar density in (d) and (e) to (g) and (h)) and some subdomains of the tissue stain differentially at both the light (g) and EM levels (h) with stains designed to enhanced contrast. The tissue is highly biosynthetic as evidence by the accumulation of proteins in the vicinity of the nuclei and golgi (g, asterisk). A subset of engineered tissue exhibits sarcomeres (f) with unusual cytoarchitectural patterns at the Z bands (arrows) and H zones (arrowheads) characterized by accessory electron dense structures. At the ultrastructural level, the implants are surrounded by collagen fibrils ((i) asterisks). Scale bar in (a) = 50 µm, (b) & (c) = 20 µm, (d) & (g) = 10 µm, (e) & (h) = 2.5 µm, (f) = 250 nm, (i) = 5 µm.

Analysis of Collagen Alpha Chain Structure and Function

Protein Analysis

We next conducted experiments to characterize how various processing conditions impact acid-soluble collagen and how these manipulations might regulate the evolution of the functional properties of an electrospun fiber. We first examined the effects of thermal denaturation on Type I collagen. These experiments were conducted to provide us with a benchmark for the evaluation of collagen structure and its α chain content in response to various steps in the electrospinning process. Collagen was isolated from calfskin corium using classical acid extraction methods, a procedure routinely used to prepare collagen as a biomaterial and for use in the electrospinning process [4, 19]. Figure 3.7 illustrates an SDS gel depicting the α chain content of the acid soluble parent extract with respect to fractions that have been subjected to varying degrees of thermal denaturation.

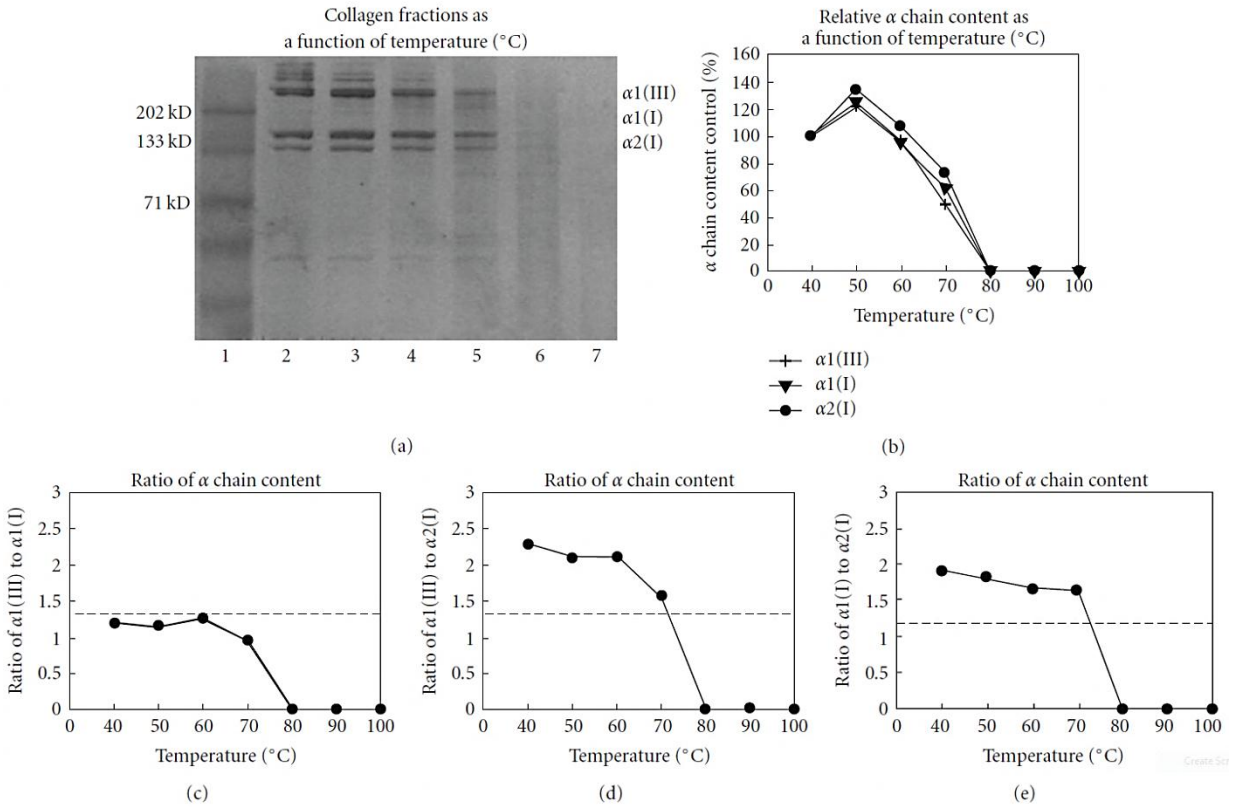

Figure 3.7: Analysis of Type I collagen α chain content. (a) Representative SDS gel depicting the effect of various degrees of heat denaturation on soluble collagen. Lane 1 = MW standards, 2 = control sample maintained and stored at 4 ˚C, 3 = sample heated to 50 ˚C for 1 hr, 4 = 60 ˚C, 5 = 70 ˚C, 6 = 80 ˚C, and 7 = 90 ˚C. (b) Densitometric analysis of α chain content from denaturation experiments. (c) Densitometric analysis (c) ratio of α 1(III) to α 1(I), (d) ratio of α 1(III) to α 2(I), (e) ratio of α 1(I) to α 2(I) as a function of thermal insult. Dotted lines in (c)–(e) depicts the actual ratio of α chains present in collagen recovered immediately after electrospinning (no thermal insult).

Protein fractions were held at 4 ˚C or heated to 50, 60, 70, 80, or 90 ˚C for 1 hr. Detectable changes in the protein banding patterns present on the SDS gels were visible in all samples subjected to heating. Densitometric analysis of the separated protein fractions revealed that 50% of the collagen α chains were lost within 1 hr when soluble collagen was exposed to 70 ˚C (Figure 3.7). Exposure to higher temperatures accelerated the loss of the collagen α chains from the soluble fractions and resulted in progressively more α chain fragmentation and smearing in the gel lanes typical of a sample that has been broken down into a heterogeneous mixture of peptides. At temperatures of 80 ˚C and greater, the protein bands corresponding to the individual α chains were completely lost after the 1 hr incubation interval. Commercially procured gelatin (collagen that has been heated and denatured during isolation) samples exhibited little or no protein banding associated with intact α chains on the SDS gels; these samples ran nearly exclusively as a continuous smear of proteins (not shown, see [19]).

To examine how the electrospinning process (solvents, electric field, and the flash-lyophilization of proteins that occurs during fiber formation) might alter collagen α chain content, we next prepared scaffolds composed of electrospun Type I collagen or commercially sourced gelatin (conditions optimized to produce average fiber diameters = 1 μm). As judged by scanning electron microscopy, these scaffolds were superficially identical. However, transmission electrospun microscopy reveals that scaffolds of electrospun collagen exhibit the 67 nm banding pattern typical of the native fibril (Figures 3.8(a)–3.8(d)). In contrast, fibers of the electrospun gelatin lack this distinctive structure and are nearly homogenous in appearance.

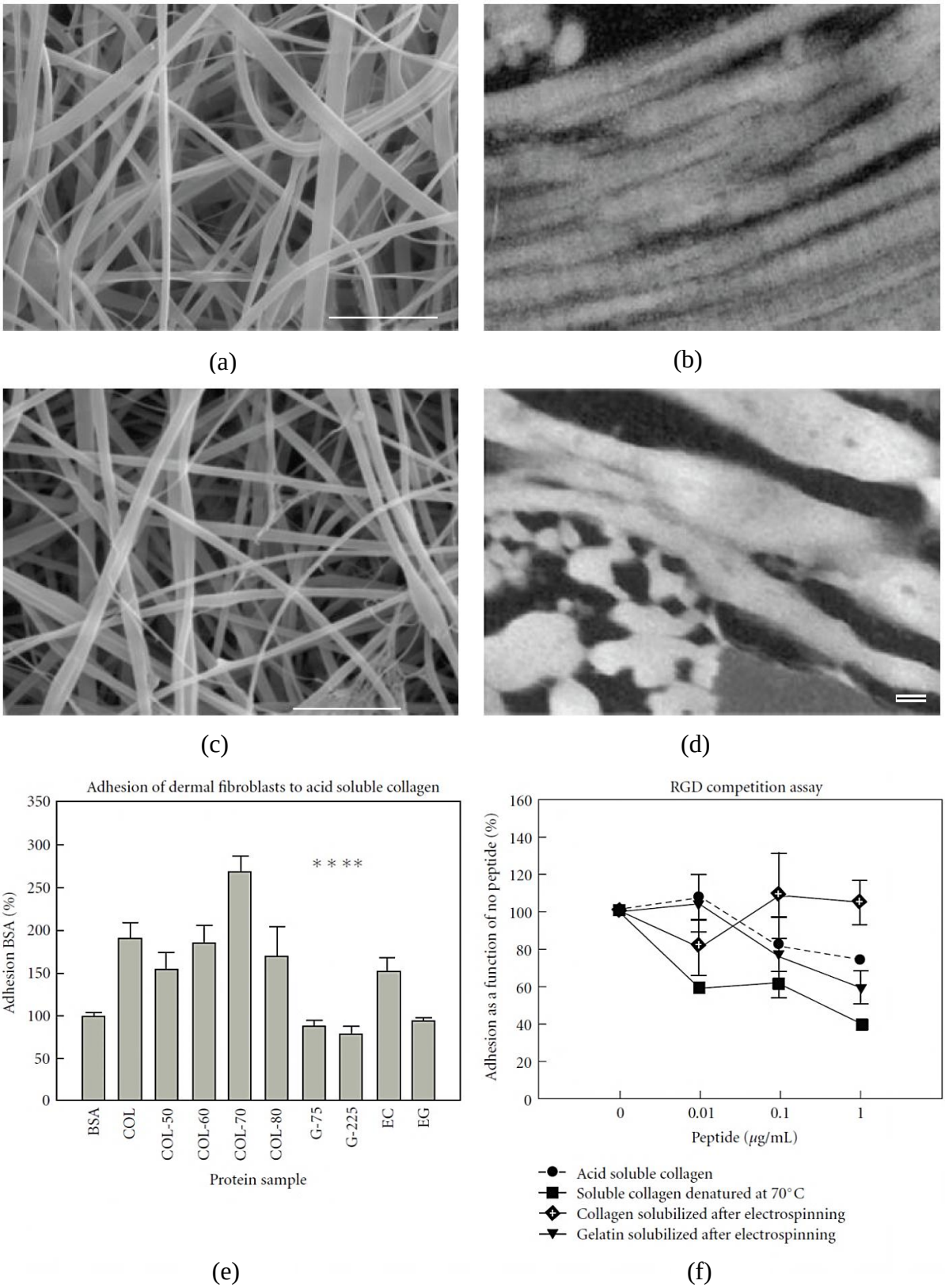

Figure 3.8: Ultrastructural and functional characteristics of collagen.

Figure 3.8: Ultrastructural and functional characteristics of collagen. Representative scanning electron and transmission electron micrographs of electrospun collagen ((a), (b)) and gelatin ((c), (d)). (e) Cell adhesion to various forms of collagen; maximal adhesion was observed in samples heated to 70 ˚C. (F) RGD competition binding assay. Cyclic RGD peptides inhibited adhesion to denatured collagens in a concentration-dependent manner and had minor effects on control acid-soluble starting material and no effect on collagen recovered from electrospun scaffolds. Scale bars in (a) and (c) = 10 μm. Scale bar in (d) for (b) and (d) = 100 nm.

For protein characterization of the electrospun scaffolds, we re-dissolved the collagen and gelatin-based scaffolds and separated the resulting extracts by SDS gel electrophoresis. The protein banding patterns on the gels and the specific compliment of α chains in the electrospun collagen and the control starting material (Acid soluble Type I Collagen: Figure 3.7) were similar, but not identical. Samples of electrospun collagen exhibited subtle derangements in α chain content and, as judged by densitometric analysis, it was enriched in the α2 (I) content (see Figure 3.7) with respect to the other α chains. Protein separation analysis of the electrospun gelatin revealed, as expected, nearly complete α chain fragmentation (these samples displayed complete fragmentation even prior to the electrospinning process) and was comparable to the calfskin collagen samples heated to 90 ºC for 1 hr (Figure 3.7).

Alpha Chain Functional Properties

Next we examined how thermal manipulation impacted the adhesion properties of acid-soluble collagen and its electrospun variants. In these experiments, we coated electrospun fibers of charged nylon with equal amounts of the various protein fractions described in Figure 3.7. This strategy made it possible to separate the fiber-forming capacity of each fraction from the biological activity that it displayed while presenting each fraction in a "matrix" that exhibited identical architectural patterns (fiber size, pore properties, and material properties). Equal numbers of dermal fibroblasts were then plated onto protein-coated electrospun nylon fibers. Rates of adhesion to the parent collagen fraction were approximately 50% greater than rates of adhesion to BSA-coated surfaces (Figure 3.8(e)). With one exception, thermal manipulation of the acid-soluble collagen fractions did not dramatically impact functional performance in these assays. Samples heated to 70 ˚C supported substantially higher rates of adhesion than the

BSA-coated surfaces and all of the other collagen fractions ($p < 0.002$), the gelatin samples ($p < 0.001$), and the samples recovered from electrospun scaffolds ($p < 0.001$). Rates of adhesion to Type I collagen recovered after electrospinning were not statistically different from the parent controls and were qualitatively much higher than gelatin and the electrospun gelatin samples.

The denaturation of collagen α chains uncovers RGD binding sites [29, 30]. To test for the presence of these sites in the different samples, we challenged cells in the adhesion assays with increasing amounts of cyclic RGD peptide. The RGD peptide reduced adhesion in the control samples by about 20% and nearly 60% in collagen samples that been heated to 70 °C prior to their use in the assay. No inhibition was detected in the collagen recovered after electrospinning (Figure 3.8(f)). It is clear from the RGD-based competition assays that collagen recovered after electrospinning behaves very differently than denatured collagens or material recovered from a scaffold of electrospun gelatin. This observation is relevant when considering the functional properties of an electrospun collagen fiber that appears to lack the 67 nm repeat banding pattern. As long as the α chains are intact, even if they are not arrayed into a polymeric form that exhibits the 67 nm repeat banding pattern, these fibers can be expected to exhibit unique and potent biological properties. Together, our SDS gel assays and adhesion results indicate that electrospinning does not directly denature collagen α chains.

DISCUSSION

In this study, through our functional assays, we explored the biological properties of electrospun collagen and electrospun gelatin. These two materials (collagen and gelatin) consistently exhibited very different functional profiles in all our assays. We note that endothelial cells began to penetrate into the fiber arrays of both electrospun collagen and electrospun gelatin once a critical fiber/pore threshold was reached. However, subjectively cell growth appeared to be much more rapid on the collagen-based scaffolds. We conclude from these *in vitro* experiments, in the absence of an inflammatory cascade or other antigenic complications, that endothelial cell infiltration is not limited by scaffold composition. Rather, gross structural properties are more important in this type of setting. The composition of the scaffolds appeared to dictate more subtle functional characteristics that regulated cell growth.

Cell culture experiments conducted with osteoblasts indicate that fibrils of electrospun collagen appear to be sufficient to induce differentiation and promote the accumulation of hydroxyapatite crystals *in vitro*. We believe this rather unexpected result may be a reflection of an intrinsic structural motif that is uniquely present in electrospun collagen. We did not observe this same result when we plated cells onto a collagen gel, a form of collagen that normally self-assembles into fibrils that contain a repeating banding pattern that also mimics native collagen [31]. Since both electrospun collagen and the fibers present in a collagen gel can exhibit a banding pattern, it is unclear what drives these results. It is clear that these two types of fibers have subtle structural differences; fibers of electrospun collagen are not stable in an aqueous environment, unless they are cross-linked. In contrast, the fibers of a collagen gel are fully stable under these conditions and do not require such treatment. Fiber stability in a collagen gel is linked to the

exothermic reaction that occurs during fiber polymerization; this leads to the partial denaturation of the constituent α chains and results in a more stable fiber structure. In the electrospinning process, collagen alpha chains essentially undergo flash lyophilization. These inherent differences in the fiber formation process likely result in the production of fibers exhibiting very different fine structure.

In dermal applications, wounds treated with electrospun collagen and electrospun gelatin underwent resolution over a similar time course. The nature of the tissue that resulted at the conclusion of wound closure was very different and varied as a function of fiber composition and the extent of cross-linking that was introduced in the scaffolds. Injuries treated with lightly cross-linked electrospun collagen and all samples of electrospun gelatin underwent varying degrees of wound contraction. Introducing additional cross-linking into the collagen-based materials likely stiffens the constructs and makes them less susceptible to wound contraction. All of the collagen-based scaffolds were infiltrated by fibroblasts and exhibited numerous functional blood vessels. In contrast, injuries treated with electrospun gelatin were consistently less densely populated and showed an accumulation of foreign body giant cells at the borders of the wound. This adverse response in the gelatin-based materials is undoubtedly related to the pro-inflammatory peptides present in highly denatured collagens [32].

The essential capacity of electrospun collagen to support rapid cell infiltration was readily apparent from the experiments in which we fabricated skeletal muscle *in situ.* The interconnected nature of the pores present in a scaffold of electrospun collagen appears to provide more than enough passive nutrient exchange to support the donor cell population. A nascent vascular supply developed in tandem with muscle differentiation to support the increased metabolic demand associated with this process. Consistent with this conclusion, we observed

functional blood vessels traversing the external walls of the implanted tissue and penetrating into the internal aspects of the constructs. In contrast, once again, tissue fabricated with electrospun gelatin induced a marked inflammatory response, and by 3 weeks the tissue was largely necrotic.

To develop an understanding of the basis of biological properties of electrospun collagen, we compared and contrasted the structure and function of collagen α chains in samples subjected to varying degrees of thermal denaturation and electrospinning. Not surprisingly, α chain content is dramatically altered in response to heating. At 70 ˚C for 1 hour, 50% of the α chains are lost; at 80 ˚C there is essentially complete α chain fragmentation and specific bands corresponding to α1(III), α1(II), and α2(I) are no longer detectable. The α chain content of collagen subjected to electrospinning is subtlety altered from the pattern observed in the starting materials (acid-soluble collagen). Based on our analysis, we have concluded that electrospun samples become enriched in α2(I) content. This conclusion is based on the observation that the ratio of α1(III): α1(I) is normal in the electrospun samples, α1(III): α2(I) is reduced and α1(I): α2(I) is reduced. Since the ratio of α1(III): α1(I) is unchanged we must assume that no change in α1(III) content has occurred as a consequence of the electrospinning process. Given this assumption and the observation that both α1(III): α2(I) and α1(I): α2(I) are depressed; the common factor is a change in α2(I) content; an increase in α2(I) is the simplest explanation for the observed results. As the denominator in both ratios, any increase in α2(I) content results in a decrease in these ratios. It is unclear how this enrichment may occur; it is possible that differences in alpha chain solubility (or stability) in the electrospinning solutions may exist, leading to a preferential enrichment of the α2(I) chain. This result awaits further investigation.

Our baseline adhesion experiments failed to definitively identify a specific binding profile that might be used to evaluate the functional profile of the collagen α chains. A number of

integrins (α1β1, α2β1, α3β1) bind to Type I collagen in an RGD-independent manner and the αvβ3 integrin binds with high affinity to denatured collagen in an RGD-dependent manner [30]. In competition binding assays, RGD challenge had little or no effect in control samples of collagen or collagen that had been recovered after electrospinning, suggesting that electrospinning in and of itself does not induce damage in a fashion that specifically uncovers cryptic RGD binding sites. We saw a dramatic decrease in adhesion when these same experiments were conducted with collagen fractions that had been heated to 70 ˚C, these samples exhibited clear evidence of denaturation in our SDS gel studies.

CONCLUSIONS

Biophysical and structural evaluations demonstrate that electrospinning does not truly reconstitute the native structure of the collagen fibril [22]. Additionally, our data suggests that fibers of electrospun collagen become enriched in α2(I) content. However, our functional assays demonstrate that electrospun collagen has unique biological activity in a wide variety of tissue engineering applications. These data argue that it is not necessary to fully recapitulate the structure of the native fibril to generate a biologically relevant tissue engineering scaffold.

We believe that there are likely three critical variables that ultimately interact to determine the structural and functional properties of the electrospun collagen fibril. These include the quality of the starting material, the specific electrospinning conditions and, finally, the post-processing manipulations that are used to prepare the material for use in a tissue engineering application. The first consideration is paramount; the starting material must not be denatured during any of the processes used to isolate and prepare the collagen for electrospinning (acid extraction, centrifugation steps, lyophilization and storage). The use of partially denatured collagen will obviously compromise the functional profile of the final product. Gelatin, a material that is composed of highly fragmented peptides readily spins into fibers but, it is highly pro-inflammatory in many settings.

Second, the role of fiber size in the formation of the ultra-structural organization of electrospun collagen has not been explored to any extent. The 67 nm banding pattern observed in electrospun samples appears to be most prominent in constructs composed of small diameter fibers. Some laboratories report that this banding pattern is confined to relatively small domains in an electrospun scaffold or that it is absent altogether [22]. We would argue that the 67 nm

repeat does not have to be present to impart potent functional properties onto the electrospun collagen fiber. Our cell adhesion experiments demonstrated that native and denatured collagen α chains have very distinctive biological properties, even when they are not assembled into fibrils. Given the dramatic differences in performance that distinguish electrospun collagen from electrospun gelatin in a broad spectrum of tissue engineering applications, it seems premature to discount the functional significance of this material [22].

Finally, during electrospinning collagen α chains are subjected to a very high strength electric field. This electric field must place these peptides in a high energy state as they traverse the charged electrospinning field; these protein subunits are then frozen and trapped in this high energy state by the flash lyophilization process that makes fiber formation possible. This residual energy may have direct role in determining the fine structure (banding) of the resulting fibers. Electrospun fibers of collagen that have been modestly cross-linked will undergo coiling when placed into an aqueous solution; this coiling is dramatically reduced as a function of increasing degrees of cross-linking [21]. At very high levels of cross-linking, fibers of electrospun collagen retain a nearly linear conformation when hydrated.

Modest cross-linking conditions appear to stabilize gross fiber structure (sufficient to keep the fibers from dissolving in an aqueous buffer); however, a modest degree of cross-linking does not appear to be sufficient to completely suppress α chain reorganization as these subunits return to a basal energy state. Upon hydration, the shedding of this excess energy appears to drive coiling. At high levels of cross-linking, fibril coiling is suppressed, suggesting the α chains are trapped in a very different tertiary configuration as compared to the fibers of more modestly cross-linked structures that can undergo molecular reorganization. The potential contribution of these variables in the formation of structure, and functional considerations in the electrospun

collagen fibril, awaits further investigation. Given the potent biological activity of electrospun collagen, in a broad spectrum of applications, we can anticipate the development of unique tissue engineering scaffolds and the introduction of a new generation of tissue engineering products in the clinical market place.

ACKNOWLEDGMENTS

This study is supported in part by NIH EB003087 (Simpson) and USAMRMC 9918006 (Simpson). Electron microscopy was conducted at the VCU Department of Neurobiology and Anatomy Microscopy Facility, supported in part by NIH-NCRR Shared Instrument Grant (1S10RR022495) and NIH-NINDS Center Core Grant (5P30NS04763).

CHAPTER 4

Chapter 4. Two pole air gap electrospinning: Fabrication of highly aligned, three-dimensional scaffolds for nerve reconstruction

***Preface**: The following manuscript appeared in Acta Biomaterialia, Volume 7, Issue 1, January 2011 [2]. While this is a published manuscript, the section detailing the 2D FFT method for measuring fiber alignment has been augmented beyond the original text of the paper. The concept of fabricating scaffolds with aligned fibers was introduced in Chapter 2 and there are a variety of tissue engineering applications that require scaffolds composed of aligned fiber arrays (e.g. muscle engineering, tendon etc.). However, conventional electrospinning systems deposit fibers into flat sheets, a structure that is difficult to translate into applications like nerve guides that are best met by a more three-dimensional structure.*

In the conventional electrospinning setup, the degree of fiber alignment, within limits, is directly proportional to the rotational speed of the mandrel [10]. These systems are composed of a single power supply and a grounded rotating mandrel. While effective at inducing alignment in fibers, alignment does deteriorate in these systems at smaller fiber diameters (< 1 μm). This is likely caused by multiple factors. For example, the chaotic nature of fiber whipping that takes place with the formation of a smaller diameter fiber limits the extent to which the orientation of the charged jet can be controlled. Conversely, conditions that favor the formation of larger diameter fibers allow the charged jet to carry more momentum and, as a result, it undergoes less whipping in the electric field. In this model of fiber alignment less whipping during fiber formation is associated with a "stiffer" charged jet that exhibits a straighter trajectory, a characteristic feature that increases the fraction of the material that can be collected, and reeled onto the rotating mandrel as linear segments.

Undoubtedly, the moving mandrel also induces the formation of a very complex electric field which greatly exacerbates the complexity of fiber whipping that intrinsically occurs with the bending instabilities that are present during fiber formation. The Coulomb repulsion charges that are present within the electrospinning jet drive these bending instabilities; these charges interact with this external electrospinning field in a highly complex fashion [7]*. Air currents induced by mandrel rotation (which for a square mandrel that is 10 mm on each side might require a rate of rotation that approaches 8,000 RPM to induce alignment) also disrupt the trajectory of small diameter fibers as they approach the spinning mandrel. These air currents can be expected to have a much larger effect on a smaller diameter fiber (< 800 nm) than a larger diameter fiber (> 800-1,000 nm)* [5] *(spinning under a vacuum to reduce this effect has not been explored to any great extent and is technically difficult). Upon visual inspection, and most likely owing to a more elastic nature, smaller diameter fibers will display a more tortuous topography than lager diameter fibers – this intrinsic property further degrades the ability to induce alignment with nano-scale diameter fibers with a rotating mandrel system. These properties limit the extent to which the fibers of constructs that are composed of smaller diameter fibers can be aligned.*

Fiber alignment is a difficult parameter to define and several different metrics have been used to transition subjective statements of alignment into a meaningful and objective measurement that can be quantified. Each method has its own advantages and disadvantages. A visual inspection of a scaffold can reveal that it has some degree of alignment, but the more critical question is how much alignment is there? A direct measurement of anisotropy can be made using destructive materials testing techniques [11]*. To test for anisotropy a series of candidate scaffolds are tested to failure along the presumptive axis of fiber orientation and at a*

90 degree angle to this orientation. If a scaffold is composed of aligned elements it will exhibit a higher degree of stress and undergo less strain along the axis of fiber alignment with respect to any testing conducted off this axis [11]*. This is because the material properties in the aligned direction will be governed by the physical properties of the polymer. Off-axis material properties are more closely associated with the physical properties that are dictated by scaffold architecture and any interactions between adjacent fibers. In the case of an aligned material the material properties would be largely determined by the electrostatic interactions of the adjacent fiber arrays and not the polymer itself* [21]*. Materials testing is an extremely effective method to measure the extent of fiber alignment that is present in a scaffold, unfortunately, by definition materials testing is a destructive test and the scaffold under consideration is lost to further use.*

Our laboratory has developed and refined optical methods for measuring fiber alignment based on the 2D FFT function [14]*. This approach is entirely non-destructive in nature and as such its principle advantage is this metric makes it possible to evaluate the alignment of a scaffold and then use that same scaffold in a tissue engineering application. The software to conduct this analysis is readily available as shareware (Image J). In this technique a digital-data image of the scaffold is captured, this image may be a light, scanning electron microscope or a fluorescence image. The 2D FFT function then examines the image to determine the extent to which edges (transitions in contrast) occur along different orientations in the data image. We have externally calibrated and verified the efficacy of the 2D FFT method by measuring fiber alignment in a scaffold using this technique and then using destructive materials testing on that same sample to verify its material properties and therefore its alignment* [11]*. Those experiments revealed that incremental changes in fiber alignment induce incremental changes in the stress observed at failure for the electrospun scaffolds.*

This Chapter will discuss the use and characterization of a novel electrospinning technique to fabricate scaffolds with aligned fibers and its use to promote nerve regeneration. Macroscopically, the nerve guides produced by this novel processing strategy are cylindrical in nature. These guides are composed of dense fiber arrays that are oriented in parallel with the long axis of the construct. Unlike conventional synthetic hollow nerve guides, these guides exhibit a unique 3D architecture; they lack a central lumen. The intrafiber spaces of these constructs literally provide thousands of individual channels to direct axon growth. These channels are designed to limit axon growth cone deviations and drive the elongation of axons to occur predominately in one axis, thereby accelerating the regeneration process. In turn, this can be expected to decrease de-innervation atrophy and the associated complications of delayed peripheral nerve regeneration.

Critical to the performance of these are the aligned fiber arrays that comprise the structure. These fiber arrays must provide guidance cues to direct preferential axon outgrowth and exhibit sufficient material strength to bear the mechanical forces encountered during manual manipulation and the movements that occur in situ once it is in place. To this effect, our laboratory has devised the technique of two pole air gap electrospinning that is discussed in detail in this Chapter. The basic set-up used in the fabrication technique is illustrated in figure 4.1. It uses a dual collecting target to induce the formation of a cylindrical construct composed of aligned fiber arrays. Our assays demonstrate that this system can induce, unlike conventional electrospinning systems, an unprecedented degree of fiber alignment, independent of fiber size.

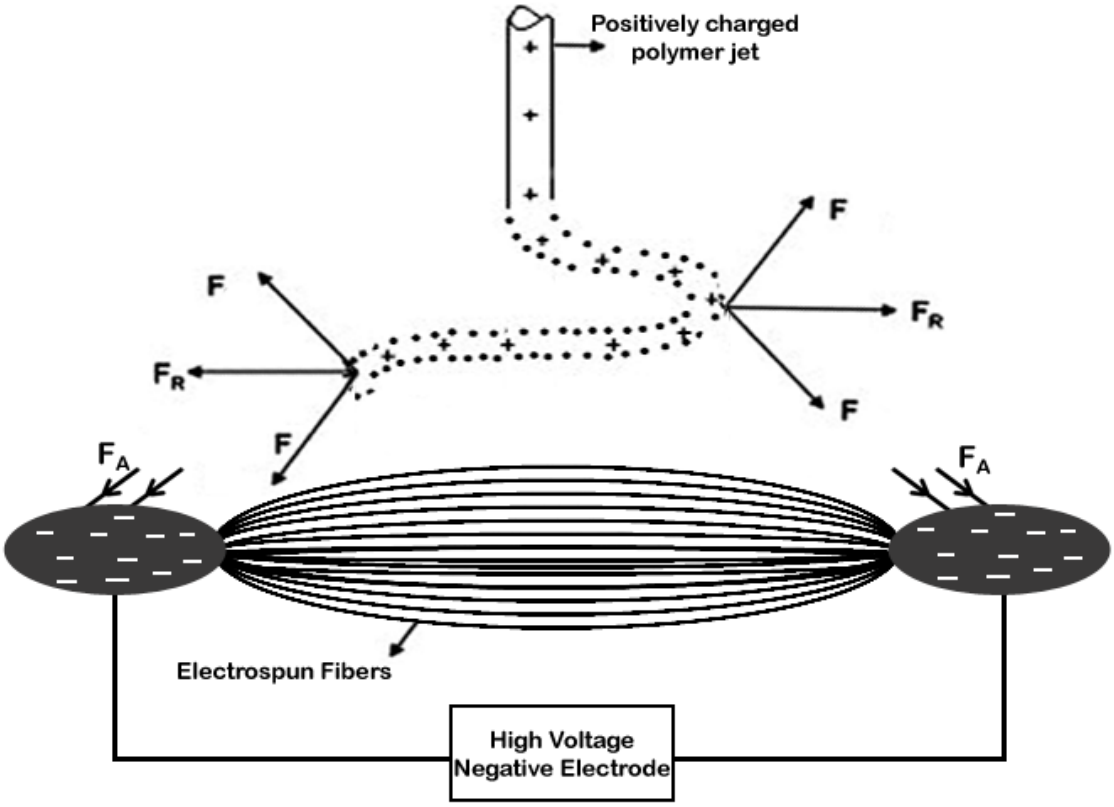

Figure 4.1: Schematic representation of the mechanism of two pole air gap electrospinning. The two metallic poles are separated by the air-gap. The length of the air-gap can be modulated, and is dependent on the characteristics of the electrospun polymer solution. As opposed to conventional electrospinning, where the entire fiber is deposited onto the target (usually a metallic disk), in two pole air gap electrospinning only the ends of the fiber loops closest to the poles adhere. The remaining fiber lengths are suspended between the poles producing an electrospun construct with highly aligned fibers along its longitudinal axis.

As detailed in Chapter 2, the electrospinning process consists of a syringe containing a positively charged electrospinning solution (or in some cases negatively charged) and a ground target (or an oppositely charged target). The charged jet from the Taylor cone undergoes coiling as it travels away from the needle and forms loops in the air (Figure 2.2A,B). In conventional electrospinning utilizing a collector plate as the target, the charged loops completely deposit on the target. In contrast, two pole air gap electrospinning utilizes two small, charged poles, approximating point-charges, as the target. The gap between the two poles of the target array constitutes the air gap. In this system, as positively charged loops of the fiber jet oscillate between the targets, they form alternating point-adhesions to the poles. The rest of the fiber (not depositing on the negatively charged poles) is suspended across the air-gap, creating an anisotropic 3D structure comprising of highly aligned fibers oriented nearly uniformly along the longitudinal axis of the construct (the direction in which in the regenerating axons need to be guided).

This electrospinning technique, like the conventional electrospinning process, has many variables which can be modulated to fabricate the construct comprising of the desired characteristics of fiber size, scaffold's porosity, scaffold's material strength and so on. This study describes the regulation of critical electrospinning variables present in a two pole system and the fabrication of constructs designed for use as nerve guides. The structural features, material properties and degree of fiber alignment present in the resulting constructs are evaluated. Finally, a series of tissue culture experiments are conducted to evaluate the extent to which axons can penetrate the fiber arrays, and we present the results of a pilot study done in the rodent designed to test the efficacy of using this design to treat in nerve injury.

Two pole air gap electrospinning: Fabrication of highly aligned, three-dimensional scaffolds for nerve reconstruction

Balendu S. Jha[1], Raymond J. Colello[1], James R. Bowman[2], Scott A. Sell[3], Kangmin D. Lee[4], John W. Bigbee[1], Gary L. Bowlin[5], Woon N. Chow[2], Bruce E. Mathern[4] and David G. Simpson[1]

[1]Department of Anatomy and Neurobiology
Virginia Commonwealth University
Richmond, VA 23298, USA

[2]School of Medicine
Virginia Commonwealth University
Richmond, VA 23298, USA

[3] McGuire Department of Veteran Affairs Medical Center,
Virginia Commonwealth University,
Richmond, VA 23298, USA

[4]Department of Neurosurgery
Virginia Commonwealth University
Richmond, VA 23298, USA

[5]Department of Biomedical Engineering
Virginia Commonwealth University
Richmond, VA 23298, USA

ABSTRACT

We describe the structural and functional properties of three-dimensional (3D) nerve guides fabricated from poly-ε-caprolactone (PCL) using the air gap electrospinning process. This process makes it possible to deposit nano-to-micron diameter fibers into linear bundles that are aligned in parallel with the long axis of a cylindrical construct. By varying starting electrospinning conditions it is possible to modulate scaffold material properties and void space volume. The architecture of these constructs provides thousands of potential channels to direct axon growth. In cell culture functional assays, scaffolds composed of individual PCL fiber diameter ranging from 400 to 1500 nm supported the penetration and growth of axons from rat dorsal root ganglion. To test the efficacy of our guide design we reconstructed 10 mm lesions in the rodent sciatic nerve with scaffolds that had fibers 1 μm in average diameter and void volumes > 90%. Seven weeks post implantation, microscopic examination of the regenerating tissue revealed dense, parallel arrays of myelinated and non-myelinated axons. Functional blood vessels were scattered throughout the implant. We speculate that end organ targeting might be improved in nerve injuries if axons can be directed to regenerate along specific tissue planes by a guide composed of 3D fiber arrays.

INTRODUCTION

After an injury, peripheral nerves can undergo an astounding degree of regeneration. When a nerve is severed, all signals distal to the injury site are immediately lost. Over time, downstream axons undergo Wallerian degeneration [33]. The surviving nerves of the proximal segment subsequently begin to undergo regeneration in response to soluble factors, many of which are produced by Schwann cells [34, 35]. If the precipitating injury cleanly severs the nerve, treatment may be confined to a surgery that is designed to re-establish the continuity between the truncated stumps of the damaged nerve. In this surgery the proximal and the distal aspects of the perineural sheath are sutured together to form an end-to-end anastomosis. In more extreme injuries where a long segment of the nerve is crushed or completely lost, treatment is greatly complicated. Under these conditions a conduit, or nerve guide, is used to bridge the gap and direct the regenerating axons to grow towards the distal stump.

Nerve guides have a relatively long clinical history; these tubular constructs are designed to direct the natural processes that lead to regeneration [36, 37]. A variety of natural and bioengineered materials have been used in this type of application, with mixed success [38]. Early synthetic guides consisted of a simple, hollow tube that provided little more than a protected environment [39]. Next generation nerve guides have been fabricated to contain signal molecules [40] and/or structural features [41] that are intended to provide guidance cues to the regenerating axons. Functional recovery with these constructs can be quite extensive, as long as the nerve guide is used to bridge a gap of less than about 10 mm in length. Once the injury gap exceeds this threshold (> 10 mm), the regeneration process will be compromised to varying degrees. Typically, in these injuries only a limited number of axons will actually traverse

the wound bed and the efficiency of targeting to the distal tissues is poor, resulting in limited functional recovery. Further exacerbating these complications, a series of irreversible degenerative changes begins to evolve in the distal tissues. As these degenerative changes become entrenched, the prospects of meaningful functional recovery are greatly diminished, even if a large number of axons are efficiently targeted to these sites.

Several published studies have demonstrated that aligned arrays of electrospun fibers can provide the guidance cues necessary to induce axons and glial cells to express a highly polarized phenotype [42-45]. Despite these preliminary and encouraging results, it is difficult to fabricate a clinically relevant nerve guide using the conventional electrospinning process, which uses a rapidly rotating target mandrel to produce aligned fibers. Conventional electrospinning systems are very effective at producing flat, two-dimensional (2D) sheets with highly anisotropic fibers [46-48]. These constructs are easily amenable to experimentation *in vitro*; however, a 2D sheet is less acceptable, or adaptable, for use *in vivo*. Despite these limitations, the efficacy of using the conventional electrospinning process to fabricate hollow, cylindrical nerve guides has been explored to some extent. In these experiments the electrospun fibers have been deposited onto a round, rotating mandrel. While the fibers of this type of construct can be induced to exhibit a considerable degree of alignment when produced under these conditions, the fibers, unfortunately, are deposited onto the target mandrel in a circumferential orientation (i.e. the axis of alignment is ~90° off with respect to the long axis of the hollow tube). For obvious reasons this architectural pattern does not lend itself well to providing guidance cues to regenerating axons. However, the nano-to-micron diameter fibers that form the wall of this type of construct do represent an effective barrier that reduces the risk of inflammatory cells penetrating into the

lumen of the guide. Blocking the infiltration of these cells into the lumen of a nerve guide is critical to the regeneration process [49, 50].

In our view, a more ideal nerve guide configuration closely mimics the structure of the autologous nerve graft. This idealized guide would display a cylindrical shape and be composed of dense three-dimensional (3D) arrays of highly aligned electrospun fibers that were oriented in parallel with the long axis of the construct. The gaps and elongated spaces that will exist between the stacked fiber arrays would literally provide thousands of channels for directed axonal growth. This type of configuration can be approximated by rolling a 2D sheet of aligned fibers into a cylinder. Although not tested, this design will result in a seam in the construct that could provide an avenue for the infiltration and penetration of inflammatory and interstitial cells into the construct. The seam could also represent a nexus for mechanical failure. Air gap electrospinning makes it possible to circumvent these limitations and produce cylindrical, seamless, and truly 3D constructs composed of aligned arrays of electrospun fibers that are oriented in parallel with the long axis of the cylindrical construct.

In this study, we characterize the air gap electrospinning process and examine how this fabrication technique can be exploited to produce nerve guides that facilitate the regeneration of peripheral nerve fibers. We chose poly-ε-caprolactone (PCL) as the polymer for the manufacture of the nerve guide owing to its slow rate of degradation [51]; thus it can act as a guide for the new axons throughout the nerve regeneration process. PCL was electrospun at varying concentrations for *in vitro* testing to determine the most appropriate air gap electrospinning variables for the manufacture of constructs suitable for directing the axons in peripheral nerve injuries.

METHODS

Electrospinning

PCL (Sigma-Aldrich: PCL 65,000 MW) was dissolved in trifluoroethanol (TFE) at various concentrations, including 50, 75, 100, 125, 150, 175, 200, 225, 250 and 275 mg mL^{-1}. Solutions were loaded into a 10 mL syringe that was capped with an 18 gauge blunt-tipped needle. Conductive, circular washers of varying diameters were placed over the blunt-tipped needle; several different electrospinning configurations were tested at each concentration of PCL. The air gap electrospinning system used in this study consists of two vertical piers grounded to a common voltage, typically set to −4.0 to −16.0 kV (Fig. 4.2, point A). From each vertical pier an additional set of horizontal piers project inwards at 90° with respect to the upright piers (Fig. 4.2, point B). A gap (which can be adjusted from about 1 to 6 inches) separates the terminal ends of these projecting piers. Electrospinning solutions were charged to +22 kV and directed into the gap separating the grounded horizontal piers. Polymer solutions were metered into the air gap system using a syringe driver with rates of delivery varying from 2 to 20 mL h^{-1} (see Table 4.1 for specific conditions). The distance between the solution reservoir and ground target array was varied from 10 cm to 30 cm. Once the charged electrospinning jet forms in this type of spinning, the polymer stream reaches the target and is laid out in a series of loops that pass back and forth between the terminal portions of the grounded piers, resulting in the formation of a bundle of parallel fiber arrays (Fig. 4.2, point C). Conditions for electrospinning at each PCL concentration were optimized to maximize fiber formation and collection onto the mandrel. We note that the electrospinning conditions disclosed in Table 4.1 are optimized to our specific laboratory environment (*e.g.*, 68 °F with ~40% humidity) and

electrospinning cabinet. Adjustments may be necessary to account for varying ambient conditions and different polymers.

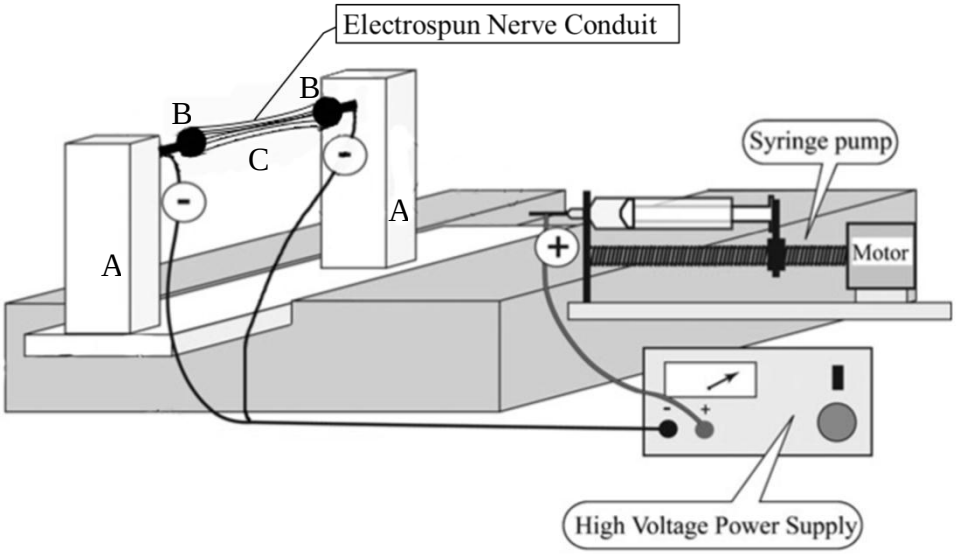

Figure 4.2: Schematic of the ground target used in a two pole air gap electrospinning system. (A) Vertical, hollow piers transmit ground wires to horizontal piers (B) that project inward towards one another. (C) Fibers accumulate across the gap that separates the two horizontal piers. The positions of the syringe and electrospinning source are relatively arbitrary and largely dependent upon the cabinet used for electroprocessing. For this study we positioned the electrospinning source parallel to the base of the ground device and at a height that corresponded to the height of the grounded horizontal piers (B).

Table 4.1: Summary of specific electrospinning conditions for PCL in the two pole electrospinning system. With increasing PCL concentration the target voltages, the electrospinning distance between the syringe reservoir and target as well as the distance between the poles of the air gap system must be reduced in order to induce fiber deposition across the poles.

Starting Concentration in TFE	Washer Diameter	Solution Voltage	Ground Voltage	Polymer Rate	Spinning Gap	Ground Target Gap
50 mg/ml	19 mm	+20 kV	-16 kV	9 ml/hr	25 cm	5 cm
75 mg/ml	19 mm	+20 kV	-16 kV	10 ml/hr	25 cm	6 cm
100 mg/ml	19 mm	+20kV	-20 kV	15 ml/hr	25 cm	6 cm
125 mg/ml	19 mm	+20kV	-10-12 kV	15 ml/hr	25 cm	6 cm
150 mg/ml	19 mm	+20kV	-7 kV	12 ml/hr	21 cm	6 cm
175 mg/ml	23 mm	+20kV	-7 kV	10 ml/hr	18 cm	6 cm
200 mg/ml	23 mm	+20kV	-7 kV	10 ml/hr	18 cm	6 cm
225 mg/ml	32 mm	+20kV	-7 kV	12 ml/hr	16 cm	5 cm
250 mg/ml	32 mm	+20kV	-5 kV	10 ml/hr	15 cm	5 cm
275 mg/ml	19 mm	+20kV	-3 kV	8 ml/hr	13 cm	5 cm

Scanning Electron Microscopy (SEM)

Electrospun constructs were removed from the target and cut into three sections of equal length. All the three segments, without any further processing, were mounted onto a scanning electron microscope studs and sputter-coated with gold for 2 minutes. A Zeiss EVO XVP scanning electron microscope equipped with digital acquisition was used for image capture. Average fiber diameter was determined from $N = 3–5$ SEM images captured at magnifications ranging from 450 to 5000× from each of the three sections using the NIH ImageTool software [49].

Fiber Alignment Analysis

Using the digital SEM images captured for fiber diameter analysis, the relative degree of fiber alignment was measured in each guide segment using the ImageJ 2D Fast Fourier transform (2D FFT) function [14, 46]. By using the 2D FFT approach an alignment plot can be generated. The height of the resulting peaks, read from the *Y*-axis, reports the degree of orientation in the data image. The position of the peaks on the *X*-axis reports the principal angle of fiber orientation [14, 46]. The FFT alignment data was normalized to the lateral edges of the cylindrical constructs which were arbitrarily assigned a value of 90° on the unit circle. The relative degree of fiber alignment and the principal angle of fiber orientation were determined for each of the construct formulations using the 2D FFT method.

2D FFT processing takes spatial information present in a data image and converts it into a "frequency" map. That frequency map essentially records the frequency at which pixels that are adjacent to one another change in contrast (the threshold of this change can be user selected). In essence it is a method of detecting edges. This property of the FFT "output" image makes it

possible to use this mathematical transformation to evaluate the alignment of objects that are present in the data image by determining how uniformly oriented the edges are in that image. The FFT image itself is composed of pixels that map the frequency at which contrast changes occur, in turn this information is a reflection of the degree of alignment that is present in a data image.

When a data image of electrospun fibers that are present in a random pattern is processed using the FFT, the resulting output image will be composed of pixels distributed in a symmetrical, circular shape centered in the middle of the FFT image (Image J FFT transformation, some FFT functions invert this relationship). The outlying areas of the FFT image will be black; the central area will contain white pixels (much like a map of an electron density map). The FFT "maps" low frequency pixels, data associated with the background of the image and other domains that contain pixels with a similar value, into the center of the image. This pattern is generated because changes in the intensity of adjacent pixels in a random image are theoretically similar in any direction. A 2D FFT function of an image containing aligned fibers (or other aligned elements) produces a frequency image that contains pixels distributed in a non-random, elliptical distribution that is centered in the middle of the image. This pattern develops because changes in pixel intensities in the data image are present in specific orientations. The high frequency pixels mapped on the FFT output corresponds to edges present in the data image; in an image of aligned structures the edges demark rapid changes in pixel intensity and they are preferentially oriented along a defined axis. Pixels along the fibers that are aligned do not change as there is no "edge"; those pixels are "oriented" along the fiber and define its shape. The elongated portions of the elliptical aspects of the FFT image are oriented at

90° with respect to the primary axis of orientation present in the data image. The extent to which the elongated aspects are distorted is proportional to the extent of alignment that is present.

The next step of the process is to quantify the extent of elliptical distortion that is present in the FFT image. This achieved by placing a circular projection on the FFT output image and then conducting a summation of the pixel intensities for each degree along a radial line running between 0° and 360° in 1° increments around the circular projection (*e.g.* summing the pixel value along each radius from 1 to 360°). For a random structure this process should produce a pixel summation that is essentially identical along any radius of the circle. Summing the radial projections for the aligned structures in the FFT image, which contain pixels mapped into the elliptical distortions, will produce different summations along each radius. The summed value will be higher along the orientation of the elliptical distortion (more pixels) and lower in the smaller and more circular aspects of the image.

In practice the summed radial values are then plotted as a scatter plot for each degree between 0° and 360°. Plotting data from a random image produces a graph containing four very low, broad peaks which correspond to the "edges" of the data image (these "spurious" peaks can be largely filtered out but for most applications this is not necessary). Data from images containing aligned structures have two much higher and narrowly defined peaks, and two corresponding to the off axis orientation-much smaller peaks-in this type of graphical depiction. In practice, the FFT data set is rotated 90° to allow the principal axis of orientation to be directly determined from the position of the peaks in the intensity plot. The amount of alignment is reflected by the height and overall shape of the peak present in this plot. For a complete discussion of the FFT method see the published and comprehensive review published by our laboratory in reference [14].

Materials Testing & Physical Properties

Materials strength was measured by uniaxially testing the constructs to failure at an extension rate of 10 mm min^{-1} using a Bionix 200 Mechanical Testing Systems instrument (MTS Systems Corp., Eden Prairie, MN). Cylindrical electrospun samples were prepared from variable concentrations of PCL (100, 150, 200 and 250 mg mL^{-1}; N = 4–6). Testing the material properties of an electrospun sample is typically done with a flat sheet of material, whereas our constructs are cylindrical in nature. To address this limitation, we elected to flatten the scaffolds and then cut out "dog-bone" shapes using a die punch (2.67 mm wide, gauge length of 0.295 mm). This approach, at least, allows us to use a configuration that controls for grip and geometry effects to evaluate how fiber diameter in each of our scaffolds contributes to their material properties. Specimen thickness was estimated using a Mitutoyo IP54 digital micrometer (Mitutoyo American Corp., Aurora, IL). In this study, we report stress at failure for these scaffolds [47]. Data sets were screened by One-Way Analysis of Variance (ANOVA; $p < 0.01$).

We quantified the physical properties of the scaffolds in terms of their overall void space. Cylindrical electrospun samples prepared from variable concentrations of PCL (100, 150, 200 and 250 mg mL^{-1}; N = 4–6) were tested using the liquid intrusion method of Pham et al. [52]. Scaffolds were electrospun, put under vacuum for 10 min and weighed ($W1$). Then, they were soaked in 90% ethanol for 10 min for initial hydration, and subsequently in distilled water for 30 min. Hydrated scaffolds were weighed ($W2$). The void space was calculated by dividing the volume of intruded water (as determined by the change in mass due to intrusion of water having density of 1 g mL^{-1}) by the total volume after intrusion:

$$\text{Percent Void Space} = \frac{W2 - W1}{W2} \times 100$$

Data sets were screened by Student–Newman–Keuls multiple pairwise comparison; $p < 0.05$.

Cell Culture

Dorsal root ganglion (DRG) explants were prepared from embryonic day 15 rats as described previously [53, 54]. PCL scaffolds for cell culture experiments were prepared from representative starting concentrations (125, 200, and 250 mg mL^{-1}). Scaffolds were soaked in 100% ethanol overnight, then rinsed in 70% ethanol, and then rinsed three times in sterile phosphate buffered saline (PBS). A 25-gauge needle was used to prepare an opening into the dorsal surface of each scaffold, and a single DRG was inserted into the resulting cavity. DRG explants were maintained for 7–10 days in media supplemented with 0.1 μg mL^{-1} NGF. Media was changed every other day.

Immunofluorescence Microscopy: DRG Explants

DRG explants were rinsed in PBS and fixed in 4% paraformaldehyde prepared in PBS. Samples were extracted in 0.1% Triton x-100 and immunostained with the neuron specific marker TuJ1 (Tubulin J1: MMS-435P, Covance, 1:500). Antibodies were diluted in PBS supplemented with 1% BSA and incubated with all samples overnight at 4 °C. Scaffolds were rinsed and counterstained with Goat anti-mouse antibodies conjugated with Texas Red (1:200). All samples were stained with 2% DAPI to reveal nuclei. A Nikon TE300 microscope equipped with a 10× objective and a DXM 1200 digital camera was used to capture images at a pixel resolution of 3840 × 3072. Individual images of the DRG explants were assembled into montages using Adobe Photoshop software.

Electrospinning for *in vivo* Experimentation

For implant studies, nerve guides were electrospun from a starting concentration of 200 mg mL^{-1} PCL using optimized conditions (Table 4.1). To reduce inflammatory cell infiltration into the fiber arrays of the guide, an exterior coating of PGA:PLA (50:50) copolymer was electrosprayed (100 mg mL^{-1} in TFE) onto the outside of the completed constructs. This was achieved by placing a circular, 120 mm diameter steel plate directly behind the completed nerve guide. To process the PGA/PLA copolymer an alligator clip was attached to the electrospinning source syringe (no washer was used) and charged to +22 kV; the steel plate was charged to −2 kV for collection. By placing the completed nerve guide between the electrospinning source solution and the grounded steel plate, the fibers of PGA/PLA copolymer deposit on the surface of the nerve guide construct, forming a barrier that is designed to limit the penetration of interstitial cells into the reconstructed nerve *in vivo* [49].

Surgery

All surgical and postoperative care procedures were performed in accordance with the Virginia Commonwealth University Institutional Animal Care and Use Committee. Nerve guides were prepared from starting concentrations of 200 mg mL^{-1} for preliminary implant studies. Adult (70–90 day) Long Evans Hooded rats (Harlan laboratories) (N = 3) were intubated and brought to a surgical plane with 2.5% isoflurane. Body temperature was kept normothermic using a homeothermic blanket. Hair was removed from the hindquarters, and skin was swabbed with betadine. Using sterile techniques, skin and muscle overlaying the sciatic nerve were mobilized, and a 10 mm segment of the nerve was excised. This interval represents a critical threshold in short term regeneration experiments that can be used to characterize the efficacy of a

candidate guide in the rodent model. Electrospun nerve guides were sutured to the distal and proximal stumps of the injured tissue using 10-0 nylon sutures (Ethicon Inc., USA). At the conclusion of surgery, skin incisions were stapled and the animals were allowed to recover on a warming pad. After surgery all animals were given free access to food and water and housed two per cage. Analgesic medication (Tylenol oral suspension, 2 mg mL^{-1}) was mixed into the drinking water and administered for the first 3 days post-surgery.

Immunofluorescence Microscopy: Implanted Nerve Guides

Tissue was immersed for 2 hr in 4% paraformaldehyde prepared in PBS at room temperature and then incubated overnight in 30% sucrose prepared in PBS at 4 °C. The samples were frozen and cut into 30 μm thick sections for staining. Primary antibodies, including S100 (Schwann cell marker, Dako, Denmark, 1:500), MBP (Myelin basic protein, SMI-99, Covance, 1:1000), and NF-68 (Neurofilament 68, Sigma-Aldrich, 1:1500) were incubated on the sections overnight at 4 °C. Samples were rinsed in 0.5% Triton x-100, and counterstained with Goat anti-mouse or Goat anti-rabbit secondary antibodies (Alexis) (1:200) for 60 min at room temperature. 2% DAPI was used to image the nuclei.

Tissue Processing

After 7 weeks, animals were sacrificed with a lethal dose of pentobarbital (Sigma–Aldrich, St. Louis, MO), and the nerve implants were harvested for microscopic analysis. Tissue was recovered and immersed in 2% glutaraldehyde plus 2% paraformaldehyde for 12 h at 4 °C and post fixed in 1.0% osmium plus 2.5% potassium ferricyanide. Samples were subjected to a graded series of dehydration in alcohol (starting with 50% ethanol for 15 min, then 70% ethanol

for 15 min, next 95% ethanol for 15 min, then 100% ethanol 2× for 15 min). Samples were next embedded in Poly/Bed (Polysciences). We note that it is difficult to get good plastic infiltration into the dense matrix of an electrospun scaffold that has been densely populated by cells; air bubbles are often trapped and interfere with subsequent processing. To overcome this limitation, we place our samples under a vacuum during the final infiltration step. Vacuum was applied to the samples until air bubbles visibly evolved from the samples. Then the samples were kept at this vacuum level for 1 hr.

A Leica EM UC 6 ultramicrotome was used to make semi-thin sections of 0.5 μm for morphometric studies and to make ultrathin sections of about 60-70 nm for TEM imaging.

Morphometric Analysis

We sampled the proximal domains that were 1 mm into the reconstructed tissue and the distal domains 1 mm proximal to the distal border of the lesions. Semi-thin sections were prepared and stained with a solution of 0.1% Toluidine Blue, 0.1% Methylene Blue, 0.1% Azure II in 1% sodium borate. To determine the total number of axons passing through the implants, a montage of the complete cross-sectional area of the graft was prepared from images captured with 10× bright-field objective lens and a Nikon TE300 microscope. The images were imported into the ImageTool (UTHSCSA version 3.0) to measure the area encompassed by the fibrotic capsule (induced by the PGA/PLA coating). Total axon number was determined for a series of images captured at systematic intervals of approximately every 500 μm throughout the nerve cross-section using a 100× oil immersion lens. The number of myelinated axons present in each data image was determined by non-biased sampling methods. Each individual raw data image covered an area of 125 μm × 125 μm and was subdivided into a series of twenty five

25 μm × 25 μm squares using a 5 × 5 grid. Of these twenty five squares in each raw image, alternate squares were used for morphometrics, *i.e.* of the total twenty five squares in each raw image, either twelve or thirteen squares were used for myelinated axons counts depending on whether the first square was included for the analysis or not. The raw data images from each cross-section sample were divided into two groups. In images of the first group, the first square was included in the analysis, resulting in thirteen squares for axon counts from those images; in the second group the not the first, but the second square was included in the analysis resulting twelve squares for axon counts from those images. Additionally, the myelinated axons touching the top and the left border of each square were excluded from the counts and the myelinated axons touching the bottom and the right border of each square were included in the count. To extrapolate the total number of axons present in the cross-sectional area, the density of myelinated axons in the sampled images was multiplied by the total cross-sectional area of the grafts. All measurements were calibrated with a stage micrometer.

Electron Microscopy

Ultrathin sections were obtained after tissue processing as detailed above and all ultrastructural analyses were conducted with Jeol-1230 electron microscope equipped with a Gatan UltraScan 4000SP 4K x 4K CCD camera.

RESULTS

Electrospinning Characteristics and Fiber Properties

The discussion concerning fiber properties is subdivided into three sections based on starting conditions and electrospinning characteristics. Overall, the average fiber diameter of the scaffolds produced varied as a function of the starting conditions ([Fig. 4.3] and [Fig. 4.4]).

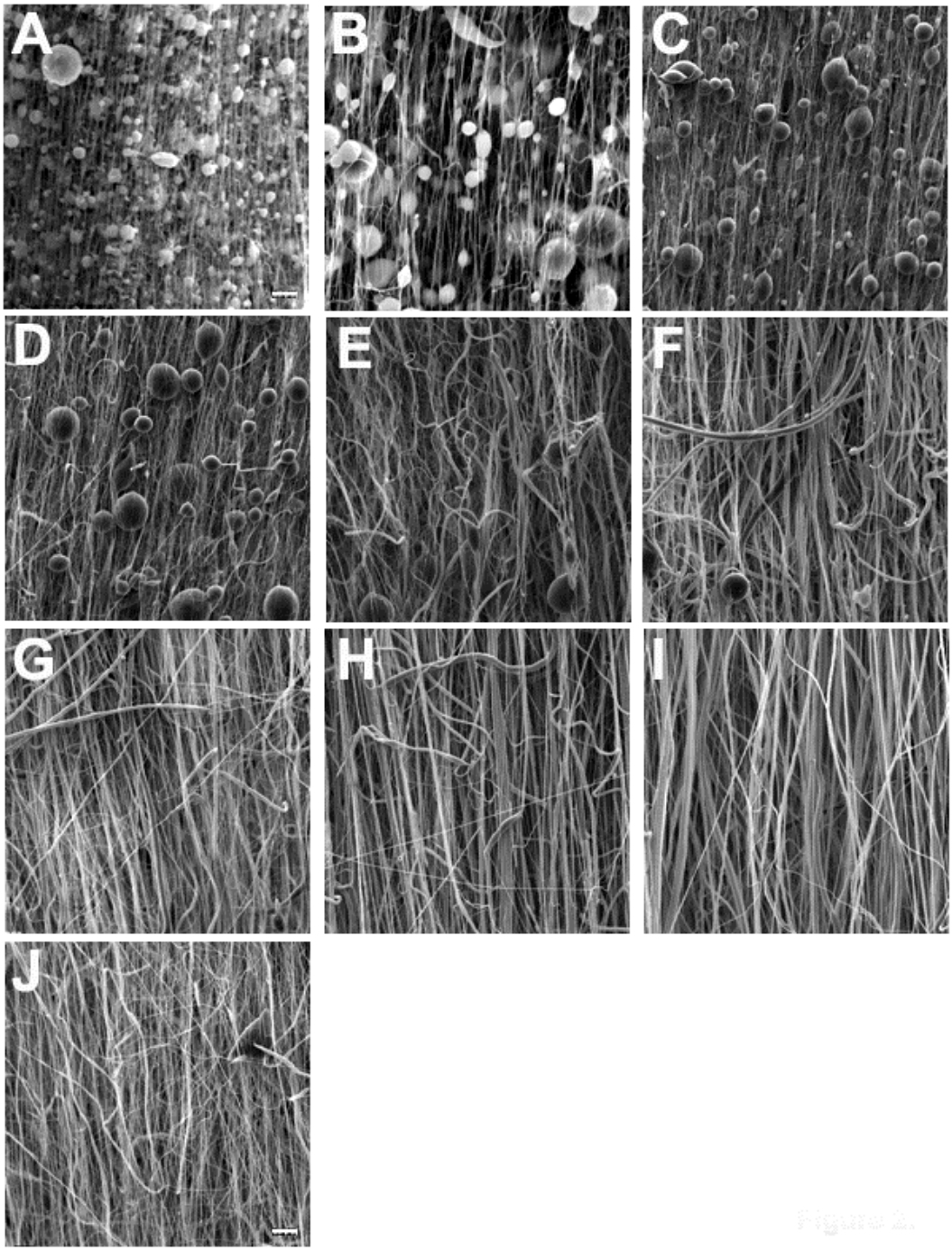

Figure 4.3: Representative scanning electron micrographs (SEM). (A) SEM of scaffolds produced from 50 mg mL^{-1} starting concentrations using air gap electrospinning. Note that even heavily beaded scaffolds exhibit aligned fibers. (B) Scaffolds produced from 75 mg mL^{-1}, (C) 100 mg mL^{-1}, (D) 125 mg mL^{-1}, (E) 150 mg mL^{-1}, (F) 175 mg mL^{-1}, (G) 200 mg mL^{-1}, (H) 225 mg mL^{-1}, (I) 250 mg mL^{-1}, (J) 275 mg mL^{-1}. All images captured at 1000× magnification. Scale in (J) for (A)–(J) = 20 μm.

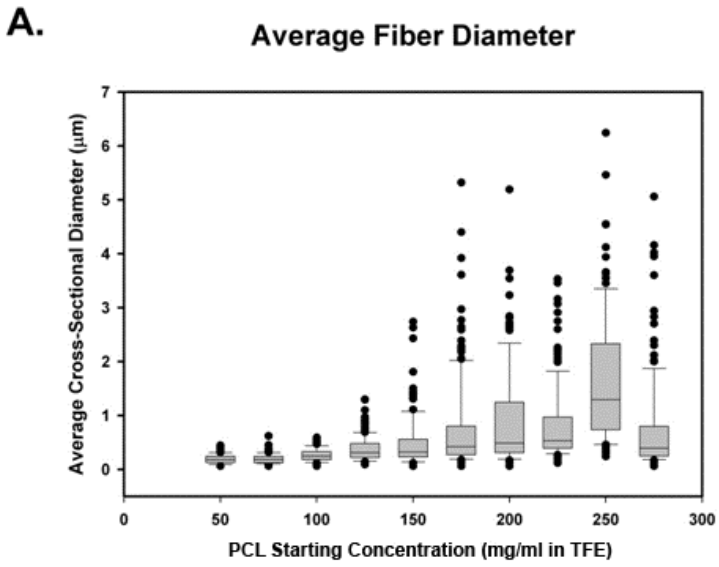

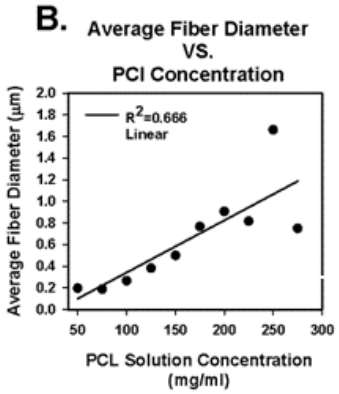

C.

	50	75	100	125	150	175	200	225	250	275
50	NA	XXX	0.001	0.001	0.001	0.001	0.001	0.001	0.001	0.001
75		NA	0.001	0.001	0.001	0.001	0.001	0.001	0.001	0.001
100			NA	0.001	0.001	0.001	0.001	0.001	0.001	0.001
125				NA	XXX	0.001	0.001	0.001	0.001	XXX
150					NA	XXX	0.001	0.001	0.001	XXX
175						NA	XXX	XXX	0.001	XXX
200							NA	XXX	0.001	XXX
225								NA	0.001	XXX
250									NA	XXX
275										NA

Figure 4.4: Average fiber diameter. (A) Average cross-sectional fiber diameter varied as a function of starting conditions. Of note in the graphical representation the range of fiber diameters also increased with increasing polymer concentration. (B) Average fiber diameter as a function of starting PCL concentration. From 50 to 200 mg mL^{-1} PCL average fiber diameter increased in a nearly linear fashion (linear regression analysis over this specific range of concentrations: $R^2 = 0.918$); however, at concentrations above 200 mg mL^{-1} this relationship markedly deteriorated. Overall, for the entire range of starting concentrations that we investigated a quadratic equation best described the relationship between starting concentration and average fiber diameter, although even in that analysis the data represented a poor fit, at best ($R^2 = 0.666$). (C) Summary of pairwise comparisons across all treatment groups. The broad range of fiber diameters present in the scaffolds produced from 275 mg mL^{-1} solutions exhibited substantial overlap with a variety of other scaffolds. Scaffolds produced from this starting concentration had fibers that were not statistically different than scaffolds produced from the 125, 150, 175, 200, 225 and 250 mg mL^{-1}.

Starting Solutions 50-100 mg/mL. At concentrations ranging from 50 to 100 mg mL^{-1} PCL, there was nominal to poor fiber formation and fiber collection. Fibers appeared to coalesce out of an amorphous cloud of material that collected in the vicinity of the target grounds. These scaffolds exhibited extensive beading; these beads were interconnected with an array of small diameter fibers that were oriented in parallel with the long axis of the cylindrical scaffolds (Fig. 4.3A–C). Macroscopically, these cylindrical constructs were predominately composed of aligned elements (Fig. 4.5).

Beaded structures can form in an electrospinning field as a consequence of Rayleigh instabilities that develop in the charged jet as a result of: (a) inadequate flow rates of the electrospinning solution; (b) electric field effects; (c) inadequate polymer chain entanglements in the solvated spinning solution and; (d) too low a starting polymer concentration [55]. Increasing the flow rate of the polymer solution into the electric field did not suppress bead formation in these scaffolds. Instead, increased flow rates resulted in the accumulation of a dense cloud of solvent in the vicinity of the target which prevented fibers from forming altogether. Nor was the formation of the beaded structures visibly altered by directly altering the potential of the electric field, manipulating the distance between the syringe reservoir and ground targets, or by changing the diameter of the washer used to direct the charged electrospinning jet at the bi-polar target (key elements of specific electrospinning conditions are summarized in Table 4.1). Given these results it is clear that a 50 mg mL^{-1} starting solution represents the near absolute minimal threshold concentration for fiber formation to take place in this particular air gap electrospinning system.

Starting Solutions 125-200 mg/mL. Over this range of starting concentrations average fiber diameter increased and was more heterogeneous with respect to the fibers electrospun from

the 50–100 mg mL^{-1} solutions (Fig. 4.4). As the starting PCL concentration was increased beyond 125 mg mL^{-1} the beaded structures present in scaffolds produced from the lower starting concentrations became increasingly less apparent (Fig. 4.3). Average fiber diameter in scaffolds produced from the 125 mg mL^{-1} solutions was 382 nm; these fibers ranged from 90 nm to 1.3 μm in cross-sectional diameter. Scaffolds produced from the 200 mg mL^{-1} solutions had an average fiber diameter of 906 nm with a range of 60 nm to more than 5.1 μm in average cross-sectional diameter.

The visible components of the electrospinning field changed dramatically over this range of starting concentrations. At 125 mg mL^{-1}, the charged electrospinning jet was distinct and composed of a continuous jet of material that emanated from the syringe tip; this jet was several centimeters in length. As the charged jet approached the targets it became unstable and fibers appeared to form out of an amorphous cloud of material. As the starting concentration was increased to 150–200 mg mL^{-1} the charged jet appeared as a distinct series of spiraling loops that originated from a prominent Taylor cone. The appearance of this stable jet coincided with a marked reduction in bead formation, a physical property indicating that sufficient polymer chain entanglements are present in the solvated spinning solution to suppress the Rayleigh instabilities observed at lower polymer concentrations. The spiraling jet of material was directed towards the gap between the two poles of the air gap system. Fibers formed in the immediate vicinity of the grounded piers and were visibly collected across the gap separating the two grounded targets. As additional fibers collected across the targets, the pre-existing fibers collapsed into a much more compact cylindrical structure. With the formation of the spiraling jet of charged material it was necessary to reduce the distance between the electrospinning source reservoir (syringe) and the grounded targets (Table 4.1). Fiber deposition was optimized when the apparent diameter of the

spiraling jet coincided with the distance between the piers of the bi-polar ground. Under these conditions fibers were observed to rapidly accrue on the ground targets.

Starting Solutions 225-275 mg/mL. The relationships between the starting solution properties and final fiber properties were less well defined in scaffolds produced from starting concentrations greater than 200 mg mL^{-1} (Fig. 4.4B). Scaffolds spun from the 225, 250, and 275 mg mL^{-1} solutions exhibited marked heterogeneity in fiber size (Figs. 4.3H–J and 4.4). For example, scaffolds produced from the 225 mg mL^{-1} solutions had an average fiber diameter of ~816 nm with a range from 120 nm to ~3.5 μm (Fig. 4.4). At 250 mg mL^{-1} average fiber diameter increased to 1.7 μm and the scaffolds exhibited fibers ranging from 240 nm to 6.2 μm (Fig. 4.4). Average diameter in scaffolds prepared from the 275 mg mL^{-1} solutions decreased to 750 nm, substantially less than the average fiber diameter observed in scaffolds prepared from starting solutions ranging from 125 to 250 mg mL^{-1} (Fig. 4.4).

In order to fabricate scaffolds from the 225 and 250 mg mL^{-1} solutions it was necessary to increase the diameter of the washer used to direct the electrospinning jet towards the grounded target. We suspect that the mass and momentum of the electrospinning jet at these higher starting concentrations restrict its lateral deviations as the jet passes from the syringe to the air gap targets. As we increased the diameter of the washer placed over the syringe, the lateral deviations in the spiral jet increased and fibers collected across the grounded piers, forming a cylindrical construct. In parallel with this change, it was also necessary to (a) move the grounded targets closer to the electrospinning reservoir, and (b) reduce the distance between the piers of the bi-polar ground (Table 4.1). These modifications appear to bring the targets within a domain of the electrospinning field that corresponded to the diameter of the spiraling jet of charged polymer.

Fiber Alignment

2D FFT analysis was used to quantify the electrospun scaffold's fiber alignment. This analysis does not provide an absolute value to determine the degree of alignment, but the values generated are relative to each other, thereby indicating the relative orientation of the fibers in comparison to the other fibers in that assay. The FFT analysis of the different scaffolds produced in this study demonstrates that fiber alignment is similar, regardless of fiber diameter, when scaffolds are produced using a bi-polar grounded target (in contrast to scaffolds produced in a conventional electrospinning system where fiber diameter and rates of mandrel rotation interact to determine the extent of alignment). In contrast to conventional systems, varying the PCL concentration and/or increasing the average fiber diameter had little effect on fiber alignment in scaffolds produced by the air gap system (Fig. 4.5D and E). Not surprisingly, the principal angle of fiber alignment in all of these scaffolds was in parallel with the long axis of the cylindrical constructs (Fig. 4.5). However, there were some subtle differences across the samples that we examined. Scaffolds produced from the 50–100 mg mL^{-1} solutions contained structural elements that partially degraded alignment values. These scaffolds each exhibited a characteristic shoulder in the 2D FFT alignment plot (occurring at about 180°). The beaded structures and the off axis fiber that are present in this family of scaffolds undoubtedly contribute to these results (Fig. 4.3). Even so, these scaffolds still exhibit considerable fiber alignment, and for this family of constructs the 2D FFT analysis generated alignment values ranging from 0.14 to 0.16 units (Fig. 4.5A). The 2D FFT analysis reported that constructs produced from starting concentrations of 125–200 mg mL^{-1} lacked the distinct shoulder detected in scaffolds produced from lower starting concentrations of PCL. Overall, these scaffolds were incrementally more aligned than scaffolds produced from the 50–100 mg mL^{-1} solutions (Fig. 4.5B). A similar trend

was observed in scaffolds prepared from the starting solutions of 225–275 mg mL^{-1} and these samples displayed the highest degree of fiber alignment (Fig. 4.5C).

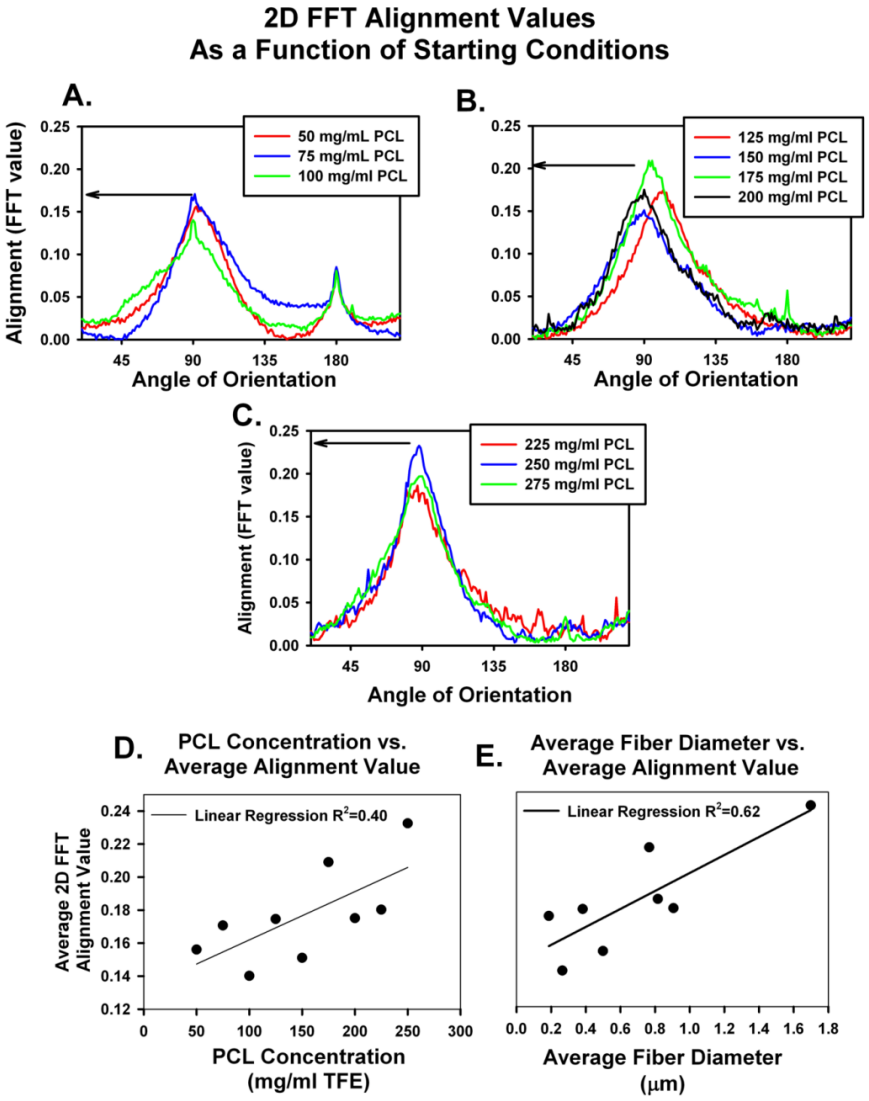

Figure 4.5: Analysis of fiber alignment by 2D FFT. (A) Average fiber alignment over the entire length of constructs produced from 50-125 mg mL^{-1} solutions; (B) 150-200 mg mL^{-1} solutions; and (C) 225-275 mg mL^{-1} solutions. Average fiber alignment is similar in each construct, although there is a trend towards an increase in the peak FFT value as a function of increasing average fiber diameter. Scaffolds produced from the 50 and 75 mg mL^{-1} starting concentrations exhibit a broader distribution of alignment values and shoulders on the FFT plots (illustrated at 180° on the alignment plot) typical of structures that degrade alignment values (beads and fibers off axis). (D) Fiber alignment as a function of initial starting PCL concentration. (E) Fiber alignment as a function of average fiber diameter. These data indicate that increasing fiber diameter has a relatively nominal effect on increasing alignment in the electrospun constructs as the FFT values are similar and not distinguishable from one another.

Materials Testing and Physical Properties

To verify the structural properties of scaffolds produced in the air gap process we conducted materials testing experiments (stress at failure increases as a function of fiber alignment in electrospun materials, see reference [47]). 2D FFT analysis indicates that fiber alignment incrementally increased as a function of starting PCL concentration (and increasing fiber diameter). A similar trend was noted in the bulk material properties of the scaffolds (Fig. 4.6). For example, peak stress in scaffolds produced from the 100 mg mL^{-1} solutions was ~2.00 MPa. This value increased to 3.25 MPa in scaffolds produced from the 150 mg mL^{-1} solutions, and to 4.25 MPa in scaffolds produced from 200 mg mL^{-1} solutions. Peak stress was 3.5 MPa in scaffolds produced from the 250 mg mL^{-1} solutions. Statistical analysis of these data indicates that scaffolds produced from 150, 200 and 250 mg mL^{-1} PCL exhibited similar material properties at failure. Peak stress in each of these constructs was greater than what was observed in scaffolds produced from 100 mg mL^{-1} PCL ($p < 0.007$). These values, with the exception of scaffolds produced from the 100 mg mL^{-1} solutions, compare favorably to the material properties of native rodent sciatic nerve [56].

While each scaffold is composed of highly aligned fibers, considering the variable fiber diameters, the spaces between each of the individual fibers can be expected to be very different, which would influence the penetration of regenerating axons. Our analysis, as determined by liquid intrusion measurements, revealed significant differences in scaffold void space ("porosity") develop as a function of starting conditions ($p < 0.05$; Fig. 4.6B). Average void space for scaffolds produced from 100 mg mL^{-1} solutions was ~58% and ranged to greater than 95% for scaffolds produced from the 250 mg mL^{-1} starting solutions.

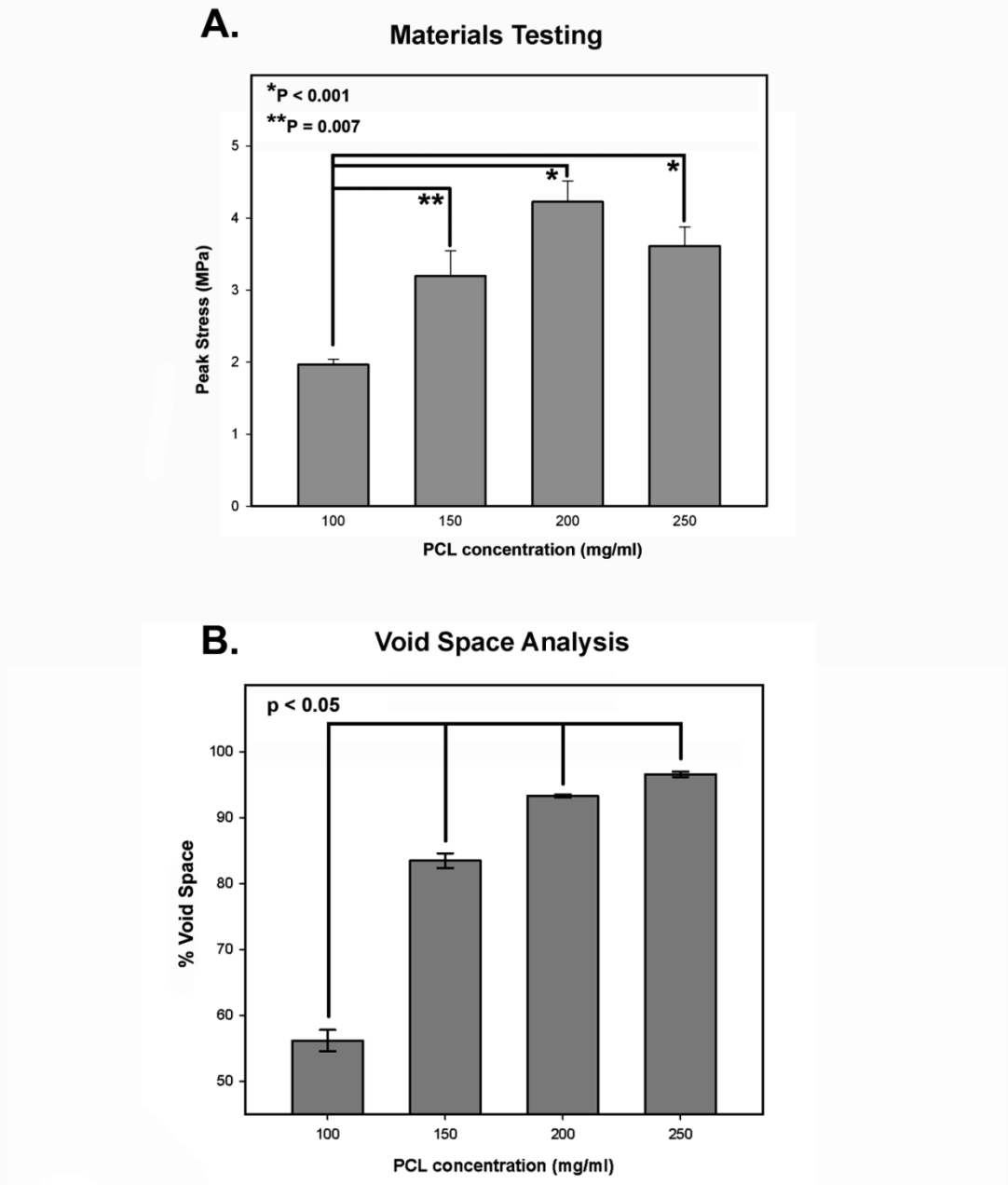

Figure 4.6: Materials testing. (A) Peak stress of electrospun constructs produced from varying concentration of PCL (100, 150, 200, and 250 mg mL^{-1}). The peak stress of the scaffolds increases with the increasing concentration of PCL from 100 to 200 mg mL^{-1}. At 250 mg mL^{-1}, the strength of the construct is qualitatively reduced, but not statistically different, with respect to scaffolds electrospun from PCL at a concentration of 200 mg mL^{-1}. (B) Void space in electrospun constructs produced from varying PCL concentrations (100, 150, 200, and 250 mg mL^{-1}) measured using the liquid intrusion method. The percentage of void space increased with increasing concentration of PCL ($p < 0.05$).

Cell Culture Experiments.

While each of the scaffolds produced in this study did exhibit similar degrees of fiber alignment, there are additional considerations that must be accounted for in the selection of a candidate construct that is to be used in nerve reconstruction. For example, scaffolds produced from 50–100 mg mL^{-1} PCL exhibit extensive beading and tensile properties that are below that of the rat sciatic nerve [56]. The beaded structures could represent obstacles to regenerating axons and or disrupt guidance cues present in the aligned fibers. At the other extreme, scaffolds produced from the 275 mg mL^{-1} solutions have highly aligned arrays of fibers and material bulk material properties that exceed the sciatic nerve of the rodent. However, the electrospinning configuration that is necessary to process these solutions into a scaffold results in very short constructs, limiting their utility in a clinical application.

An additional consideration regarding the physical properties of the constructs concerns how the functional porosity of scaffolds affects axonal regeneration. In these cell culture assays we tested how effective different scaffold configurations were at supporting the penetration of axons into the fiber arrays using explanted DRGs as a model system. We elected to test scaffolds produced from the 125 (average fiber diameter = 383 nm ± 228 nm SD), 200 (906 nm ± 923 nm) and 250 (1667 nm ± 1165 nm) mg mL^{-1} PCL starting concentrations in these assays.

DRGs were implanted directly into the cylindrical scaffolds (scaffolds were prepared with a length of 10–15 mm and 5–7 mm in diameter) and cultured for 7 days in the presence of NGF. At the conclusion of this experimental interval all the scaffolds exhibited axons that projected into and parallel with the surrounding fiber arrays (Fig. 4.7D–F). These experiments suggest that constructs composed of smaller diameter fibers foster the penetration of numerous individual axons along individual PCL fiber tracks (or perhaps more accurately within the pore

spaces). This pattern was particularly evident in DRGs cultured in the scaffolds prepared from the 125 mg mL^{-1} starting solutions. At the other extreme, DRGs plated into scaffolds prepared from the 250 mg mL^{-1} solutions exhibited pronounced fasciculation (Fig. 4.7F). In these cultures the axons appeared to interact with one another, form bundles and then pass along far fewer fiber tracks. A nuclear stain of the explanted cultures revealed that cells associated (Schwann cells and interstitial fibroblasts) with the DRGs heavily infiltrated the scaffolds and tracked in association with the DRG axons (Fig. 4.7G).

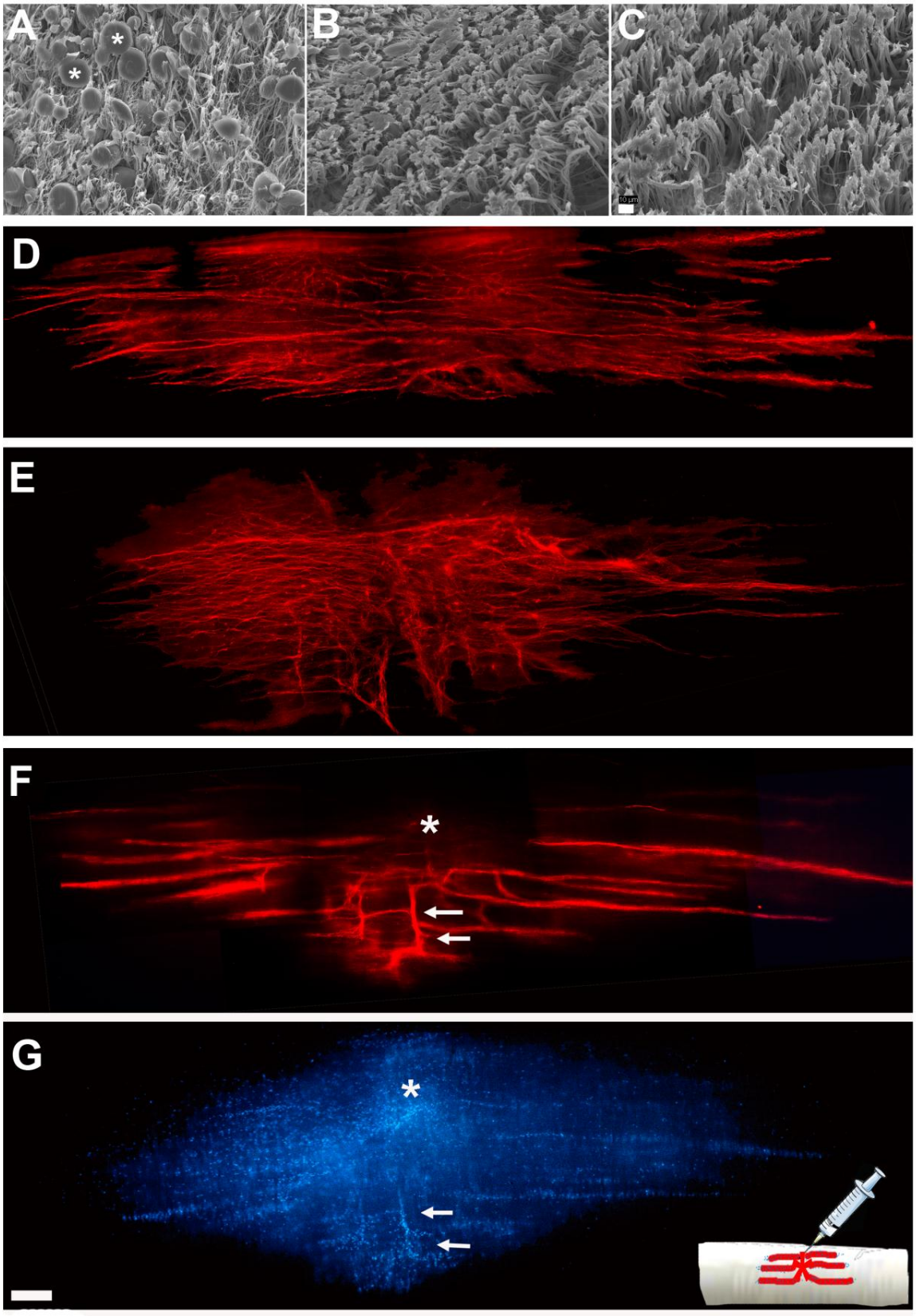

Figure 4.7: Cell culture experimentation.

Figure 4.7: Cell culture experimentation. (A) SEM tangential sections of scaffolds produced from 125 mg mL^{-1}, (B) 200 mg mL^{-1} and (C) 250 mg mL^{-1}. While there is evidence of fiber damage and some compression in the cut zones note the high porosity of the constructs that is present in parallel with the axis of fiber alignment. Scaffolds produced from the 125 mg mL^{-1} solutions have the beaded structures typical of these constructs ((a), asterisks, see also Fig. 4.3). Scale bar in (C) = 10 μm for (A)–(C). (D) Fluorescence images of DRG in scaffold produced from the 125 mg mL^{-1} solution. (E) 200 mg mL^{-1} solution and (F) 250 mg mL^{-1} solutions. Note the increasing trend towards fasciculation with increasing PCL fiber diameter. This effect is particularly evident in the samples cultured in the scaffolds produced from the 250 mg mL^{-1} solutions. The axons that are projecting perpendicular to the primary axis of the construct are within the channel used to implant the DRGs into the scaffold (arrows in (F) and (G)). (G) corresponds to (F) stained to reveal nuclei. Note the extensive overall cellularity of the cultures and the association of nuclei with the axons bundles. The asterisks in (F) and (G) represent the initial implant site for the DRG. Inset in (G) represents an illustration regarding the method and site of DRG injection into the scaffolds. Bar in (G) represents 100 μm in (D)–(G).

Preliminary Peripheral Nerve Reconstruction Experiments.

For *in vivo* testing, we prepared nerve guides from the 200 mg mL^{-1} starting concentrations of PCL. This construct formulation exhibited highly aligned fibers, excellent material properties and extensive void spaces to support the penetration of axons along individual. In these experiments, a 10 mm section of the right sciatic nerve was removed and replaced with an electrospun nerve guide.

During the 1–2 weeks after surgery, the lesioned animals walked on three limbs and carried the injured limb. Motion at the knee and distal joints was substantially absent. After 3–4 weeks the animals carried weight on the injured leg, but gait in this limb was characterized by a pronounced abduction at the hip. By 6 weeks, gait improved and the exaggerated abduction at the hip was replaced with motion in more normal planes as mobility increased at the knee and ankle joints. At this time point, the animals also responded to a sensory stimulation in the guise of a withdrawal reflex in response to a foot pinch. Given these results, we elected to recover our implants 7 weeks after the initial surgical reconstruction.

At recovery the implanted nerve guides were visibly well integrated with the stumps of the transected nerves (See Fig. 4.8A). The guides lifted easily out of the surrounding tissue, and there was very little evidence of fibrosis on, or in the vicinity of, the implant sites. Frozen sections taken from the mid-point of the regenerating tissue had a pronounced anisotropic structure and were densely populated with cells (Fig. 4.8B, C). Staining for NF-68 revealed a dense population of axons in the regenerating tissue. These axons were aligned in parallel with the long axis of the cylindrical nerve guides (Fig. 4.8D). Myelin basic protein was present in a dense fibrillar pattern (Fig. 4.8E). Staining for S100 revealed elongated Schwann cells that were aligned in parallel with the long axis of the regenerating tissue (Fig. 4.8F). Together, the staining

patterns for S100 and MBP suggest that a subset of the axons present in these central domains (of the implants) is actively undergoing myelination.

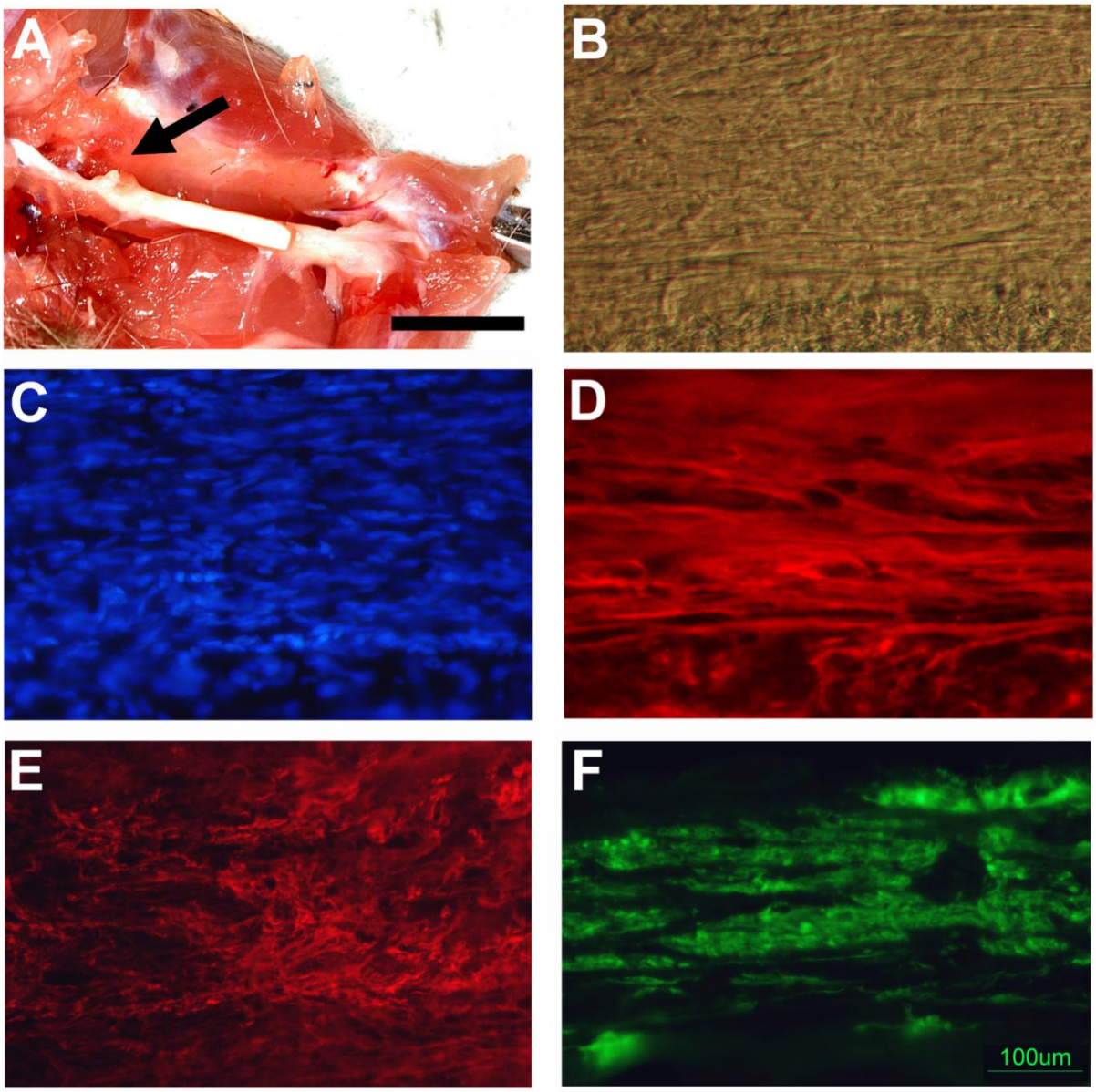

Figure 4.8: Nerve reconstruction – frozen sections. (A) is a representative implant recovered after 7 weeks *in vivo*. Arrow indicates the proximal attachment site of the implant. The guides were well integrated into the tissue of the damaged nerve. Bar in (A) = 10 mm. (B) Nomarski image of frozen sections taken mid-point in guide. Note the anisotropic nature of the tissue. (C) DAPI staining, (D) neural filament 68 (NF-68), (E) myelin basic protein (MBP), and (F) S100 Schwann cell marker. (B)–(F) captured with 40× objective. Bar in (F) = 100 μm for (B)–(F).

To verify the architectural organization of the reconstructed nerves, we embedded representative samples for light and transmission electron microscopy, and cut them in cross-section. Semi-thin sections imaged by light microscopy revealed that the proximal segments of the nerve guides that were densely packed with myelinated axons. These axons were more variable in size than axons present in a normal sciatic nerve (see Fig. 4.9A and B). Non-myelinated axons were interspersed with the myelinated axons (Figs. 4.9C, arrows and 4.10A). The PGA/PLA coating that we used on the implants induced the formation of an epineurium-like capsule (Fig. 4.9D). Samples taken from the mid-point of the grafts exhibited numerous bundles of axons that were surrounded by a delimiting band of tissue that was reminiscent of the perineurium (Fig. 4.9E). Cells with an elongated, spindle-like morphology were present in association with the periphery of these fascicule-like structures (Fig. 4.10C, arrow). Functional blood vessels, as indicated by the presence of red blood cells (Fig. 4.9C, asterisk and Fig. 4.10B), were observed at scattered intervals within the reconstructed tissue.

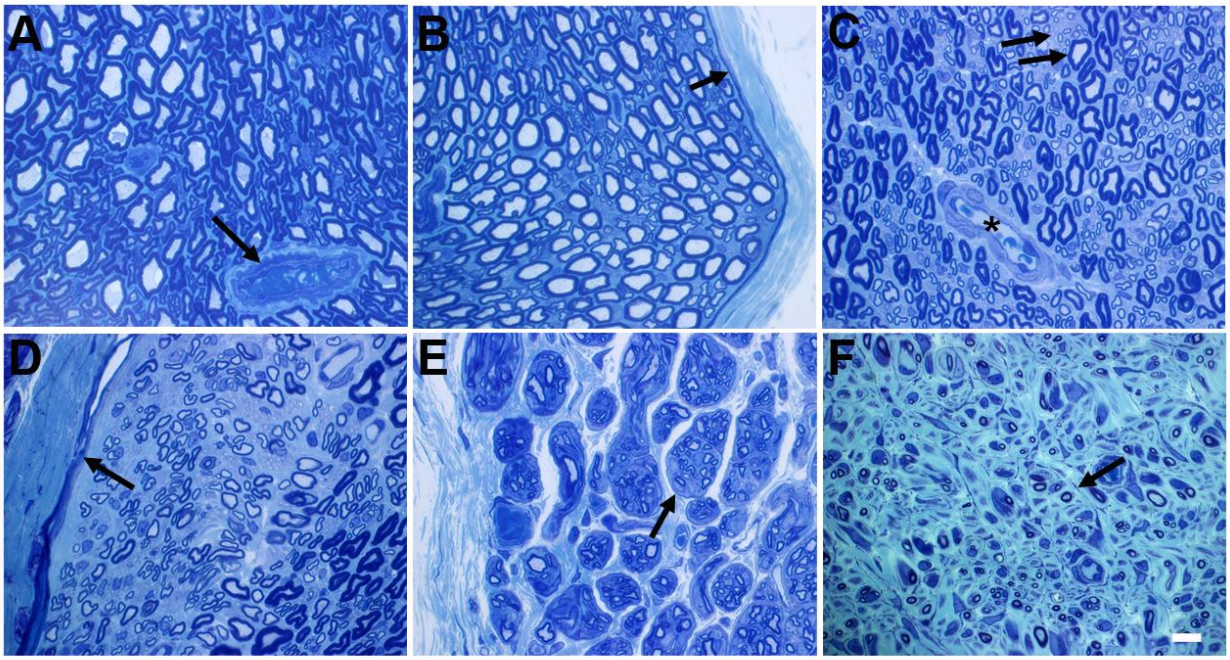

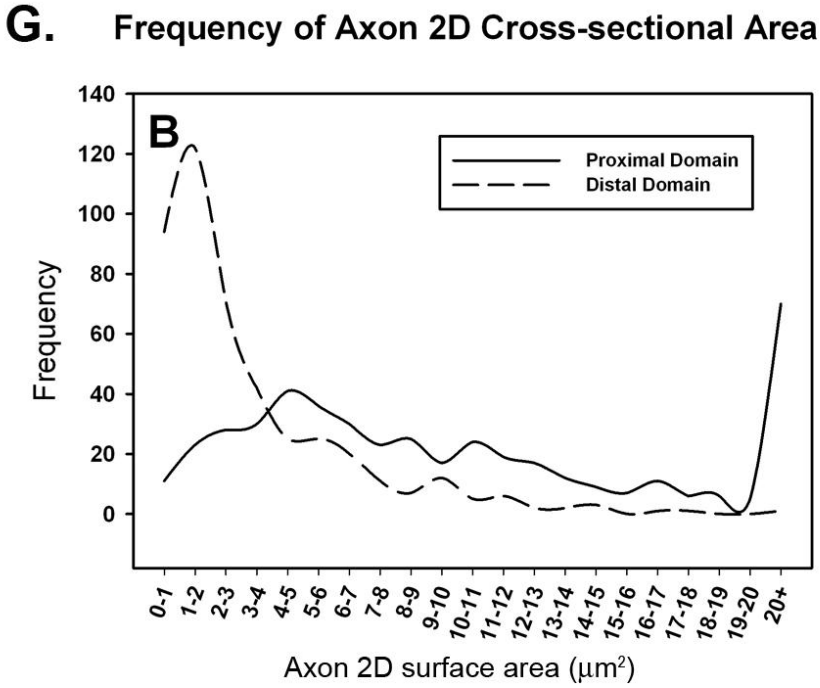

Figure 4.9: Nerve reconstruction – semi-thin sections.

Figure 4.9: Nerve reconstruction – semi-thin sections. (A and B) Control sciatic nerve samples. Sections are densely populated by myelinated nerves. Scattered blood vessels are present ((a), arrow). The epineurium is well defined ((B), arrow). (C and D) Samples taken within 1 mm of the proximal nerve stump. Myelinated and non-myelinated axons of varying caliber are present ((C), arrows). (*) in (C) denotes a blood vessel, arrow in (D) denotes external capsule of implant. (E) Sample taken within 5 mm of the proximal nerve stump. This domain was characterized by bundles of axons surrounded by a delimiting band of tissue that resembles the perineurium of native nerve ((E), arrow). (F) Samples taken 8–10 mm distal to the proximal nerve stump. Axon caliber and density is reduced with respect to the proximal domains depicted in (C)–(E). Arrowhead denotes the perineurial-like structure (precursors to the structures present in (E)). Note the nearly uniform alignment of the axons in all of the cross-sections. All images captured with a 100× oil immersion lens. Bar in (F) for (A)–(F) = 10 μm. (G) Frequency of the regenerating axon 2D cross-sectional area at proximal and distal sites of the implanted scaffold. The frequency at which the smaller caliber axons are encountered in the distal domains is greater than the proximal aspects of the tissue, typical of the early stages of nerve regeneration.

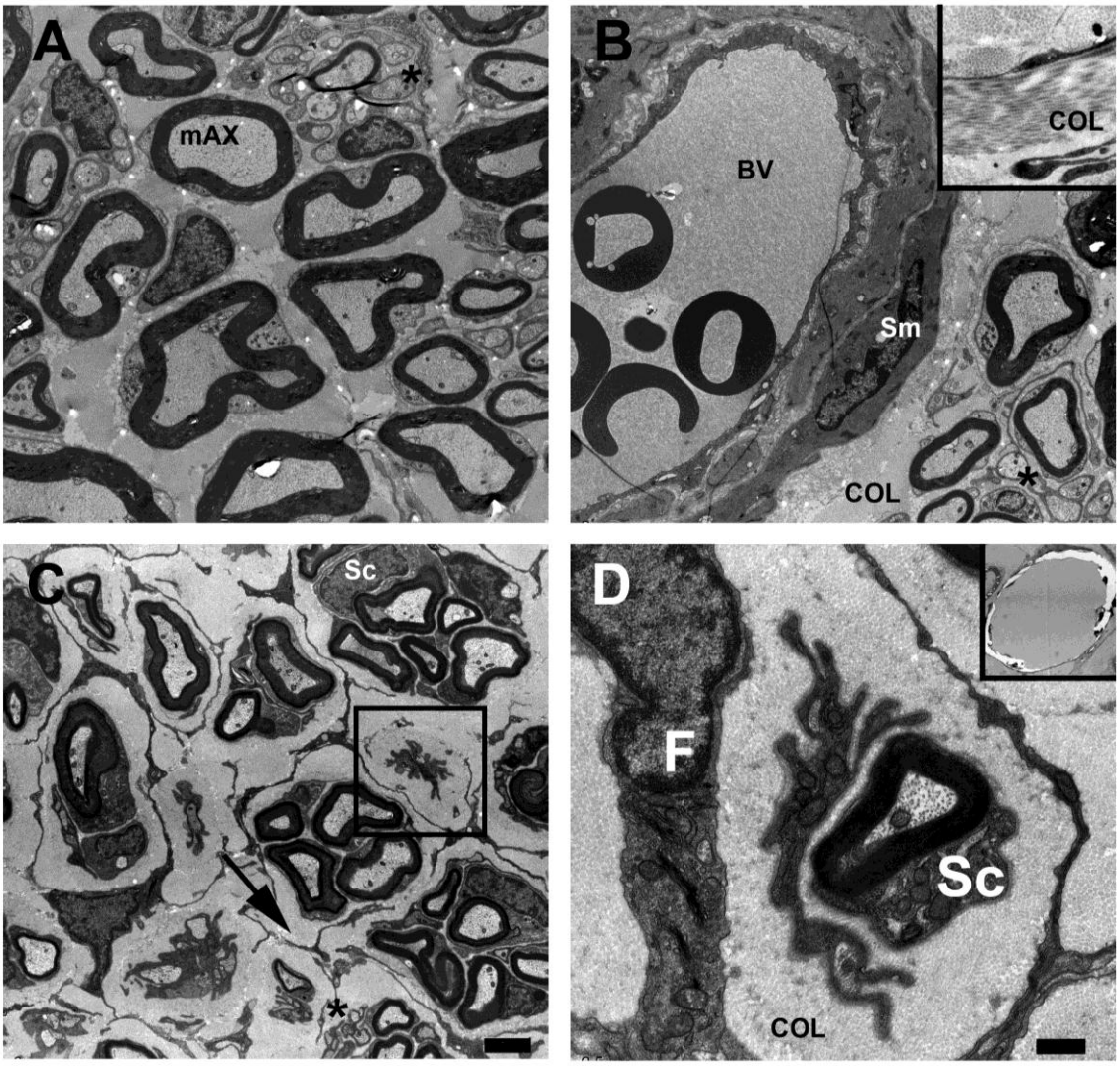

Figure 4.10: Transmission electron microscopy. (A and B) Proximal domains, (C and D) distal domains of regenerating tissue. In these cross-sections, the proximal and distal domains exhibit well differentiated myelinated axons (mAX) interspersed with unmyelinated axons (*). Functional blood vessels in the regenerating tissue range from capillaries to small arterioles ((B), BV) with smooth muscle cells ((B), Sm). Distal domains (C and D) contain the profiles of numerous Schwann cells (Sc) in association with small caliber axons. The box in (C) denotes one of these profiles, in (D) a high magnification detail of a Schwann cell surrounding a small caliber axon and adjacent to a fibroblast (F) is illustrated. Note the relatively high degree of maturation in the myelin sheaths. Cytoskeletal elements are clearly evident in the axons. Interstitial spaces are filled with parallel arrays of collagen fibrils ((B), inset shows a tangential section of collagen fibers, also see Col in (B and D)). Inset (D) illustrates a PCL fiber, note the lack of myelination on these structures. Scale bar in (C) for (A-C) = 2 µm, scale bar in (D) = 0.5 µm.

Overall, we note that the extent of myelination present on individual axons is surprisingly mature within the regenerating tissue. The myelin sheath surrounding the axons was considerably thicker than we anticipated, given the relatively short period of time that we allowed for regeneration (Fig. 4.10). Also surprisingly, the regenerating tissue was packed with highly aligned fibrils of collagen that were predominately oriented in parallel with the long axis of the developing tissue (Fig. 4.10B, inset). At this time the role of these fibers in directing axon growth remains an open question. Conversely, these fibers do not appear to have adversely affected the regeneration process; guides composed of collagen have exhibited efficacy in nerve reconstruction [57].

Using quantitative morphometrics we calculated that the proximal section of the grafts contained 8400 myelinated axons, a figure that is comparable to the estimates given in the intact sciatic nerve [58]. At the distal end, and again based on our light microscopy survey, we calculated that there were about 1900 myelinated axons present in the regenerating tissue. Consistent with the early stages of regeneration that we have examined in this study, we observed that the average 2D myelinated axon cross-sectional area decreases as a function of increasing distance from the proximal nerve stump, and that majority of axons present in the distal domains were, on average, smaller in caliber and more uniform in size distribution as compared to the proximal domain (Fig. 4.9G).

DISCUSSION

In this study we have used two pole electrospinning to fabricate "semi-solid", 3D-cylindrical constructs composed of fibers that have been deposited into highly aligned arrays that are oriented parallel to the long axis of the constructs. In contrast to conventional electrospinning systems, the extent of fiber alignment in air gap spinning is clearly much less dependent upon the size of the fibers. In our air gap system, we have been able to electrospin scaffolds composed of aligned PCL fibers ranging from less than 200 nm to ~1.5–1.8 μm in average cross-sectional diameter. The uncoupling of fiber alignment from its normal dependence on fiber diameter has allowed us to develop and test a family of scaffolds with distinct material properties and intrafiber spacing (void volume) to select the best configuration for a nerve conduit.

Several studies already have demonstrated that 2D sheets composed of anisotropic electrospun fibers can effectively induce the alignment of neuronal cells [42-44] as well as the directed and accelerated migration of a variety of cell types [45, 59, 60]. This type of 2D surface is particularly well suited for *in vitro* applications; cells plated onto a flat sheet are readily accessible for analysis by a variety of microscopy techniques [5]. These 2D constructs are less well suited for use in the actual reconstruction of a damaged nerve.

Sheets of electrospun materials have been described as 3D in the literature; however, arguably, the 3D aspect of this depiction may be overstated and is largely confined to a description of the surface topography of the scaffold. Air gap electrospinning makes it possible to produce a truly 3D cylindrical construct composed of linear arrays of fibers oriented along a common axis. We have produced cylindrical scaffolds 15–20 mm in cross-sectional diameter

using this system and we have observed virtually no degradation in fiber alignment in the large scale constructs.

As noted, the fabrication of nerve guides using conventional electrospinning processes has been explored to some degree. Electrospun PCL-based devices have been fabricated as hollow, cylindrical tubes that are designed to confine regenerating nerves to the lumen of the device while restricting the penetration of inflammatory cells into the injury site [50]. These hollow devices appeared to initiate only a nominal inflammatory response when used in sciatic nerve reconstruction. Additionally, PCL breaks down slowly, and as a result, has displayed good biocompatibility in a variety of other bioengineering applications. Our experiments yielded similar results and we did not observe evidence of inflammatory cells or scarring within our guides. Morphometric analysis would suggest that hollow nerve guides produced by conventional electrospinning processes using PCL can direct perhaps 25% of the axons (based on volume of tissue, not the actual number of axons) present in the proximal stump to regenerate down the length of 10 mm tube over a 14 week interval [50]. While the metrics between this study and our study vary to some degree, our estimates suggest that we achieved a similar degree of axon regeneration (approximately 25% of the axons present in the proximal section reached the distal end of the guides as determined by morphometric analysis) in our 3D guides over a 7 week interval (we believe the regeneration process has not reached its penultimate extent by any means in our experiments, given the very brief time interval of these preliminary experiments.

The extent of functional recovery that can be achieved after nerve injury is limited by the nature of the precipitating injury and by processes that exist downstream to the actual wound bed. For example, in peripheral nerve injuries, functional recovery may essentially

be complete if the continuity of the endoneurium is spared during precipitating event (neuropraxia). In this type of injury the myelin sheath that is distal to the wound bed represents a "full-length" guidance conduit. The regenerating axons are confined to returning to the end organs associated with the surviving endoneurium. These observations suggest that guidance cues incorporated into a synthetic nerve guide can play a critical role in directing the regeneration process [41]. The extent, and fidelity, of nerve regeneration and subsequent functional recovery are greatly reduced once the endoneurium has been compromised (axonotmesis and neurotmesis).

While electrospun, hollow devices afford a measure of improvement over existing nerve guide designs that have been fabricated by more conventional processes (excellent porosity for nutrient exchange and good structural integrity), we would argue that hollow electrospun tubes represent a relatively early evolutionary stage in nerve guide design. The autologous nerve guide remains the gold standard treatment for nerve injuries that require reconstruction. We have modeled our unique 3D design on the architecture of these "natural guides". The use of autologous implants is not without its limitations. For example, the action of harvesting the autologous tissue obviously results in morbidity at the donor site. The axonal debris that is present within the harvested tissue also must largely degrade before regenerating axons can penetrate the tissue, a time delay that can exacerbate the onset of degenerative changes in the distal tissues (*e.g.* loss of motor end plates in muscle, muscle disuse atrophy). While regenerative processes in the peripheral nervous system can restore a considerable degree of function to end organ tissues, the recovery of fine motor skills, unfortunately, is limited. We believe that functional recovery can be improved by (a) accelerating axon growth across the injury bed and simultaneously (b) confining these regenerating axons to a spatial domain (tissue

plane) that mimics their original position within the nerve. Our synthetic guides are designed to provide the guidance cues that are inherently present in autologous grafts without the time delay needed to degrade the axonal fragments present in the harvested tissues. In addition, we believe that our 3D guides can be used to confine regenerating axons to the tissue plane where they existed prior to the precipitating event that damaged the nerve. This can be expected to increase the probability that the axons passing down the guide structure will emerge closer to their original position, a circumstance that should improve targeting and thereby increase functional recovery.

In summary, air gap electrospinning makes it possible to directly incorporate guidance cues into the structure of a truly 3D construct. The pore spaces present between the aligned fibers in these nerve guides readily supported axonal growth. Somewhat surprisingly, even scaffolds composed of the smallest diameter fibers supported the penetration of axons and Schwann cells in our *in vitro* studies. It remains to be determined how the architecture of a 3D guide might be exploited to further modulate axonal targeting, sprouting and fasciculation. At present we are attempting to quantitatively determine how the number and density of electrospun fibers might impact these processes. We can only speculate how the incorporation of cells or gradients containing specific binding moieties and/or biochemical signals designed to enhance tissue regeneration might be used to further enhance the functional properties of our construct. Physical and biochemical cues that accelerate axonal regeneration can be expected to improve functional recovery in distal tissues by limiting end-organ complications associated with de-innervation (i.e. atrophy). Notably, the use of such combinatorial strategies may hold great promise in the development of treatment strategies and tissue engineering scaffolds that are designed to promote regeneration in the central nervous system [60, 61].

CONCLUSION

In peripheral nerve injuries, the extent of recovery depends upon the appropriate targeting and the time taken by the regenerating axons to reach and re-innervate the target tissues. In contrast to conventional hollow nerve conduits, our novel 3D nerve guide with dense arrays of anisotropic fibers are very effective at directing axon elongation along a defined axis, thereby providing the spatial cues for proper targeting. The use of our 3D nerve guide in place of an autologous graft eliminates the complications associated with donor site morbidity and theoretically accelerates the regeneration process by eliminating the need to degrade the axonal fragments that typify material sourced from autologous tissues. These factors can be expected to accelerate regeneration across the injury site, and thereby reduce the associated complications, and thus improve functional recovery.

Acknowledgments

Scanning electron microscopy and transmission electron microscopy were conducted at the VCU, Department of Neurobiology and Anatomy Microscopy Facility, supported with funding from NIH-NCRR shared instrumentation Grant (1S10RR022495) and, in part, NIH-NINDS Center core Grant (5P30NS047463). This work is supported, in part, by NIH R21 NS067364 (Colello).

CHAPTER 5

Chapter 5. Designing of a drug delivery platform for sustained release of gradients of growth factors at precise locations

Preface: *In this chapter we describe the preliminary investigation and proof of concept experimentation for the use of alginate as a solid phase platform designed to release growth factors and other therapeutic reagents over a prolonged period of time to enhance the regenerative environment of an injured tissue.*

Tissue regeneration in the adult takes place under unique conditions. For example, in the adult, when fully differentiated tissues are damaged they undergo a wound healing process that superficially approximates developmental events. However, it is critical to remember that this wounded tissue in the adult regenerates in an adult biochemical (and signaling) environment that is likely to have mechanical damage and will more than likely have an ongoing inflammatory response. Compounding these circumstances, wound healing in general, becomes far less efficient with age and with a deteriorated physiological state. Injuries may compromise a single tissue, like peripheral nerve, and leave associated tissues relatively unharmed. Fetal tissues undergo de novo differentiation, development and growth and do so in concert with other tissues. This makes for a very different environment than that of an adult. Wound healing in the skin is a very well documented example of how healing in the adult and fetal environment differ. For example, in adult dermal injuries, skin can undergo a certain degree of true regeneration but the process almost always is impaired to some extent by the development of scar tissue [62]. *This scar tissue is non-functional and limits the extent to which the wound healing process can restore normal structure and function in the skin. In contrast, wound healing in a surgically induced injury in the fetus can undergo complete and scar-less healing. This has been largely*

attributed to the signaling environment that exists during these early stages of development. TGFβ3-based signaling predominates in the fetus; in contrast TGFβ1 and TGFβ2 based predominate in adult tissues. When wound healing in the fetus is experimentally manipulated to take place with lower ratios of TGFβ3 versus TGFβ1 and TGFβ2, scarring can be induced even in the privileged environment of the fetus. Conversely, blocking TGFβ1and TGFβ2 in the adult and driving the healing with TGFβ3 reduces scarring in a skin injury [63]. These results underscore the role that local environmental events can play on the wound healing process.

Our novel 3D nerve guide fostered tissue regeneration in an experimental model of rodent sciatic nerve injury. These injuries are relatively short in length and there are concerns that longer defect injuries may not undergo as complete healing as described in our pilot study. To modulate the regenerative environment of the tissue injuries, we have developed a drug delivery platform designed to provide the sustained release of growth factors in precise locations and / or the establishment of growth factor gradients. This platform was then used in our 3D nerve guides to modulate the regenerative environment in a rodent model of long defect nerve injury to the sciatic nerve. These experiments are discussed in Chapter 6.

ABSTRACT

This study investigates the use of alginate as a platform for the controlled release of growth factors into a regenerative environment. Alginates are well characterized biopolymers used extensively in this type of application. One specific advantage to alginate gels concerns the observation that they can be fabricated into a variety of physical shapes and forms using very simple conditions. We used electrospray to produce microbeads (5-10 μm in diameter in a hydrated state), controlled volume droplets to produce macrobeads (2-3 mm in diameter in a hydrated state) and small segments of PVC tubing to produce linear threads (4-5 mm in diameter in a hydrated state) of alginate. The thread form of alginate was found to have the best capture efficiency of NGF. NGF release from the alginate threads was persistent and well sustained over a prolonged period of time. When alginate threads were incorporated into an electrospun 3D nerve guide, NGF was released and became concentrated in the vicinity of the thread. Imagining studies indicate that a fraction of the growth factor becomes adherent to the surrounding electrospun fibers. The fabrication methods to produce alginate threads are simple and can be used to deliver gradients of the same and or multiple growth factors at specific locations in an electrospun nerve guide.

INTRODUCTION

In long defect peripheral nerve injuries (in humans this represents a loss of approximately 3 cm of tissue), where a segment of nerve tissue is completely crushed or severed, a nerve guide is needed to restore the continuity of the damaged nerve. Functionally, these devices are designed to physically link the severed ends of a transected nerve and constrain the regenerating axons to grow in a directed fashion from the proximal stump of the nerve back into the perineural remnants of the distal nerve stump. These devices have a long history and are designed to direct the natural processes that lead to peripheral nerve regeneration [36, 37]. We have developed a nerve guide with unique 3D architectural features that is composed of aligned arrays of nano-to-micron scale diameter fibers. These constructs are produced by two pole air gap electrospinning [2] and are composed of the bio-compatible polymer, polycaprolactone (PCL). The guides are cylindrical in nature and contain literally thousands of individual channels that are orientated in parallel with long axis of the guide. The air gap process makes it possible to tailor the size (diameter) of these constructs to match the diameter of the nerve to be reconstructed

In a pilot study, we demonstrated that our electrospun 3D nerve guides support nerve regeneration across a 10 mm gap in the rodent sciatic nerve [2]. This injury gap represents a defect that is just below the threshold (threshold is > 10 mm) of what is considered to be a long defect nerve injury in the rodent. To address longer defect injuries, we suspect that it may be necessary to provide additional exogenous trophic factors to the regenerative environment to drive axon growth.

In this chapter, we examine the use of the carbohydrate polymer, alginate, as a platform designed to introduce NGF to precise locations and or in the form of gradients in the local microenvironment. NGF and other neurotrophic factors have short half-lives [64] and regeneration across a long defect nerve gap can take days to weeks depending on the nature of the injury, making it critically important to develop strategies designed to provide therapeutic agents over more prolonged intervals.

Alginate exhibits good biocompatibility and has been used as a delivery platform in a variety of different applications in the past [65-69]. Alginic acid (also called algin or alginates) are naturally occurring polysaccharide polymers isolated from brown seaweed (Phaeophyceae). They contain blocks of D-mannuronic acid and L-guluronic acid (Figure 5.1). Commercially available alginate is in the form of sodium alginate salt. These salts form a gel when a solution of the sodium alginate is extruded into a divalent cross-linking solution containing Ca^{2+}, Ba^{2+}, or Sr^{2+}. The process of gelation occurs when sodium ions associated with the guluronic acids exchange with the divalent cations, this exchange causes the sugar moieties to stack and form a characteristic egg-box-like structure (Figure 5.1 and 5.2) [66, 70]. Each polymer chain of alginate can dimerize and form junctions with many other chains and results in the formation of a cross-linked alginate gel. This gelation process can be used to trap growth factors and other therapeutic reagents into the resulting alginate gel [66, 67, 71]. After the gelation process alginate is typically collected and cured and or / dried by any number of different methods. Once the dry alginate is placed back into an aqueous environment it undergoes hydration and gradually dissolves as the diavant cations begin to dissociate from the sugars, releasing reagents that are trapped in the carbohydrate based matrix. In this study, we exploit the characteristics of alginate and explore

the use of this material as a delivery system designed to incorporate growth factors in precise locations and / or to produce gradients of growth factors within a nerve guide.

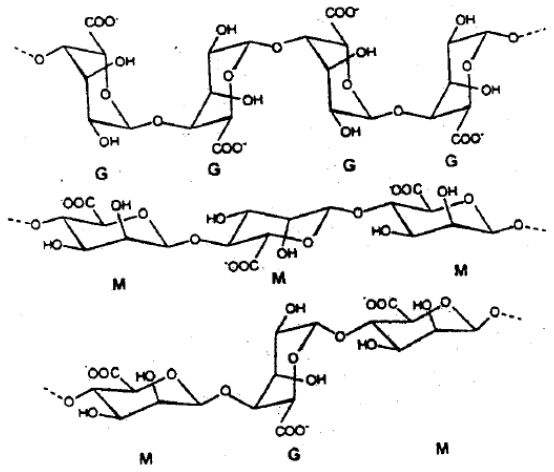

Figure 5.1: Structure of alginic acid residues. Alginic acid is a linear polymer with homopolymeric blocks of M = mannuronic acid and, G = guluronic acid residues covalently linked together *(From Tonnesen and Karlsen, 2002* [66].

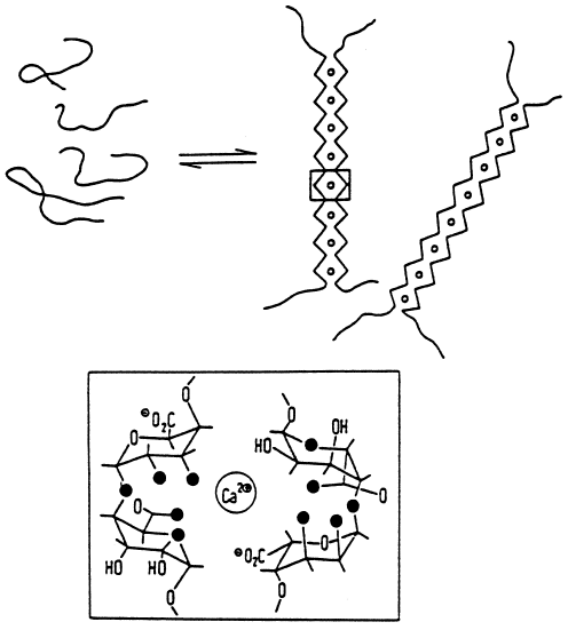

Figure 5.2: Schematic of the characteristic egg-box structure. The poly-L-guluronate sequences are cross-linked by the calcium ions resulting in alginate gelation process. Upper part of the figure represents random coils of the mannuronic acid and guluronic acid residues converting to ribbon-like structures containing arrays of calcium ions. The lower part of the figure represents the proposed binding between the calcium ions and the guluronic acid residues. *(From Gombotz and Wee, 1998* [70]*).*

In an effort to enhance peripheral nerve regeneration by providing biochemical cues to the regenerating axons, we used Nerve Growth Factor (NGF) as a model protein. One specific advantage of this particular growth factor is that its functionality can be easily evaluated in tissue culture experiments. The growth and survival of explanted dorsal root ganglions (DRGs) is depended upon this reagent *in vitro* [2, 72, 73]. In this study we tested various permutations of alginate and gel structures to develop a delivery platform designed to provide the sustained release of NGF at precise locations in between the electrospun fibrils of the 3D nerve guide.

Each form that we examined exhibited its own relative merits and limitations in this particular application. Many reagents, when added directly to the organic solvents used in electrospinning can be damaged [74]; to address this processing limitation, we developed alginate microbeads as a means to trap and sequester therapeutic reagents in a compartment that can be directly added to the organic solvents used in the electrospinning process and co-spun into the fibers of an electrospun scaffold. Unfortunately, the capture efficiency of trapping reagents into these beads is very low. We next designed threads of alginate as a means to develop gradients of therapeutic reagents. ELISA results show that this platform demonstrated much better capture efficiency and favorable release kinetics. When implanted into a scaffold there threads release NGF, which then adheres to the surrounding fibers of the electrospun matrix, producing a functional gradient.

METHODS

Alginate Microbeads Preparation.

Unless otherwise noted, all alginate solutions were prepared by dissolving the sodium salt of alginic acid from brown algae (Sigma-Aldrich) in deionized water at 12.5 mg mL^{-1}. All solutions in controlled release studies were supplemented with Bovine Serum Albumin (BSA) at a concentration of 10 mg mL^{-1} (Alginate–BSA solution). Nerve Growth Factor (NGF) was added in various concentrations to the alginate solution, Alginate–BSA–NGF solution was loaded into a 10 mL syringe which was capped with an 18 gauge blunt-tipped needle. The syringe was attached to a vertically oriented syringe driver set at a delivery rate of 2 mL hr^{-1} (Figure 5.3). A 250 mL Pyrex beaker containing 100 mL of 2% calcium chloride solution prepared in deionized water was placed underneath the vertical syringe such that the distance between the needle tip and the base of the beaker was approximately 6.5 cm. The alginate solution was charged to +22 kV with a positive electrode connected to the needle; a metallic plate charged to -22 kV was placed beneath the glass beaker containing the calcium bath. The potential difference between the alginate solution and the metallic plate under the beaker results in the ejection of a fine aerosol mist of the Alginate–BSA–NGF from the needle tip. The resultant alginate aerosol is deposited into the calcium bath, causing alginate solution to undergo polymerization / gelation and formation of alginate microbeads (5-10 μm in diameter). Beads were incubated for 10 min in the calcium bath; the calcium bath was then transferred into 50 mL centrifuge tubes and subjected to gentle centrifugation (400× g) for 10 minutes. Beads were collected, rinsed in fresh calcium bath solution supplemented with 10% propanol and re-suspended in this same buffer. The calcium propanol solution was then supplemented, by volume, with 25% HFP (Sigma-

Aldrich). This results in the formation of a bi-layer solution with the beads collecting at the interface. Beads were recovered and dried under a vacuum.

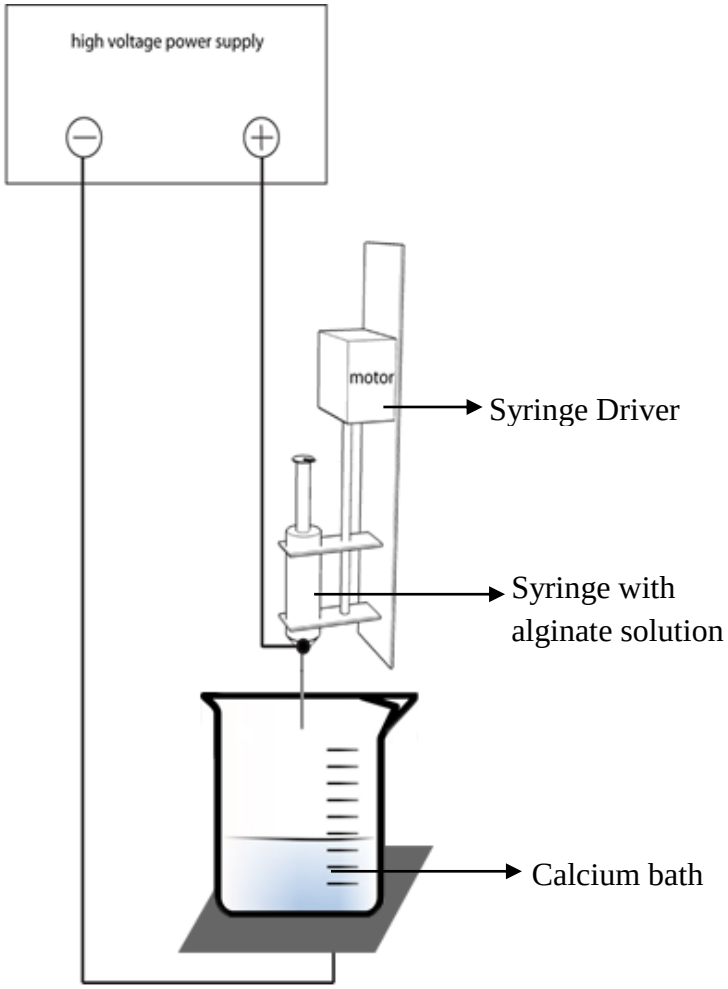

Figure 5.3: Schematic of the electrospraying apparatus for preparing alginate microbeads. The alginate-BSA solution with / without the NGF was loaded into the syringe with its needle connected to the positive electrode of a high voltage power supply. The negative electrode was connected to a metallic plate placed under a 250 mL beaker containing 100 mL of 2% calcium chloride. The rate of delivery for the syringe driver was set at 2 mL hr^{-1}. The potential difference of the charges resulted in electrospraying of the alginate beads from the needle tip; the spray is directed inside the beaker and into the calcium bath where the droplets of alginate are induced to undergo gelation.

Alginate Macrobeads Preparation.

Macrobeads were used for comparison and as controls in selected experiments. Alginate–BSA–NGF solution was applied in 25 µL aliquots using piston-driven air displacement pipettes into a 250 mL beaker containing 100 mL of 2% calcium chloride solution prepared in deionized water. Macrobeads were incubated for 10 minutes in the calcium bath and processed through the propanol and HFP washes as described for the microbeads.

Alginate Threads Preparation.

To produce linear threads of alginate we pipetted Alginate–BSA–NGF solutions into segments of PVC tubing with an inner diameter of 2 mm. To produce "micro" gradients of NGF along the length of these threads, alginate solutions were supplemented with varying amounts of NGF. An aliquot was injected into the tubing and then frozen at -70 ºC for 15 minutes. Once frozen, additional aliquots of NGF supplemented alginate prepared with varying concentrations of growth factor were sequentially added to the already frozen material. This process is easy and can be done quickly enough such that only the interface of the frozen material undergoes any melting when the next solution is added to the "casting tube". This slight amount of melting "connects" the aliquots together (see (Figure 5.4). Once an additional aliquot has been added to the tube it is returned to the freezer once again. By repeating this process a thread can be produced. Once the thread has been fabricated a thin plunger is used to extrude the frozen alginate into a 250 mL beaker containing 100 mL of 2% calcium chloride solution prepared in deionized water. The threads were incubated for 10 minutes in this solution then recovered washed and dried as described.

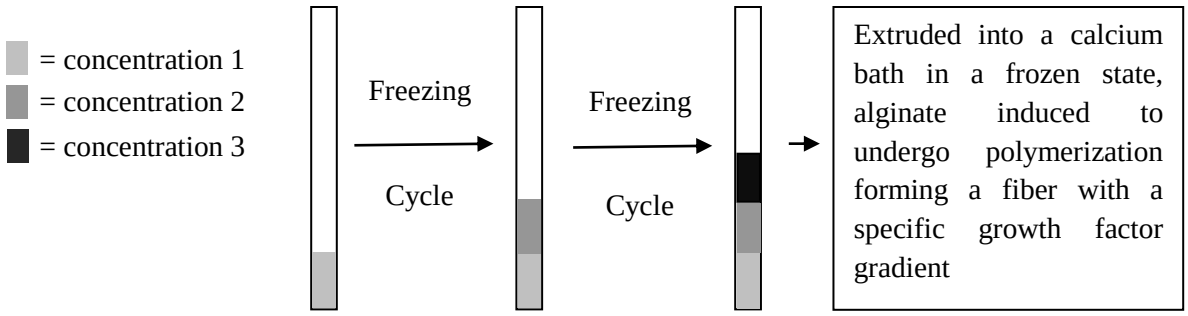

Figure 5.4: Fabrication of alginate thread with concentration gradients. A desired amount of alginate solution with one concentration of a reagent is pipetted into a segment of PVC tubing and this sample is frozen. Then a second aliquot of alginate solution containing a second concentration of reagent is pipetted into the same PVC tube directly on top of the first aliquot of the now frozen alginate solution. The vessel is then frozen again. This cycle is repeated until a frozen thread of alginate containing a reagent gradient is completed. Finally, the complete column inside the tubing is extruded into a calcium bath for polymerization. The minor amount of melting that occurs as each subsequent aliquot of alginate solution is added to the frozen material is enough to ensure that the thread remains intact as a continuous linear structure when the column is extruded as we well as when it undergoes polymerization.

Routine Scanning Electron Microscopy (SEM).

Dried alginate microbeads, macrobeads, and threads without any further processing were mounted onto a scanning electron microscope stud and sputter-coated with gold for 2 minutes. A Zeiss EVO XVP scanning electron microscope equipped with digital acquisition was used for image capture.

Enzyme Linked Immunoprecipitation Assays.

For NGF release assays, alginate structures were incubated in serum-free Minimum essential media (MEM) (GIBCO), media was collected and changed out daily. Samples were stored at -70 ºC until needed. On the last day of experimentation, the remaining fragments of alginate were processed in dissolving buffer (10 mM 3-(N-Morpholino), Propane-Sulfonic acid (MOPS), 100 mM sodium citrate, and 27 mM sodium chloride; all Fisher Scientific) for 30 min at 37 ºC [65]. This procedure was done to measure the amount of NGF left in the alginate on the last day of the release assays. For NGF capture assays, the efficiency of NGF capture in the different forms of alginate was determined by directly incubating the alginate constructs in dissolving buffer for 30 min at 37 ºC. After collection of the samples, NGF ELISA was conducted on NGF E_{msx} ImmunoAssay System (Promega) following the manufacturer's detailed protocols.

Statistical Analysis.

To compare the growth factor capture and release profiles in the different forms of alginate, One-Way ANOVA was used to screen the data sets, and Holm-Sidak method was used for multiple pairwise comparison in the *post hoc* analysis (p values as reported).

Imaging of NGF.

NGF was labeled with NHS-Rhodamine (EZ-label Rhodamine Protein Labeling Kit, Pierce Biotechnology) using the manufacturer's protocol. Three aliquots of alginate (10 µL each) were supplemented with the Rhodamine-labeled NGF at concentrations of 200, 400, and 1000 ng NGF mL^{-1} respectively and used to prepare a gradient thread. The thread was hydrated and imaged by fluorescence microscopy then dried, embedded in Tissue-Tek (Sakura, Inc) and frozen. Threads were cut in 20 µm thick sections in parallel with the longitudinal axis of the constructs using Shandon cryostat.

In limited experimentation alginate threads were supplemented with 25 ng of Rhodamine-labeled NGF. Alginate threads (+ or – NGF), were placed near the two ends of a 3D nerve guide and within the fiber arrays. This was accomplished by spinning a small amount of PCL onto a target array in a two pole air gap electrospinning system. Once the PCL had collected across the target array the threads were placed onto the fibers. The electrospinning process was re-started and completed. This results in a 3D nerve guide with an alginate thread enveloped and completely trapped within the fiber arrays. The electrospun scaffolds, with the two spatially separate alginate threads were incubated in serum-free MEM (GIBCO) for 4 days with media being changed daily. On day 5, the scaffold was recovered and embedded in Tissue-Tek, frozen and cut into 60 µm thick longitudinal sections using the Shandon cryostat. All samples using the rhodamine-labeled NGF were imaged with a Nikon TE300 microscope equipped with a 10× objective and a DXM 1200 digital camera. Images were captured at a pixel resolution of 3840 × 3072. Individual images of the alginate threads and scaffolds were assembled into montage images using Adobe Photoshop software.

Cell Culture.

3D nerve guides with alginate threads were prepared for cell culture experiments. Alginate threads were prepared using 15 ng NGF/thread in the starting conditions. From our preliminary experiments we assume a capture efficiency of approximately 50% for the NGF used in these assays. Given this assumption, starting with 15 ng of NGF in the capture aspect of thread fabrication will result in the capture of 7.5 ng of NGF in each thread. Scaffolds were prepared using two pole air gap electrospinning using a starting concentration of 200 mg mL^{-1} PCL as described in reference 2 (and Chapter 4 of this thesis). Dry alginate threads were placed at one end of these scaffolds and within the fiber arrays. Scaffolds were incubated overnight in MEM (GIBCO) supplemented with 10% FBS, 2.0% antibiotics, and 0.3% glucose. Media was changed and a 25 gauge needle was used to prepare an opening into the dorsal surface of the scaffold. Dorsal root ganglion (DRG) explants were prepared as described previously [53, 54]. Intact ganglia were removed from the spinal cords of embryonic day 15 (E-15) rats, tissue was pooled. A single explanted and intact DRG was inserted into the cavity prepared in the electrospun scaffolds. DRG explants were maintained for 3 days, media exchanged every other day.

Immunofluorescence Microscopy: DRG Explants.

DRG explants were rinsed in PBS and fixed in 4% paraformaldehyde prepared in PBS. Samples were extracted in 0.1% Triton x-100 prepared in PBS and immunostained for the neuron specific marker TuJ1 (Tubulin J1: MMS-435P, Covance, 1:500). Antibodies were diluted in PBS supplemented with 1% BSA and applied to cultures overnight at 4 °C. Scaffolds were rinsed and counterstained with Goat anti-mouse antibodies conjugated with Texas Red

(1:200). A Nikon TE300 microscope equipped with a 10× objective and a DXM 1200 digital camera was used to capture images at a pixel resolution of 3840 × 3072. Individual images of the DRG explants were assembled into montages using the Adobe Photoshop software.

RESULTS

Alginate Microbeads vs. Macrobeads vs. Threads.

The microbeads, macrobeads and alginate-based threads showed varied morphology macroscopically (Figure 5.5). Dry microbeads exhibit a saucer-like appearance (Figure 5.5A); the macrobeads (Figure 5.5B) and threads (Figure 5.5C) both displayed complex surfaces with many convolutions.

To characterize the relative efficiency of NGF capture in the different alginate constructs, samples were prepared and then directly dissolved in the alginate dissolving buffer. The amount of growth factor present in each sample was then assayed (Figure 5.6). This capture efficiency is a critical variable to define for future *in vivo* experimentation. This information is necessary in order to insure that constructs are formulated with effective doses of material. ELISA assays indicated (N=3) that the capture efficiency of NGF in the alginate macrobeads was superior to that of microbeads ($p < 0.001$). Alginate threads were more efficient than microbeads ($p < 0.001$) and the macrobeads ($p = 0.003$) at trapping the NGF.

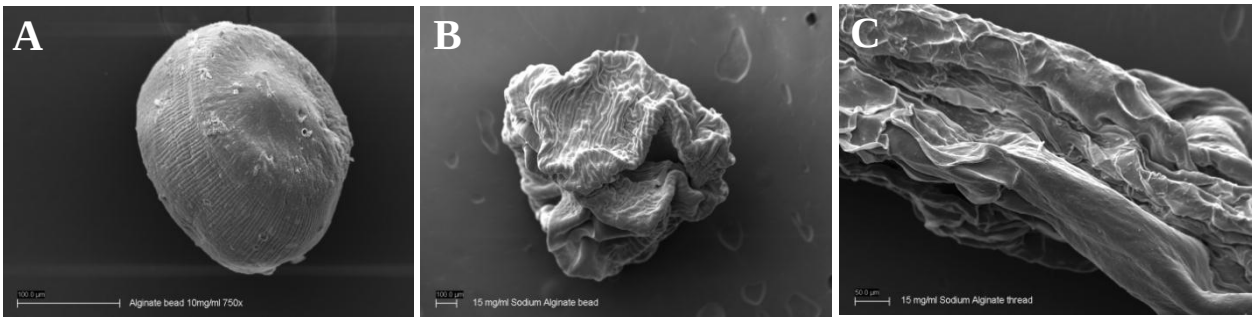

Figure 5.5: SEM images of (A) alginate microbeads, (B) macrobeads, (C) threads. Scale bar in (A,B) = 100 µm, Scale bar in (C) = 50 µm.

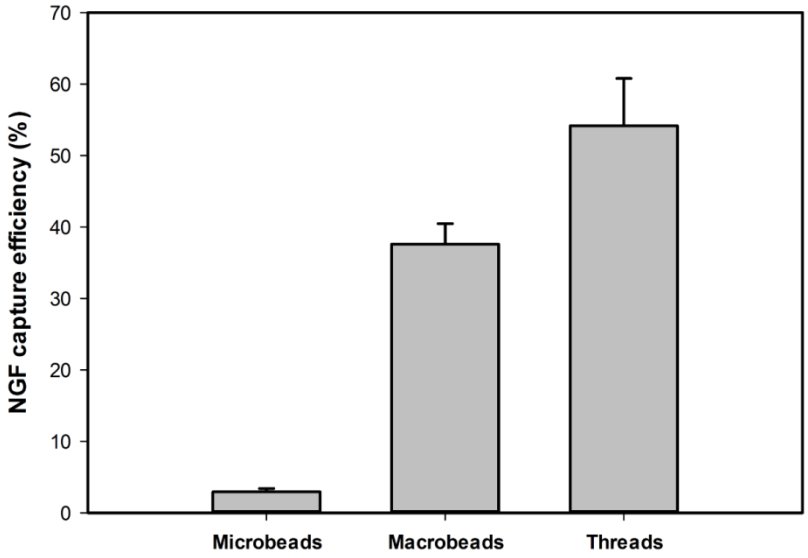

Figure 5.6: NGF capture efficiency of different forms of alginate delivery platforms. ELISA assays (N=3 separate experiments) indicated that NGF capture efficiency in alginate threads ($p = 0.003$) > macrobeads ($p < 0.001$) > microbeads.

Effect of Alginate Concentration on NGF Capture and Release.

Given the poor capture efficiencies of the microbeads and the poor dimensional characteristics of the macrobeads (too large to electrospin, too large to incorporate into a nerve guide directly), we concentrated our efforts on characterizing the threads prepared by extrusion. Our ELISA assays indicated that threads were highly efficient at capturing the NGF. We next examined how varying the concentration of alginate impacted the capture and release efficiency of this growth factor. Alginate threads were fabricated from alginate at starting concentrations of 2.5 mg mL^{-1}, 7.5 mg mL^{-1}, and 12.5 mg mL^{-1}, each was supplemented with 10 ng NGF. The alginate threads prepared using 12.5 mg mL^{-1} alginate acid were more efficient at capturing the NGF protein as compared to the alginate threads prepared using 2.5 mg mL^{-1} ($P = 0.022$) (Figure 5.7A). The capture efficiency of the alginate thread prepared using alginate at 7.5 mg mL^{-1} was not statistically different from the thread made from 12.5 mg mL^{-1} alginate acid. Thus, capture efficiency is modulated to some extent by the concentration of alginate used to prepare a construct; however we note that increased viscosity of the higher concentrations of alginate make the material more difficult to process.

In release studies the total cumulative amount of NGF that was released from alginate threads prepared from 2.5 mg mL^{-1}, 7.5 mg mL^{-1}, and 12.5 mg mL^{-1} alginate was not statistically different after 7 days (Figure 5.7A). However, an examination of the amount of NGF that is released on a daily basis reveals that release is slower from structures prepared from higher concentrations of alginate. Additionally, at the conclusion of the experimental interval, there was more NGF remaining in the constructs prepared with the higher concentrations of alginate. Thus, as alginate concentration is increased, capture efficiency is improved and the captured material is available for a longer period of time with a slower, more sustained release pattern.

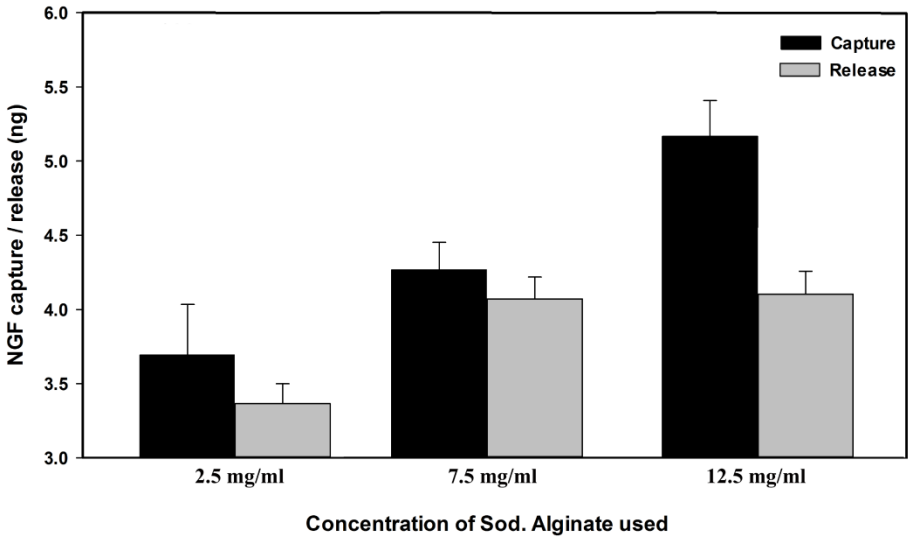

Figure 5.7A. NGF capture efficiency of alginate threads and total NGF release in 7 days from different concentration alginate threads (2.5 mg mL^{-1}, 7.5 mg mL^{-1}, and 12.5 mg mL^{-1}). Increased capture efficiency is noted in alginate threads prepared from 12.5 mg mL^{-1} concentration vs. 2.5 mg mL^{-1} concentration ($p = 0.022$). However, no statistical difference is noted in the NGF release from these threads over a 7 days period.

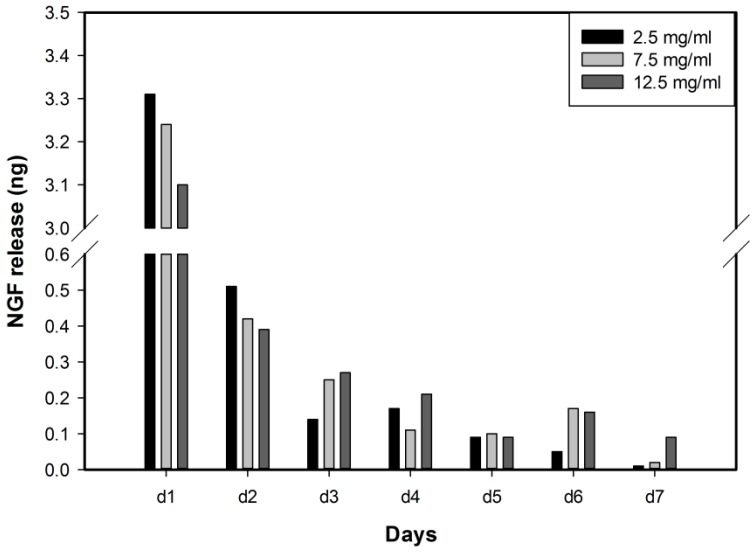

Figure 5.7B: NGF release profile from varying concentration alginate threads. Constructs were each prepared with 10 ng of NGF. Release from alginate threads prepared using 12.5 mg mL^{-1} alginate is comparatively slower as compared to the alginate threads prepared using lower concentrations of alginate.

Saturation Value of Alginate Thread for NGF Loading.

We were not able to ever come close to capturing 100% of the NGF added to our alginate solutions. One explanation for this result is that we might have already reached the saturation levels of capture for this particular growth factor in our experiments. To test this hypothesis, we next loaded varying amounts of NGF (5-100 ng) into a fixed volume of alginate solution (25 µL at 12.5 mg mL^{-1}) and prepared alginate threads. The constructs were then directly processed in dissolving buffer; the recovered material was assayed by ELISA for NGF content. The fractional amount of NGF that was captured in these experiments did not vary with the starting concentration of growth factor. For example, the capture efficiency for 5 ng of NGF was approximately 55%; the capture efficiency for 100 ng of NGF was nearly identical (Figure 5.8). These data indicate that the amount of NGF added to our alginate solutions during thread fabrication does not represent the rate limiting step in the capture efficiency. During thread fabrication the frozen alginate appears to thaw as it undergoes polymerization (these processes appear to take place nearly simultaneously) and we suspect that it is during this step that a fraction of NGF is lost before it can be trapped in the forming gel. Also, NGF may be present on the surface of the construct and this material simply diffuses away when the alginate is immersed in the calcium bath. Consistent with these conclusions, an examination of the soluble phase of our polymerization buffer (calcium bath) indicates that most of the lost NGF is present in this fraction (Figure 5.9).

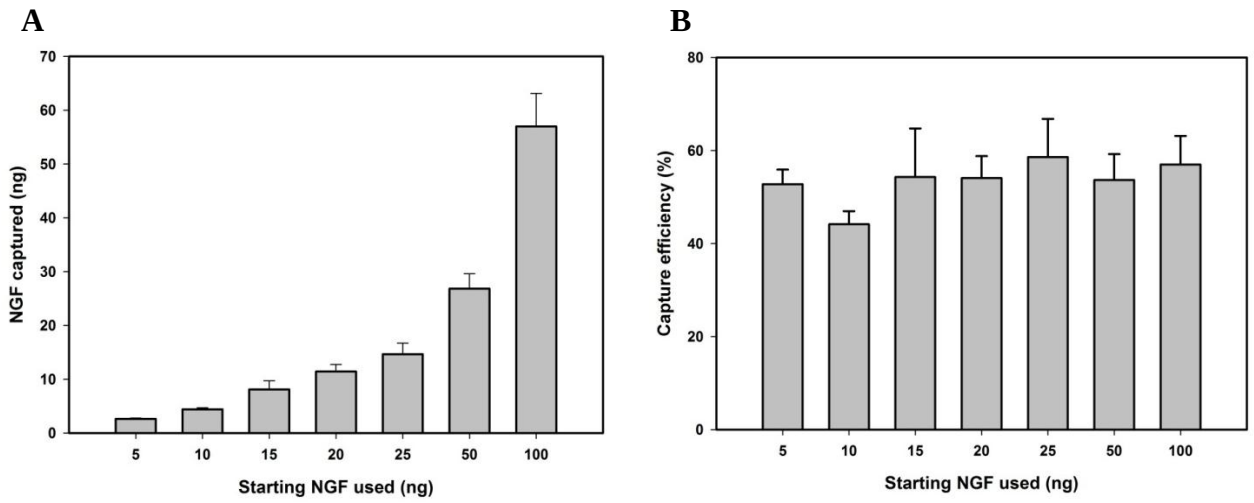

Figure 5.8 (A,B). NGF capture efficiency of alginate threads loaded with varying concentration of NGF. The threads were prepared from 25 µl alginate at a concentration of 12.5 mg mL^{-1} and loaded with 5, 10, 15, 20, 25, 50, and 100 ng of NGF. Capture efficiency was approximately 50-60% for all conditions assayed. All data plus / minus the standard deviation.

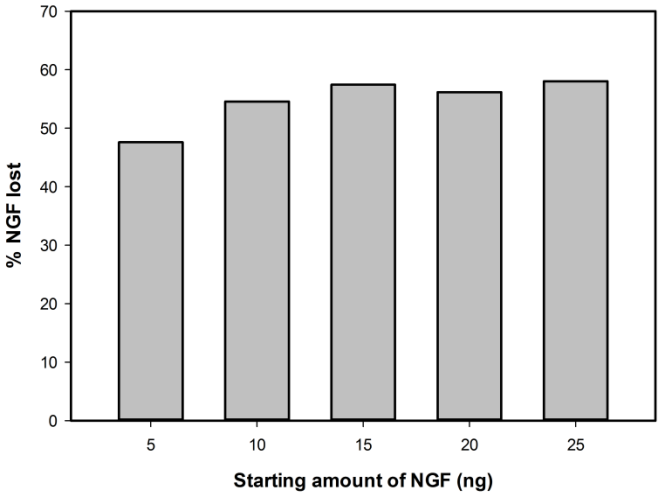

Figure 5.9: % NGF present and lost to the calcium chloride bath during the process of alginate thread polymerization. ELISA assays revealed that regardless of the amount of NGF added to the system that approximately 50% of the growth factor is lost during polymerization.

NGF Release Profile.

To determine how the starting concentration of NGF impacts the kinetics of growth factor release, we conducted additional controlled release studies. Alginate threads (alginate volume 25 μL at 12.5 mg mL^{-1}) were prepared and supplemented 5 ng, 15 ng, or 25 ng of NGF. In these experiments there was a burst of release from each of the samples on day 1. This was followed by a sustained release of NGF from all the samples from day 2 continuing until day 8 (Figure 5.10).

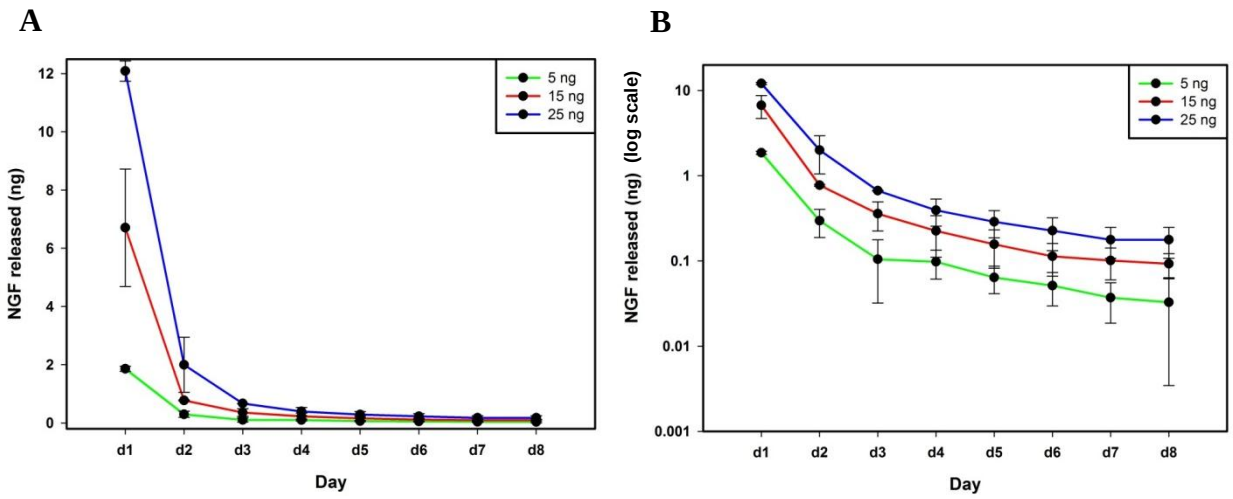

Figure 5.10: NGF release profile from alginate threads. (A) NGF release profile of the alginate threads prepared from 25 µl volume of 12.5 mg mL^{-1} alginic acid sodium salt. We tested 3 different concentrations of NGF were examined: threads were loaded with 5ng (green), 15 ng (red), or 25 ng (blue) of NGF. (B) NGF release profile with expanded scale on the Y-axis of the plot between 0.001 ng and 1.0 ng to reflect the variable release kinetics, from day 2 to day 8, of the 3 groups of alginate threads loaded with varying amounts of NGF. All data plus / minus the standard deviation.

Characterization of NGF within a 3D Electrospun Nerve Guide Scaffold.

We prepared 3D nerve guide scaffolds and incorporated alginate threads containing varying amounts of NGF into these constructs. In controlled release experiments, and with respect to threads in media (*i.e.* threads in media alone and not incorporated into scaffolds), only about 15-25% of the NGF (values varied with the starting amount of NGF) that was expected to be released appeared in the media at day 1 in samples that had been incorporated into scaffolds. By day 3, the released valued declined to 11-18% of that observed in the control threads (threads not incorporated into scaffolds). Given the large surface area present in the fibers of a 3D nerve graft, the logical conclusion to these experiments is that a substantial proportion of the NGF becomes trapped within the fiber arrays of the scaffolds and is not released into the surrounding media. This conclusion was supported by imaging experiments.

To characterize how the NGF interacted with the electrospun fibers, we loaded alginate threads with or without rhodamine-labeled NGF and incorporated these constructs into 3D electrospun scaffolds. After 4 days of incubation under conditions identical to those used in the controlled release experiments, the labeled NGF release was found to be concentrated in the vicinity of where the alginate threads were originally embedded (Figure 5.11B). The electrospun PCL fibers in these domains were coated with the labeled NGF. When control threads were imaged no signal could be detected.

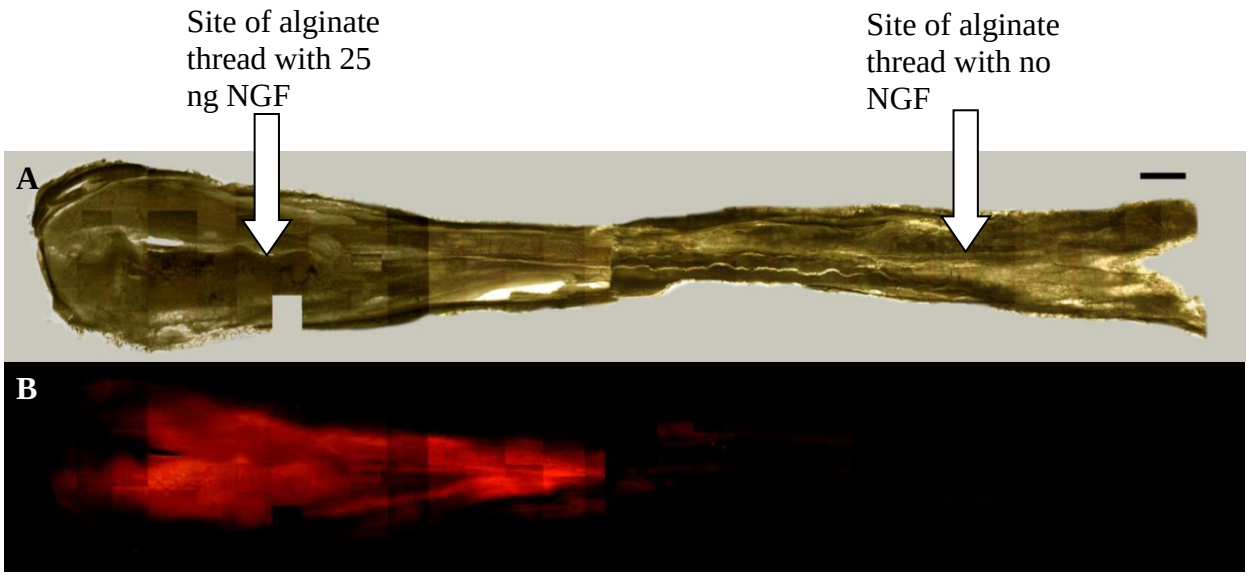

Figure 5.11: NGF release and capture from alginate thread inside electrospun 3D nerve guide. (A) Montage brightfield image of electrospun 3D scaffold. Alginate thread with 25 ng NGF was placed in between the fiber arrays (left side of image). A control alginate thread with no NGF was placed inside the scaffold on the right. (B) Immunofluorescence of rhodamine-labeled NGF demonstrating the local release and concentration of growth factor in a relatively localized domain.

Functional Assay

DRG cultures were used to confirm the bioactivity of the NGF released from alginate threads. DRG explants require NGF for survival and in order to extend neurites in tissue culture. DRGs were cultured for 3 days in scaffolds plus or minus alginate threads prepared with NGF. At the conclusion of the experimental interval DRGs cultured in 3D nerve guides supplemented with NGF produced elaborate arrays of neurites that grew in parallel with the surrounding fibers (Figure 5.12). These results indicate NGF was released in physiologically relevant levels within the nerve guides. No outgrowth was observed in the absence of NGF.

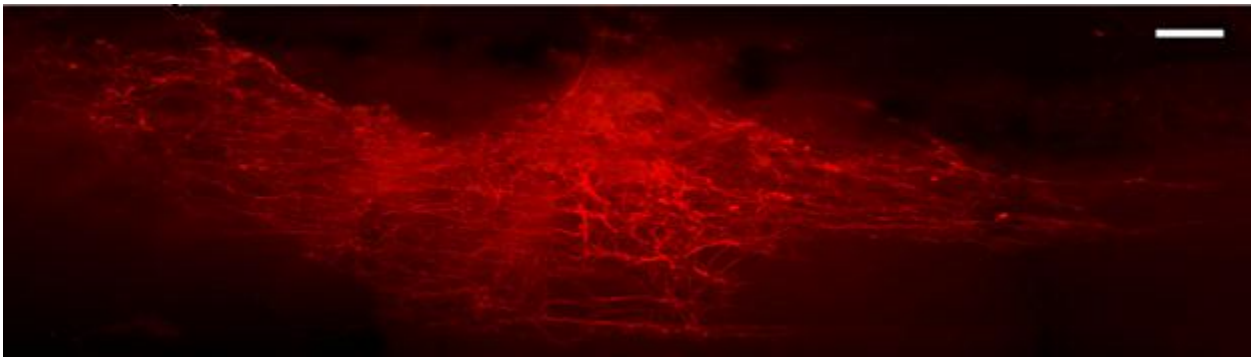

Figure 5.12: DRG culture in scaffold with NGF in alginate delivery platform. The elongating axons stained with TuJ1 anti-body growing inside the 3D nerve guide confirms the bioactivity and availability of the NGF released from the alginate threads inside the 3D nerve guide. Scale bar = 100 µm.

Alginate Thread with NGF Gradient.

Finally we investigated the extent to which we could fabricate a growth factor gradient over a very short interval. Gradients of growth factors have different effects on regenerative environments as compared to the effects of that same factor distributed in a homogenous fashion [75]. For example, a gradient of NGF elicits an enhanced response in regenerating axons as compared to uniformly distributed NGF [64]. Using the repeated freeze cycles as described above in the methods section, gradients of NGF (or other factors or blends of factors) can be incorporated into a single segment of an alginate thread for the sustained release of materials within a 3D nerve guide. In this series of experiments we used three concentrations of Rhodamine-labeled NGF (200, 400 and 1000 ng NGF mL^{-1} respectively) to prepare the gradient-thread by the process of sequential freezing. The results of these experiments are illustrated in Figure 5.13.

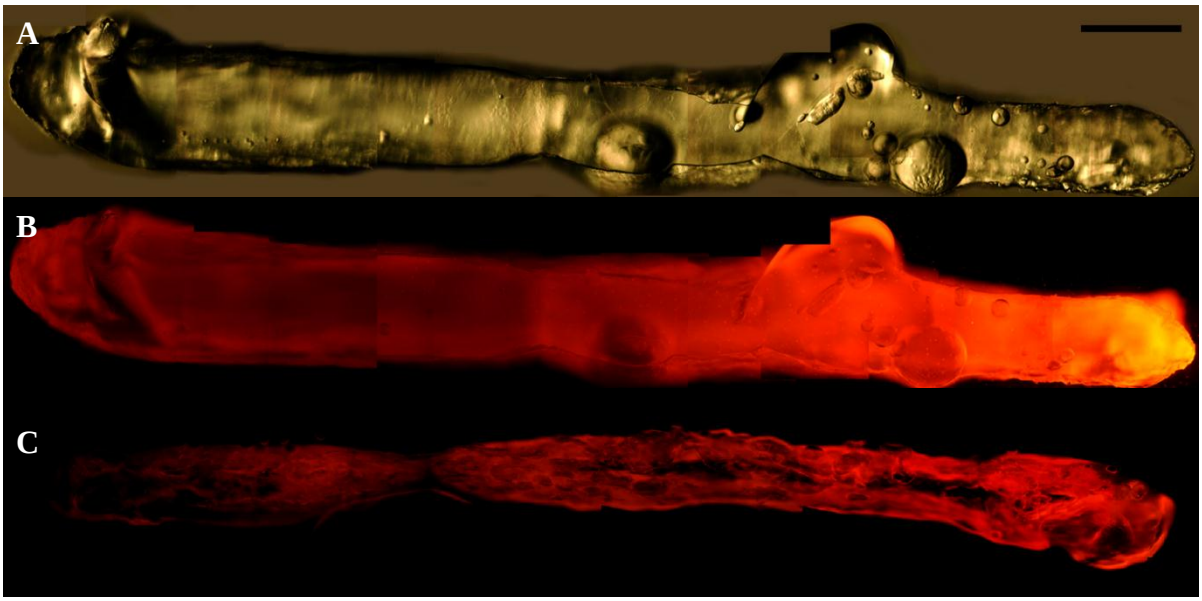

Figure 5.13: NGF gradient in the alginate thread. (A) Brightfield image of an alginate thread, focal plane at the surface of the construct; (B) fluorescence image of the same thread demonstrating the distribution of rhodamine-labeled NFG gradient. The gradient runs from lowest to highest from left to right in the depicted sample. (C) Frozen longitudinal section of the same thread confirming the gradient distribution of NGF within the thread. (A)-(C) captured with 10× objective and assembled into a montage image. Bar in (A) = 1 mm for (A - C).

DISCUSSION

The unique properties of the alginate make it possible to use this material as a platform to trap and deliver a variety of proteins and other therapeutic reagents. For example, for this material: (i) the gelation process occurs at room temperature, (ii) the gels are porous allowing for the outward diffusion of molecules not directly embedded in the gel, (iii) the gelation process is flexible and can be induced using a variety of methods (extrusion, drops, sprays, and so on), (iv) biodegradation of the alginate occurs under normal physiological conditions thereby releasing materials that have been incorporated into the gel structure, (v) and, it exhibits good biocompatibility.

We compared the efficacy of three different forms of polymerized alginate gels – microbeads, macrobeads, and threads. Capture and controlled release studies indicate that alginate threads have far better efficiency in capturing NGF as compared to the alginate micro- and macro-beads. Loss may occur in microbead formation in any number of different sites in the fabrication process. The NGF is mixed directly with the alginate and electrosprayed into a calcium bath. Overspray and poor targeting must account for some loss. Beads are also likely lost during recovery as they have a small volume. Directly fabricating macrobeads by simply dropping a constant volume of alginate into a calcium bath improves capture efficiency, but the physical dimensions of this form of alginate gel limits its use in our tissue engineering applications. Moreover, even with improved NGF capture efficiency, as compared to the microbeads, there still was a substantial loss of growth factor during the fabrication steps. As determined from our assays (*e.g.* Fig 5.9) most of this loss occurred during the alginate polymerization stage in the calcium bath.

Alginate threads exhibited the highest capture efficiency among all the alginate forms tested. This increased efficacy can largely be attributed to how the polymerization process was initiated; the frozen alginate structure was directly extruded into the polymerization buffer. Directly applying the frozen (and solid form of) alginate into the calcium bath for polymerization likely reduces the inherent loss of NGF from the construct that we observed when we processed the (wet) microbeads and macrobeads for gelation. Our experiments with the alginate macrobeads clearly indicate that a considerable amount of growth factor is lost to diffusion into the calcium during the gelation step (Figure 5.6).

Our goal in the fabrication of alginate in the form of microbeads was to produce a platform that would protect incorporated reagents from the electrospinning solvents typically used to produce tissue engineering scaffolds. We had initially planned on placing these beads directly into the electrospinning solutions with the PCL polymer and electrospinning them into the scaffold at the time of fabrication. The small dimensions of the microbeads (in a dry state less than 5 microns in diameter) make them suitable for this type of use. However, given the poor capture efficiency that we observed, a far more reliable strategy would appear to be the use of alginate threads. It may be possible to produce the supplemented threads and then simply grind them into a powder using mortar and pestle prior to adding the material to the electrospinning solutions.

In addition to the capture efficiency, the release kinetics represents another important characteristic of any delivery platform. The alginate threads prepared from higher concentrations of alginate exhibited prolonged and sustained release of the growth factor with respect to constructs produced with lower concentrations of alginate. The early stages of release from all formulations were marked by a burst of release on day 1 (all alginate forms, using varied alginate

and / or NGF concentrations). This would suggest that a fraction of the NGF adheres to the surface or near the surface of the alginate structures and that it can diffuse freely from this compartment upon hydration. As necessary this fractional loss during the early stages of release might be reduced through the use of additional coatings of alginate and other polymers. However, this burst of release may be desirable, when an alginate thread is placed into an electrospun scaffold a fraction of the released material does appear to become trapped on the surrounding electrospun fibers. In effect, this burst of release and subsequent adhesion or trapping on the electrospun fibers may produce yet another functional compartment for the release of materials. As reflected in the ELISA assays, reagent release is more uniform after day 2 of incubation (Figure 5.10), suggesting this release originates from a different kinetic compartment. This secondary compartment may originate with the breakdown of the alginate and or the diffusion of NGF out from the internal pores that we observed in our SEM study.

We have shown integration of an NGF-loaded alginate thread into and between the fibrillar arrays of a 3D nerve guide results in the localized release of growth factor inside the construct. Controlled release studies with alginate threads placed into an electrospun scaffold composed of PCL suggest that about 30% of any NGF that is expected to be released from the alginate compartment becomes trapped on the fibers and fails to diffuse out of the constructs. Cell culture experiments conducted with explanted DRGs confirm the functionality of NGF released from the alginate threads.

We expect that an even higher concentration of NGF will be trapped in the “fibrillar” compartment of a 3D nerve graft that has been fabricated with the external coating of PGA/PLA copolymer that we use when the devices are to be used *in vivo* to reconstruct a damaged nerve. We elected to conduct our *in vitro* release assays without this coating to allow us to examine the

intrinsic interactions of the released NGF and the fibrillar arrays. We note that regardless of how these release studies are conducted, there are nearly insurmountable technical limitations. As noted, our 3D nerve guides are typically over-coated with a PGA/PLA to reduce interstitial cell penetration into the fiber arrays in an implant study. The distal ends of these constructs are sutured to the nerve stumps. Together, these circumstances effectively seal the internal aspects of the constructs from the surrounding tissues. To produce and evaluate the release of factors from a nerve guide in that mimics these conditions using *in vitro* experiments will result in the fabrication of a construct in which virtually no NGF can escape. Without the ability to recover the released NGF, kinetic measurements cannot easily be made. Conversely, using a guide without the overcoating allows us to measure release, but this type of construct does not really very accurately reflect the conditions observed in a construct placed *in vivo*.

One possible method to address some of these issues may be to conduct *in vitro* assays with a fully fabricated nerve guide (3D graft plus the overcoating) using radioactively tagged NGF. By fabricating a series of replicate scaffolds it may be possible to trace the diffusion of the tagged NGF along the longitudinal axis of the constructs. Replicate scaffolds could be isolated at intervals, cut into cross-sectional segments and assayed for the labeled material. This approach has limitations in the evaluation of NGF distribution in the radial axis. It would be difficult to discern how the labeled material is compartmentalized in domains where alginate is still intact. Determining if any particular fraction of the labeled material is associated with the fibers or still retained within alginate would remain a relatively complex task. Still, this approach has merits and it should provide good kinetic data overall to complement the experiments described in this chapter. In the end the most critical assay that can be conducted is one that is conducted under actual regenerative conditions as undertaken in the next chapter of this thesis.

CONCLUSION

We characterized a delivery platform using alginate that can be incorporated into electrospun scaffolds. This construct was designed to deliver therapeutic reagents over a prolonged period of time and at precise locations in a regenerative environment. The fabrication processes used to produce alginate threads are very simple and straightforward, and provide an avenue to produce signaling gradients over relatively short distances. The simplicity of this approach makes it possible to load the threads with different concentrations and/or different growth factors and deliver those materials in a spatially and temporally to the regenerative environment.

CHAPTER 6

Chapter 6. Electrospun 3D nerve guides: A comparative study

***Preface**: Our objective is to develop a next generation nerve guide that can supplant the autologous graft which is considered as the gold standard treatment for peripheral nerve injuries; our pilot data presented in Chapter 3 of this document clearly shows that our design has great promise. Those studies confirmed that our device can support axon growth in tissue culture experiments and nerve regeneration in vivo. However, to truly replace the autologous nerve graft, we must directly compare and contrast the performance of our designs with this standard of care. This chapter describes a study in which we directly compare and contrast the performance of our 3D design with an autologous graft, and conventional hollow core graft in a rodent model of a long defect injury to the sciatic nerve. In addition to making this basic comparison, we also examine how 3D graft enhanced with an NGF gradient prepared after the methods described in Chapter 4 impacts the regenerative process. We use a variety of structural and functional metrics to characterize our grafts and evaluate the results of this expanded study.*

ABSTRACT

Robust axon regeneration can occur after peripheral nerve injuries, provided that a proper regenerative environment is present to support the process. This study is designed to test the performance of a unique 3D nerve guide fabricated from PCL using two pole air gap electrospinning. These 3D guides were fabricated with / without an exogenous source of NGF and compared against autologous nerve grafts and hollow core nerve guides in a rodent model of a long defect nerve injury in the sciatic nerve (15 mm lesions). Functional and structural metrics were used to evaluate the different treatments. The animals treated with 3D nerve grafts displayed more rapid and increased functional recovery with respect to animals treated with autologous nerve grafts and hollow core nerve guides.

INTRODUCTION

Peripheral nerve undergoes an astounding degree of regeneration; however, the surgeon, office worker, or hobbyist that has experienced a long defect injury is unlikely to regain the strength and or fine motor control that is necessary to truly re-engage in pre-injury pursuits [76, 77]. Insidious "time-to-regeneration" barriers imposed by autologous nerve graft material and conventional nerve guides play a central role in limiting the extent of functional recovery that can be achieved after a nerve injury.

In humans, long defect peripheral nerve injuries (>3 cm) must be treated by surgical reconstruction using an autologous graft or an engineered nerve guide; direct anastomotic repair places too much tension across the tissue and results in a poor regenerative response [78]. Despite extensive research, the autologous nerve graft remains the gold standard treatment for these devastating injuries. However, this approach has well recognized inherent limitations. There is paucity of donor nerves for autologous grafts; mismatch of the donor nerve size and / or length with the recipient nerve site is very common limiting completely successful regeneration; the secondary surgery for extracting the autologous graft increases intraoperative time, exacerbates the risk of infections, and results in donor site morbidity. Additional complications that may develop at the donor site include the evolution of neuromas and or hyperesthesia [50, 79]. Far more importantly, autologous material retains axonal debris that must first degenerate before regenerating axons can pass through the graft. Regeneration across this type of graft is further slowed by proteoglycans that accumulate in the tissue and the adjacent nerve stumps, in response to injury [80].

Interventions that reduce the regeneration delays associated with the time it takes axonal fragments in an autologous graft to degenerate represents a crucial avenue for improving functional outcomes, and patient quality of life [81]. Achieving this goal is, in part, is one reason why so many different nerve guide designs have been developed and promulgated as next generation treatments designed to replace autologous material. Reducing the regeneration delay is critically important because denervation leads to the onset of atrophic changes in the downstream tissues. Within hours of denervation, motor endplates undergo re-organization [82] and the terminal Schwann cells spread into the synaptic cleft [83]. Over time the motor endplates disperse, and the fine structure of the neuromuscular junctions is lost [84]. Disuse atrophy evolves in the underlying muscle tissues [85-88]. Once these degenerative changes become entrenched, the neuromuscular junctions will fail to fully reform even when axons are restored to the muscle [89]; not surprisingly, the prospects of significant functional recovery are very limited under these circumstances.

A broad variety of nerve guides have been developed and explored, with mixed and limited success, as indicated by the continued use of autologous material [90, 91]. To address the limitations imposed by autologous material and the time-to-regeneration barriers that ultimately limit functional recovery, we have developed a 3D “semi-solid” nerve guide that mimics the anisotropic structure of native tissue [2]. These constructs are fabricated from the biocompatible polymer, poly-ε-caprolactone (PCL) using two pole air gap electrospinning. This modification of the electrospinning process produces seamless, cylindrical constructs that are composed of dense, highly aligned arrays of PCL fibers that are oriented in parallel with the long axis of the guides. Unlike conventional hollow cylindrical guides, and electrospun variants of this simple

tubular design [50], our 3D guides lack the central lumen (hence "semi-solid"); axons grow along the aligned fibers within the longitudinally arrayed intra-fiber spaces.

Our pilot study concentrated on describing our fabrication techniques and clearly demonstrated the efficacy of the 3D design in the repair of a 10 mm lesion in the rodent sciatic nerve. In this study, we use a battery of functional and structural metrics to compare and contrast the performance of the 3D design with respect to the autologous graft and a conventional hollow core cylindrical graft using a long defect injury in the rodent sciatic nerve. We also describe our strategies to incorporate therapeutic reagents directly into our constructs to enhance graft performance. The basic 3D nerve guide design **(A)** improved Sciatic Functional Index (SFI) scores **(B)** and accelerated recovery of the withdrawal reflex to pain within 30 days with respect to autologous grafts and conventional hollow grafts. In conjunction with these functional metrics animals treated with the 3D grafts also exhibited evidence of dramatically improved nerve-to-muscle signal amplitudes and increased gastrocnemius muscle mass. These preliminary results are unprecedented and superior to results reported in the literature for a variety of existing graft designs [92-97].

METHODS

Electrospinning

All reagents were purchased from Sigma-Aldrich unless noted. Polycaprolactone (PCL 65,000 M.W.) was dissolved in 1,1,1-trifluoroethanol (TFE) overnight at a concentration of 200 mg mL^{-1}. 3D nerve guides were fabricated after the methods of Jha et al., 2011 [2] as described in Chapter 4 using two pole air gap electrospinning. The hollow tube nerve guides were prepared by spinning PCL (200 mg mL^{-1} TFE) onto a rotating (100 rpm) stainless steel 1 mm diameter grounded mandrel. Electrospinning conditions were optimized such that the nominal average PCL fiber diameter was 1 μm for all electrospun constructs. The 3D and hollow tube nerve guides were over-coated with a layer of 50:50 PGA/PLA co-polymer (100 mg mL^{-1} in TFE). This layer induces the formation of a fibrotic capsule on the surface of the electrospun guides and serves to reduce interstitial cell infiltration into the fiber arrays [19]. All electrospun constructs were calibrated to match the cross sectional diameter of the intact sciatic nerve.

Alginate Thread with NGF

A stock solution of sodium salt of alginic acid from brown algae (Sigma-Aldrich) was prepared in deionized water at a concentration of 12.5 mg mL^{-1} and supplemented with 10 mg mL^{-1} Bovine Serum Albumin (BSA). A 25 μL volume of this solution was supplemented with 15 ng NGF and placed into a segment of PVC tubing with inner diameter of 2 mm (Nalgene). The aliquot was frozen at -70 ˚C for 15 minutes. Using a thin plunger, the frozen alginate-BSA-NGF solution was extruded into 100 mL of 2% calcium chloride prepared in deionized water and allowed to incubate for 10 minutes. The resulting “alginate thread” was

rinsed in 2% calcium chloride supplemented with 10% propanol and dried under vacuum for 4 hours. This fabrication strategy for capturing NGF into the alginate is approximately 50% efficient. Alginate threads containing NGF were placed directly into the forming fiber arrays during the electrospinning process. This was achieved by initiating the formation of a 3D graft in the two pole electrospinning system and stopping the process after the graft was 25-50% complete. A single alginate thread was placed onto the electrospun fibers suspended between the two target poles. After the placement of the alginate thread, the process of electrospinning was resumed to completion. We assume based on empirical experimentation that the final NGF concentration present within the grafts is 7.5 ng/implant.

Surgical Manipulation

Adult Long Evans Hooded rats (Harlan laboratories) were brought to a surgical plane with isoflurane, sciatic nerve exposed as described in Jha et al. [2]. Depth of anesthesia was verified by the absence of a corneal reflex and maintained with isoflurane delivered via a nose cone. A 15 mm lesion was introduced into the left sciatic nerve and reconstructed with a 15 mm segment of a 3D electrospun nerve guide (plus or minus NGF), a hollow core electrospun cylindrical nerve guide or an autologous graft (N=3 for each permutation). Autologous material was prepared by removing a 15 mm gap from the sciatic nerve and flipping that tissue 180º prior to surgical placement. All implants were anchored with two sutures (10-0 Ethicon). For the electrospun grafts, the sutures were placed through the outer layer of PGA/PLA and the epineurium of the native tissue at its proximal and distal ends, for the autologous implants the sutures were placed through the epineurium of both the implant and the proximal and distal ends.

Additional fiduciary sutures were placed in the epineurium of the adjacent native tissue to mark the injury borders.

Functional Recovery Analysis: Sciatic Functional Index (SFI) for Motor Function

SFI was used to monitor motor functional recovery [92]. All animals were assessed at day 10, 20 and 30 after surgery. On days 40-60 after surgery animals evaluated every 5 days. Animals were trained to walk along a track with a clear bottom; data for gait and footprint analysis was captured using a video recorder positioned underneath the walking track. Single images were captured from the videos using Sony Vegas Pro software. To ensure that footprint analysis was conducted when the limb of interest was fully weight bearing, still images were captured from the videos when the contralateral leg was flexed and retracted from the surface of the track at the midpoint of the stride. SFI was calculated from the average of 5 "footprints" from each hind paw based on the Bain's formula [92], where:

$$\text{Sciatic Functional Index} = -38.3\,(\text{PLF}) + 109.5\,(\text{TSF}) + 13.3\,(\text{ITF}) - 8.8$$

PLF (Print length function, distance between heel and longest toe) =

$$\frac{Experimental\ foot\ \ print\ length - Normal\ foot\ print\ length}{Normal\ foot\ print\ length}$$

TSF (Toe function, distance between 1st and 5th toe) =

$$\frac{Experimental\ foot\ toe\ spread - Normal\ foot\ toe\ spred}{Normal\ foot\ toe\ spread}$$

ITF (Intermedian toe function, distance between 2nd and 4th toe) =

$$\frac{Experimental\ foot\ intermedian\ toes\ distance - Normal\ foot\ intermedian\ toes\ distance}{Normal\ foot\ intermedian\ toes\ distance}$$

All images were calibrated for measurements from a scale bar captured at the time of data acquisition.

Functional Recovery Analysis: Withdrawal Reflex for Sensory Function

Withdrawal reflex to noxious heat was used to monitor sensory recovery. Animals were positioned so that one foot of the rear extremity was placed in contact with hot plate set at 56 ˚C. The pain withdrawal reflex was defined as the interval of time between contact with the plate and hind limb retraction (each hind-limb is tested 3× with a 2 minute inter-trial interval and a maximum exposure time of 10 seconds). Data was collected on day 10, 20, 30, 40, 50 and 60 on the evenings of SFI evaluation; individual trials were averaged.

Statistical Analysis

The SFI and withdrawal reflex studies consisted of 3 animals from each treatment group for days 10-30, two animals from each treatment group for days 31-45 and one animal from each treatment group for day 45-60. A two-way repeated measures ANOVA was used to screen the data from the SFI and withdrawal reflex studies conducted on day 10, 20 and 30 after surgery, where variable 1 = implant identity, and variable 2 = time interval after surgery. Output was SFI score or time to withdrawal. The Holm-Sidak method was used for *post hoc* analysis in each study for these data sets (p values as reported). No statistical treatment was used for the later time points as there were insufficient samples for analysis after day 30 due to the nature of the study design.

Electrophysiology

Selected animals were brought to a surgical plane with 2.5% isoflurane. Hair was removed from the hindquarters, and skin was swabbed with betadine. Skin and muscle overlying the sciatic nerve was mobilized and the sciatic nerves in both the hind limbs were exposed. The

Compound Action Potential amplitude (signal amplitude) of the sciatic nerves was recorded across the test distance. This amplitude is an indirect measure of the total axonal innervation across the distance between the electrodes. For nerve-to-nerve amplitude testing across the reconstructed tissue, electrodes were placed on native tissue immediately rostral and immediately caudal to the lesion site. When recording nerve-to-muscle amplitudes, stimulating electrode was applied rostral to the implant site and a recording electrode was positioned in the gastrocnemius. After placing the electrodes, the stimulus voltage was increased to obtain the maximum amplitude of the compound action potential between the stimulation and the recording electrodes. Beyond this maximal stimulus voltage, a further increase in stimulus voltage produced no further increase in the compound action potential amplitude. Nicolet Viking Select Electromyography machine was used for testing.

Tissue Processing

Tissues were isolated for analysis from each treatment group at day 30, 45 and 60 after surgical reconstruction. Animals were injected with euthasol, flushed with 200 mL of sterile PBS and perfusion fixed with 4% paraformaldehyde plus 0.5% glutaraldehyde using a transcardial puncture. After 24 hr, sciatic nerve tissue was removed and immersion fixed for an additional 24 hr at 4 ºC in 4% paraformaldehyde plus 2% glutaraldehyde prepared in 0.1 M Cacodylate buffer. They were washed 3× in 0.1 M Cacodylate buffer and post-fixed in 1.0% osmium plus or minus 2.5% potassium ferricyanide for 1 hr [2, 19]. All samples were subjected to a graded series of alcohol dehydration (starting with 50% ethanol for 15 min, then 70% ethanol for 15 min, next 95% ethanol for 15 min, then 100% ethanol 2× for 15 min). Samples were next embedded in 1:1 Poly/Bed(Polysciences):Propylene oxide for 2 hr, followed by embedding in

2:1 Poly/Bed:Propylene oxide overnight in dessicator. A Leica EM UC 6 ultramicrotome was used to make semi-thin sections of 0.5 μm for morphometric studies and to make ultrathin sections of about 60-70 nm for TEM imaging.

The lumbricals were recovered from the control and experimental limbs and immersion fixed for an additional 24 hr in 4% paraformaldehyde plus 0.5% glutaraldehyde. Simultaneously, gastrocnemius muscles from the control and reconstructed legs were recovered, minced, lyophilized to obtain the dry weight mass. We expressed gastrocnemius muscle mass observed on the experimental side as a percentage of muscle mass on the contralateral side to control for any differences in overall rodent body mass.

Motor-End Plate Staining in the Lumbricals

Lumbricals were washed for 10 min in PBS at room temperature and then incubated in 0.1 M glycine plus 0.1% Triton x-100 and 1% BSA in PBS for 15 min. Tissue was placed onto an orbital shaker for 1 hr at 4 ºC with Texas red-conjugated α-bungarotoxin (1:1000 dilution) in PBS. The lumbricals were then compressed overnight between two microscope slides, recovered and mounted on in Vectashield and imaged using a 63× objective on Leica TCS-SP2 AOBS Confocal Laser Scanning microscope. The data images presented in this study represent stacked, maximum data sets of the individual Z scans (ImageJ software).

Morphometry

We sampled the proximal domains that were 1 mm into the reconstructed tissue, at the midpoint of the reconstructed tissue, 1 mm proximal to the distal border of the lesions and 1 mm caudal to the distal attachment site of the implants (represents the number of axons that

completely regenerated across the lesion). Semi-thin sections were prepared and stained with a solution of 0.1% Toluidine Blue, 0.1% Methylene Blue, 0.1% Azure II in 1% sodium borate. To calculate the total nerve cross-sectional area, montages from the implants were prepared using size calibrated digital images captured using a Nikon TE 3000 microscope equipped with a 10× brightfield objective. Individual images were assembled using the automated montage function of Adobe Photoshop. The cross-sectional area of the different domains of the grafts were calculated from the montage images using analysis tool of Adobe Photoshop software as defined by the fibrotic capsule induced by the PGA/PLA layer or the epineurium of autologous material. For morphometric analysis of myelinated axon content, a 100× oil immersion lens was used to capture digital images at intervals of approximately every 500 μm throughout the nerve cross-section at a resolution of 3072 × 3072 covering an area of 125 μm × 125 μm. The number of myelinated axons present in each data image was determined by non-biased sampling methods. Each raw data image was subdivided into a series of twenty five 25 μm × 25 μm squares using a 5 × 5 grid. Of these twenty five squares in each raw image, alternate squares were used for the morphometrics, *i.e.* of the total twenty five squares in each raw image, either twelve or thirteen squares were used for myelinated axons counts depending on whether the first square was included for the analysis or not. The raw data images from each cross-section sample were divided into two groups. In images of the first group, the first square was included in the analysis, resulting in thirteen squares for axon counts from those images; in the second group the not the first, but the second square was included in the analysis resulting twelve squares for axon counts from those images. Additionally, the myelinated axons touching the top and the left border of each square were excluded from the counts and the myelinated axons touching the bottom and the right border of each square were included in the count. To extrapolate the total

number of axons present in the cross-sectional area, the density of myelinated axons in the sampled images was multiplied by the total cross-sectional area of the grafts. Total myelinated axon number was extrapolated from morphometric studies using the total cross sectional area of the reconstructed tissue. All measurements were calibrated with a stage micrometer.

Electron Microscopy

Ultrathin sections were obtained after tissue processing as detailed above and all ultrastructural analyses were conducted with Jeol-1230 electron microscope equipped with a Gatan UltraScan 4000SP 4K x 4K CCD camera.

RESULTS

Functional Recovery Analysis – Sciatic Functional Index (SFI)

The loss of sciatic nerve function compromises ankle dorsiflexion in the rodent and results in characteristic defects in the foot morphology resulting in gait deviations which gradually resolve as the distal muscles are innervated by the regenerating axons of the sciatic nerve. The SFI exploits these characteristics to generate a score that reflects the extent of sciatic nerve function present at any given time after the surgical intervention. On this functional index scale -100 represents complete impairment and 0 represents normal functioning.

Treatment groups consisted of 3 animals each in the SFI analysis through day 30, making it possible to use two-way repeated measures ANOVA to evaluate the functional profile of the different treatment groups over this interval. A graphical depiction of the time course of SFI scores is presented in Figure 6.1 and a summary of the statistical results are presented in the Table 6.1.

On post-operative day 10, the first day of evaluation after the surgery, the degree of dysfunction was consistent across the different treatment groups with a mean SFI of approximately -73.50 (Figure 6.1). Between days 10 and 20, the SFI for each treatment group deteriorated with respect to day 10. This deterioration was most pronounced in the animals treated with the autologous graft; this treatment group generated an average SFI of -94.99 at day 20 ($p < 0.001$ with respect to day 10). On day 20, animals treated with hollow grafts had an average SFI decline to -87.21 ($p < 0.001$ with respect to day 10), animals treated with the 3D grafts had their SFI decline to -81.79 on day 20 ($p < 0.001$ with respect to day 10), and animals treated with 3D grafts + NGF had their SFI decline to -83.67 ($p < 0.001$ with respect to day 10).

At day 20, the SFI scores for animals treated with the 3D grafts + NGF (-83.67) vs. the hollow grafts (-87.21) and 3D grafts (-81.79) vs. 3D grafts + NGF (-83.67) were not statistically different from each other; however, the SFI for animals treated with the 3D grafts (-81.79; $p < 0.001$) were improved with respect to animals treated with autologous grafts (-94.99) and the hollow grafts (-87.21) at this time point. Additionally, animals with autologous grafts ($p < 0.001$) had lower SFI scores as compared to animals with hollow and 3D grafts + NGF. Overall the decline in SFI scores at day 20 is most likely associated with the evolution of atrophy in the distal muscle tissues.

On day 30, the different treatment groups remained stratified. The average SFI for the animals treated with the autologous material improved to -81.93 ($p < 0.001$ with respect to day 20). Animals treated with the hollow grafts showed no measurable improvement on day 30 (-86 with respect to day 20 -87). Animals treated with the 3D grafts improved to -73.85 ($p < 0.001$ with respect to day 20) and the 3D + NGF group improved to -76.02 ($p < 0.001$). At day 30, the SFI score for animals treated with the 3D grafts and 3D + NGF grafts was higher with respect to animals treated with the autologous grafts ($p < 0.001$) and the hollow grafts ($p < 0.001$); and the autologous treatment group was better than the hollow core grafts ($p = 0.005$). There was no difference observed in the performance of animals treated with 3D grafts and 3D + NGF grafts. These results indicate that motor functional recovery was faster in animals treated with the 3D grafts = 3D + NGF grafts > autologous grafts > hollow grafts over the first 30 days of our study.

Only two animals remained in each treatment group over the interval of day 30 to 45. With only 2 animals per treatment group in these later time points no statistical treatment was applied to these results. However, the graphical depiction of the results depicts plus and minus the standard error to illustrate the range of data collected from the two animals remaining in the

functional studies at this time point. Animals treated with autologous material had an average SFI score of -73.07, hollow graft animals had an average SFI of -79.36, 3D graft animals had an average SFI score of -67.75, and 3D + NGF graft animals had a SFI of -62.73 by day 45.

From day 45 to day 60 there was only one animal in each treatment group. Over this interval, the animals treated with the autologous and the hollow core implants displayed no evidence of any additional motor recovery as judged by the SFI. These two animals in aggregate achieved a SFI score of approximately -75 by this time point. In contrast, the animals treated with the 3D graft or the 3D graft + NGF continued to display evidence of steady improvement over this interval and each attained an SFI of about -52. The trajectory of changes observed in gastrocnemius muscle mass over our study interval (Figure 6.3) provides additional evidence that 3D grafts support a rapid and robust recovery in the peripheral tissues.

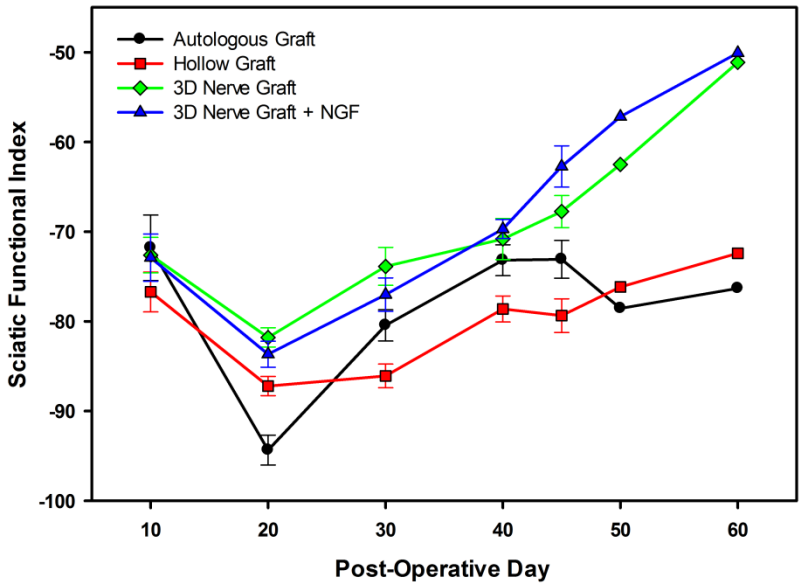

Figure 6.1: Sciatic Functional Index. Functional motor recovery of all the treatment groups. Values near -100 represent impairment as compared to values closer to 0 represent normal motor functioning.

Table 6.1: Statistical analysis for sciatic functional index (SFI) assay.

Statistical Summary I. Time after surgery			
	Day 10-20*	**Day 20-30***	**Day 10-30***
Autologous	$p < 0.001$	$p < 0.001$	$p < 0.001$
Hollow	$p < 0.001$	No	$p < 0.001$
3D	$p < 0.001$	$p < 0.001$	No
3D + NGF	$p < 0.001$	$p < 0.001$	No
Statistical Summary II. Treatment			
	Day 10	**Day 20**	**Day 30***
3D vs. Autologous	No	$p < 0.001$	$p < 0.001$
3D vs. Hollow	$p < 0.001$	$p = 0.002$	$p < 0.001$
3D vs. 3D + NGF	No	No	No
3D + NGF vs. Autologous	No	$p < 0.001$	$p < 0.001$
3D + NGF vs. Hollow	No	No	$p < 0.001$
Autologous vs. Hollow	$p < 0.001$	$p < 0.001$	$p = 0.005$
** N=3 with 9 cases: two-way repeated measures ANOVA; Variable 1=Post-surgery time and Variable 2=Treatment*			

Gastrocnemius Muscle Mass Comparisons

The gastrocnemius muscle is distal to the site of our nerve lesion and it begins to atrophy after de-innervation. As a result, the mass of this muscle after injury reflects the extent of sciatic nerve re-innervation. On post-operative day 30, mass of the gastrocnemius muscle in the impaired limb in the animal treated with the 3D graft was 34%, the 3D graft + NGF was 42% the autologous graft was 39%, and the hollow core graft was 35% of the contralateral side (Figure 6.2). By day 45, the gastrocnemius muscle mass of the impaired limb in the animal treated with the 3D graft was 48% of the contralateral side. In comparison, the impaired limb's gastrocnemius mass of the animal treated with the 3D graft + NGF was 40%, the autologous graft was 31% of controls and the hollow core graft was 29% of controls. By day 60 the affected limb's mass of the gastrocnemius in animals treated with a 3D graft was 55%, 3D graft + NGF was 55% of controls, autologous graft was 42%, and the hollow core graft was only 28% of controls. These data are in support our SFI data indicating that animals treated with 3D grafts with / without NGF undergo a more rapid and extensive degree of nerve regeneration than the other treatment groups.

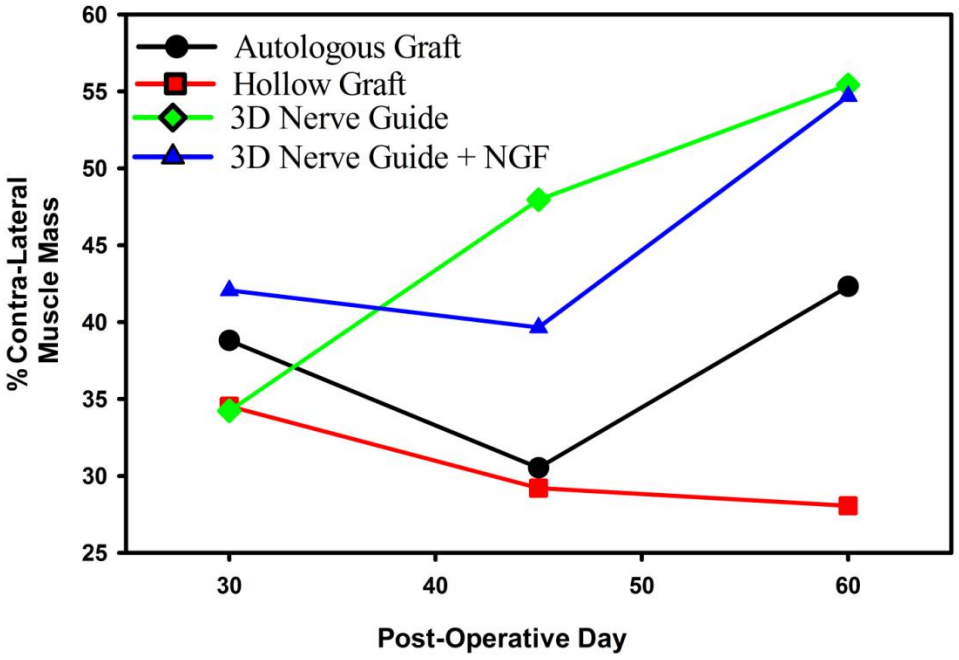

Figure 6.2: Gastrocnemius muscle atrophy comparison. Higher percentage of contralateral muscle mass represents limited muscle atrophy with good regeneration indicative of enhanced peripheral nerve regeneration.

Functional recovery analysis: Withdrawal Reflex.

To monitor recovery in the sensory tracks we used the withdrawal reflex to noxious heat. The results of these experiments substantially parallel the results of our SFI studies, with the exception of the animals implanted with the 3D nerve guide supplemented with NGF. These animals exhibited a much slower rate of recovery for this reflex over the first 30 days of the experiment than animals treated with the un-supplemented 3D grafts. A summary of the results and the p values in the statistical tests are presented in the Table 6.2.

At day 10, the first day of testing, all animals exhibited a statistically identical response to the noxious heat stimulus. The average time for withdrawal reflex in animals with autologous grafts was 9.67 sec, in hollow graft animals was 9.47 sec, in animals with 3D grafts was 9.08 sec, and in animals with 3D graft + NGF was 9.4 sec (Figure 6.3).

No measurable improvement occurred from day 10 to day 20 after surgery in the animals treated with the autologous or hollow core grafts. However, on day 20 there was significant improvement in the animals with 3D grafts (8.37 sec; $p = 0.032$) and in the animals with 3D + NGF grafts ($p = 0.010$) with respect to day 10. Also, animals treated with the 3D grafts and with 3D + NGF grafts had faster response times than the autologous ($p \leq 0.044$) and hollow core grafts ($p < 0.001$) at day 20 after surgery. There was no difference in the response times for the animals treated with the autologous graft and the hollow core grafts at day 20; similarly, there was no difference between the 3D graft animals and 3D + NGF graft animals at this time point.

With the exception of the animals treated with the 3D + NGF grafts, all treatment groups exhibited an improved withdrawal reflex by day 30 with respect to day 20 ($p < 0.001$). The animals with 3D grafts responded markedly faster than animals treated with the hollow core grafts ($p < 0.001$), the autologous grafts ($p = 0.008$), and the 3D + NGF grafts ($p < 0.001$) at this

time point. The animals treated with the autologous grafts exhibited faster withdrawal reflexes than the animals treated with the hollow core grafts ($p = 0.001$).

As with the SFI study, only two animals remained in the withdrawal reflex study from days 30-45. No statistical treatment was applied to these results, however, the graphical depiction of the results depicts plus and minus the standard error to illustrate the range of data collected from the two animals remaining in the functional studies at this time point. The two animals treated with 3D grafts were nearly at control levels by day 45 with an average response time of 4.13 sec and the animals treated with the 3D + NGF graft responded in an average time of 6.89 sec. Animals treated with the autologous grafts had an average withdrawal time of 5.48 sec and the animals treated with the hollow core grafts had an average response time of 8.02 sec.

At day 60 one animal remained in each treatment group, the animal with the 3D graft responded to the noxious stimuli within 1.62 sec (implying hypersensitivity), the animal treated with the 3D + NGF graft responded within 3.35 sec, the animal with the autologous graft responded within 3.63 sec and the hollow graft responded within 7.4 sec. These results indicate enhanced sensory recovery in the un-enhanced 3D graft as compared to all other treatment groups over the first 30 days after surgery.

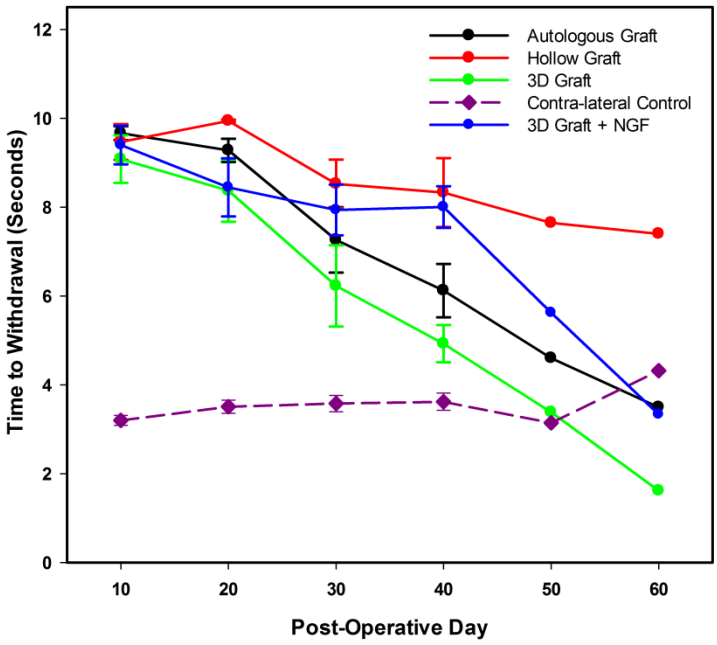

Figure 6.3: Sensory testing using the withdrawal reflex. Functional sensory recovery of all the treatment groups. The animals responding faster or closer to the values of contra-lateral control limb represent better response as compared to higher response time.

Table 6.2: Statistical analysis for withdrawal reflex assay.

Statistical Summary I. Time after surgery			
	Day 10-20*	**Day 20-30***	**Day 10-30***
Autologous	No	$p < 0.001$	$p < 0.001$
Hollow	No	No	$p = 0.010$
3D	$p = 0.032$	$p < 0.001$	$p < 0.001$
3D + NGF	$p = 0.010$	No	$p < 0.001$
Statistical Summary II. Treatment			
	Day 10	**Day 20**	**Day 30***
3D vs. Autologous	No	$p = 0.030$	$p = 0.008$
3D vs. Hollow	No	$p < 0.001$	$p < 0.001$
3D vs. 3D + NGF	No	No	$p < 0.001$
3D + NGF vs. Autologous	No	$p = 0.044$	No
3D + NGF vs. Hollow	No	$p < 0.001$	No
Autologous vs. Hollow	No	No	$p = 0.001$
** N=3 with 9 cases: two-way repeated measures MANOVA; Variable 1=Post-surgery time and Variable 2=Treatment*			

Motor End Plates

SFI, reflex withdrawal studies and changes in gastrocnemius muscle mass all indicate that functional recovery is well entrenched by day 45 after surgical reconstruction in animals treated with 3D grafts. We next examined the motor endplates of the lumbrical muscles of the treated animals as an additional metric to evaluate the regenerative process. For these experiments the motor endplates were stained with Texas red labeled α-bungarotoxin to image the post-synaptic acetylcholine receptors. In control tissues, the motor endplates exhibited classic lobular structure. At day 30 the endplates present were largely unrecognizable. The α-bungarotoxin positive structures present at this time point were indistinct and scattered on the surface of the myotubes as small fluorescent foci, or clusters of foci (Figure 6.4). By day 45, this pattern had undergone a remarkable transformation. At this time point α-bungarotoxin positive features were clustered into structures consistent with that expected for functional rodent motor endplates. At day 60 the motor endplate staining pattern was still evident, however, we note that the staining in animal treated with a autologous graft and the hollow core graft was less distinct than at day 45 and far more difficult to image. Motor endplates in animals treated with the 3D and 3D + NGF grafts were similar to those observed at day 45.

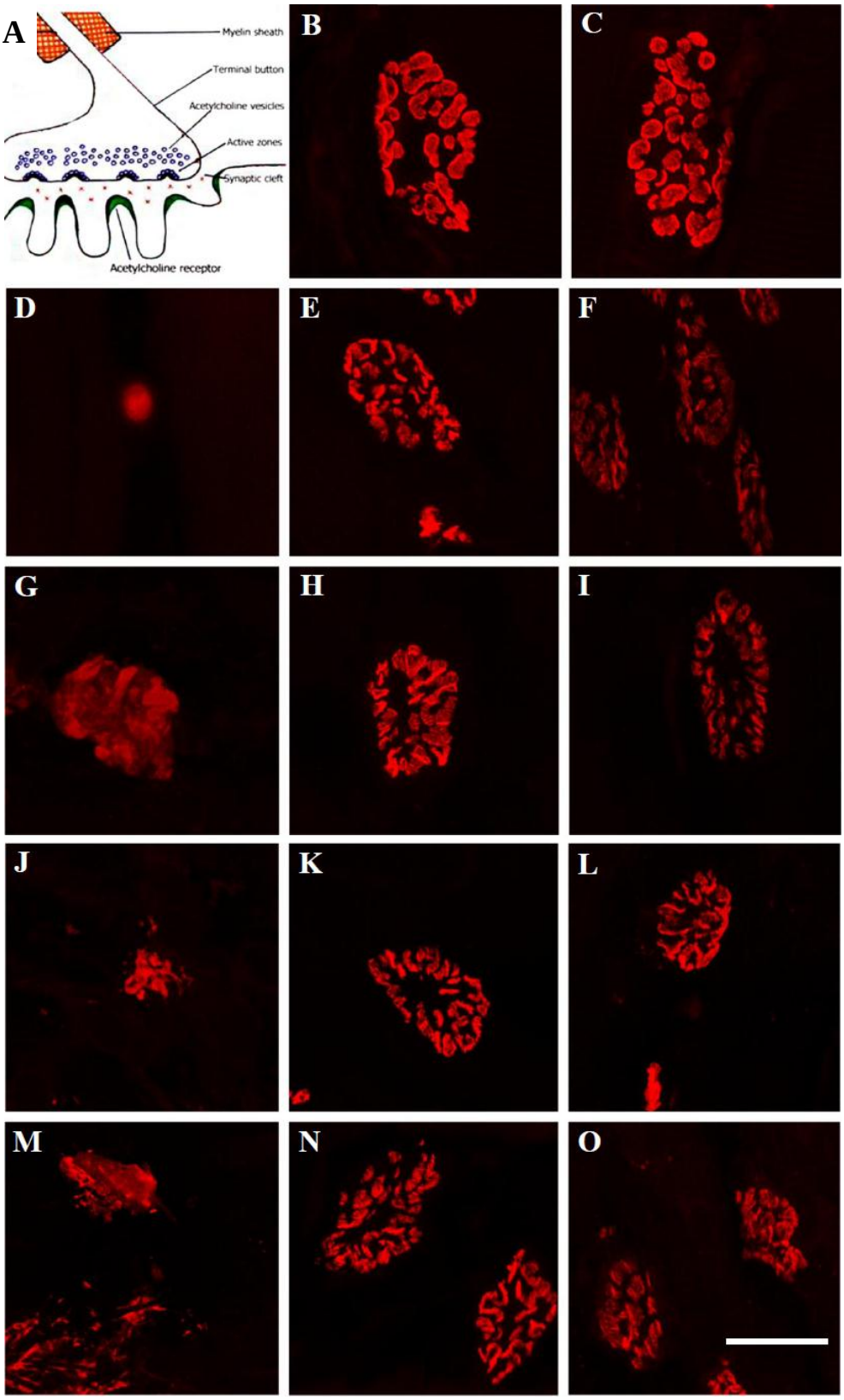

Figure 6.4: Lumbrical motor end plates.

Figure 6.4: Lumbrical motor end plates. Motor end plates labeled with Texas red-conjugated α-bungarotoxin in the first lumbrical muscle of the rodent. (A) Diagrammatic representation of a neuromuscular junction with acetylcholnine receptors shown in green along the crest of post-synaptic cleft. (B-C) Control motor end plates from contralateral normal foot. (D-F) motor end plates of animals with autologous graft at post-operative day 30 (D), day 45 (E), and day 60 (F). (G-I) motor end plates of animals with hollow graft at post-operative day 30 (G), day 45 (H), and day 60 (I). (J-L) motor end plates of animals with 3D graft at post-operative day 30 (J), day 45 (K), and day 60 (L). (M-O) motor end plates of animals with 3D graft + NGF at post-operative day 30 (M), day 45 (N), and day 60 (O). Scale bar in (O) for (B-O) = 20 μm.

Electrophysiology

All of the metrics that we have used to measure functional recovery indicate that day 45 represents a watershed interval and clearly demonstrate that varying degrees of regeneration have taken place in each of the treatment groups by this time point in the distal target tissues. Electrophysiological studies were conducted at this time point to confirm these results. Compound action potential amplitudes, an indirect measure of axon number, were taken across the lesions – "nerve-to-nerve" (electrodes rostral and caudal of the injury gap), and "nerve-to-muscle" (one electrode rostral to the injury site and one electrode in the gastrocnemius muscle). In the nerve-to-nerve study, the signal amplitude in the animal treated with the autologous graft was 303 μV, the hollow graft was 5,729 μV and the 3D graft was 15,104 μV (Figure 6.5). The signal amplitude for the nerve to nerve study in the contralateral normal sciatic nerves in our test rodents ranged from 17,000 to 20,000 μV. Thus, the 3D nerve graft was approaching the normal sciatic nerve's electrophysiological functional properties at this time point. Nerve-to-muscle signal amplitudes at the gastrocnemius muscle in the animal treated with the autologous graft was 17 μV, the hollow core graft was 158 μV and 1,203 μV in the animal treated with the 3D nerve graft (Figure 6.5).

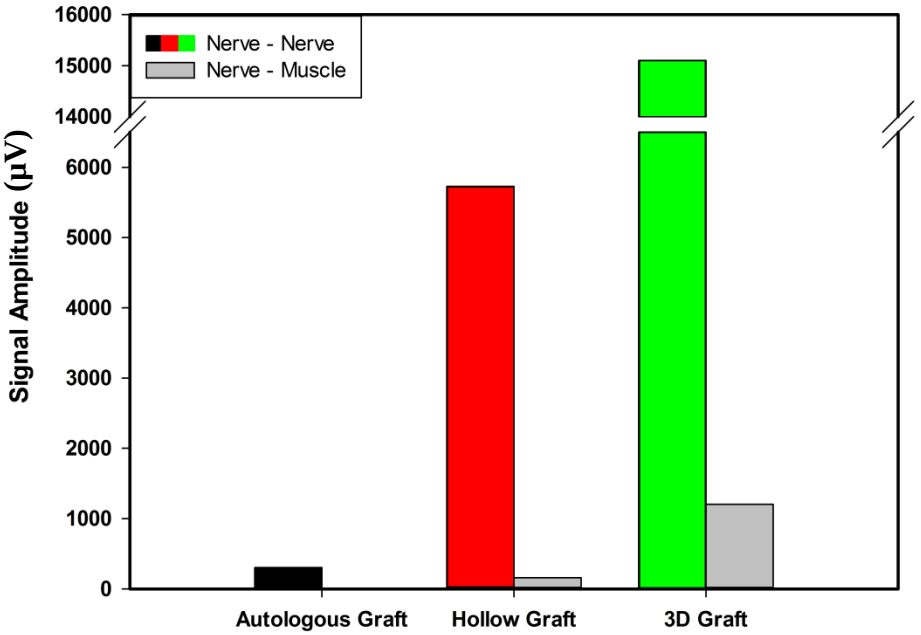

Figure 6.5: Signal amplitudes across the implants at post-operative day 45. Higher nerve-to-nerve signal amplitudes were recorded across the 3D nerve grafts (green), as compared to the hollow graft (red) and autologous graft (black). Nerve-to-muscle signal amplitudes across the native nervous tissue proximal to the injury site and the gastrocnemius muscle were also higher in 3D nerve graft as compared to the hollow and autologous grafts (gray bars).

Morphometric Analysis

To characterize the underlying regeneration response supported by the different graft designs, morphometric analysis was conducted to estimate the total number of axons that crossed the lesion site in each of the different treatment groups. This preliminary survey was conducted using a light micrographic survey of semi-thin cross sections taken from specific domains in the implanted tissue at days 30, 45 and 60. Figure 6.6 illustrates the gross architectural appearance of the autologous, hollow, and 3D grafts at their proximal and distal segments on post-surgical day 45. For each segment of tissue examined, a montage image taken with a 10× objective was prepared from the semi-thin sections (like Figure 6.6A-F), these images were then used to calculate the total cross-sectional area of the implant. A series of 100× images from these sections (like Figure 6.6G-L) were then used to do morphometric analysis to give the myelinated axon count at that segment. Data for myelinated axons was generated for samples taken 1mm into the implanted tissue (denoted as proximal), at the mid-point of the implanted tissue (denoted as middle), 1mm proximal to the caudal attachment site of the implanted tissue (denoted as distal implant) and 1mm distal to the caudal attachment site of the implanted tissue (denoted as distal native tissue).

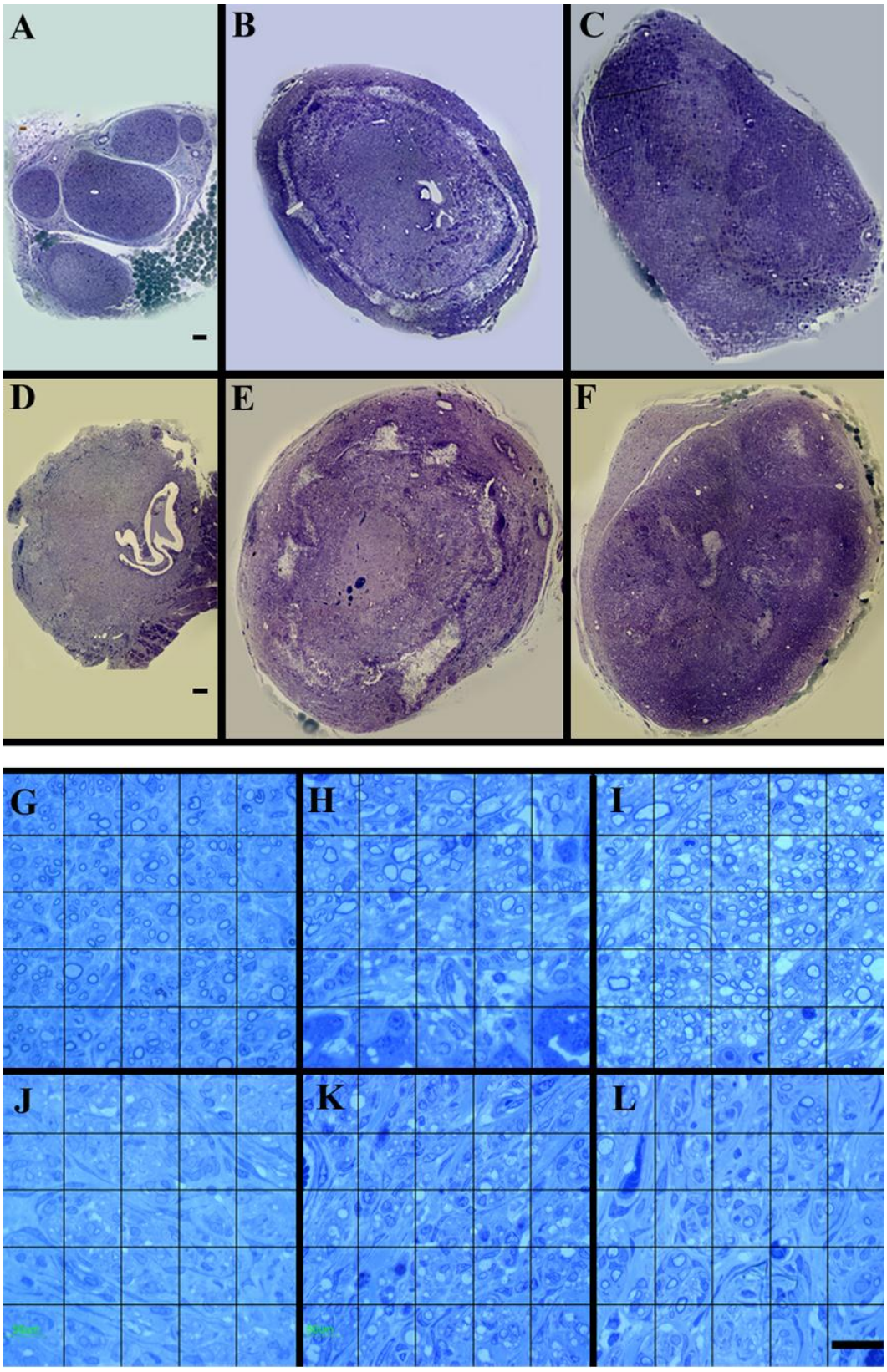

Figure 6.6: Tangential semi-thin sections 45 days post-surgery.

Figure 6.6: Tangential semi-thin sections 45 days post-surgery. Montage images (using 10× lens) of cross-section 3D graft, proximal segment (A-C) and distal segment (D-F): Autologous graft (A, D), hollow graft (B, E), and 3D graft (C, F); all the grafts were well infiltrated with the nervous tissue. Proximal (G-I) and distal (J-L) domains of the implant using 100× lens with the 5 × 5 grid mask used for morphometric analyses: Autologous graft (G, J), hollow graft (H, K), and 3D graft (I, L). Scale bar in (A) for (A-C) = 100 µm, scale bar in (D) for (D-F) = 100 µm, scale bar in (L) for (G-L) = 20 µm.

Figure 6.7 graphically represents the results of the morphometric analysis of the different treatment groups. It summarizes the myelinated axon count at different domains of the reconstructed nerve (proximal, middle, and distal domain of the implant, and the segment of the native tissue distal to the implant) at each of the time points assayed (30, 45, and 60 days).

A brief summary of this data indicates that on post-surgical day 30, autologous and hollow implants exhibited higher counts of myelinated axons at the proximal segment as compared to the 3D graft +/- NGF. We anticipated that our 3D grafts would support a much more rapid penetration of axons than the autologous material. One clear possibility to account for this result may be the compression and distortion of the terminal aspects of the fibers present in an electrospun 3D guide which may occur during surgical placement (in a related study we have observed that the distortion of the terminal aspects inhibits cellular penetration in the central nervous system-data not shown). At day 30 for the proximal section total axon count for the autologous > hollow > 3D > 3D + NGF. No myelinated axons were detected in the distal segments of the hollow, 3D, or 3D + NGF; however, there were a considerable number of axons present in the distal segments of the autologous graft. It is difficult to explain the apparent efficiency at which this graft appears to have supported axon penetration (especially considering the poor functional recovery displayed in this treatment group overall). Day 30 represents a very early time point and while it seems unlikely we can not discount the possibility that these axons in the distal segments of the autologous graft might represent axons which have not yet been completely degraded. Countering this argument, however, are two relevant observations. First, these axons appear to be completely normal at the light microscopic level. Second, axons are completely absent in the native distal segment of the animal treated with the autologous graft, indicating that sufficient time has passed to allow for axonal debris to develop and be removed.

No axons were present in any of the implants in the distal native segment, consistent with our observation that motor-endplates were degenerated at this time point in all of the animals.

On post-surgical day 45, the number of myelinated axons present in the proximal segments of all the implanted grafts was similar. At this time point the total axon count in this domain was highest in the 3D guide > autologous implant > 3D + NGF and the hollow core graft. Total axon count remained highest in the middle segment in the autologous graft. Myelinated axons were visible in the distal native segments at this time point in all of the treatment groups. Total axon counts in this distal domain were highest in the 3D graft > 3D + NGF > autologous > hollow core. Superficially, these results would appear to generally correlate with the electrophysiology data; however it is important to remember that myelinated and non-myelinated axons, both contribute to the formation of the compound action potential amplitudes we observed in the electrophysiological data.

By day 60, the number of myelinated axons present in the distal downstream segments of the autologous and hollow core grafts increased with respect to day 30. This is not unexpected; axons in any particular graft likely grow at varying rates. The distal implant and distal native segments of these two graft designs were populated by more myelinated axons than they were at day 30 after surgery. Surprisingly, and despite clear and unambiguous evidence of a robust functional recovery in animals treated with the 3D and 3D + NGF implants, we failed to detect more than a very small number of myelinated axons in the distal implant or distal native segments in our assay. Of note at this time point is the myelinated axon count in the middle segment of the hollow nerve guide. It is very high as compared to all the treatment groups and also as compared to the axon count in the proximal and distal segment of the same implant. We suspect that this high axon count represents an overestimation of the total number of axons

present in this particular implant; in absence of guidance cues for individual axons in the hollow guide the axons might may have elongated indiscriminately in non-specific directions resulting in the same axon being counted more than once in a cross-sectional data image. The axon cross-sections present in this domain exhibited a variety of profiles (true cross sections, more tangential and partial longitudinal). Axon sprouting undoubtedly may also have contributed to this "inflated" count. The 3D graft exhibited a small increase in axons in the middle segment with respect to more proximal and distal segments, however the magnitude of this increased count was modest compared to the hollow graft. The 3D + NGF graft exhibited a low number of myelinated axons, but each domain in this graft exhibited a very consistent count.

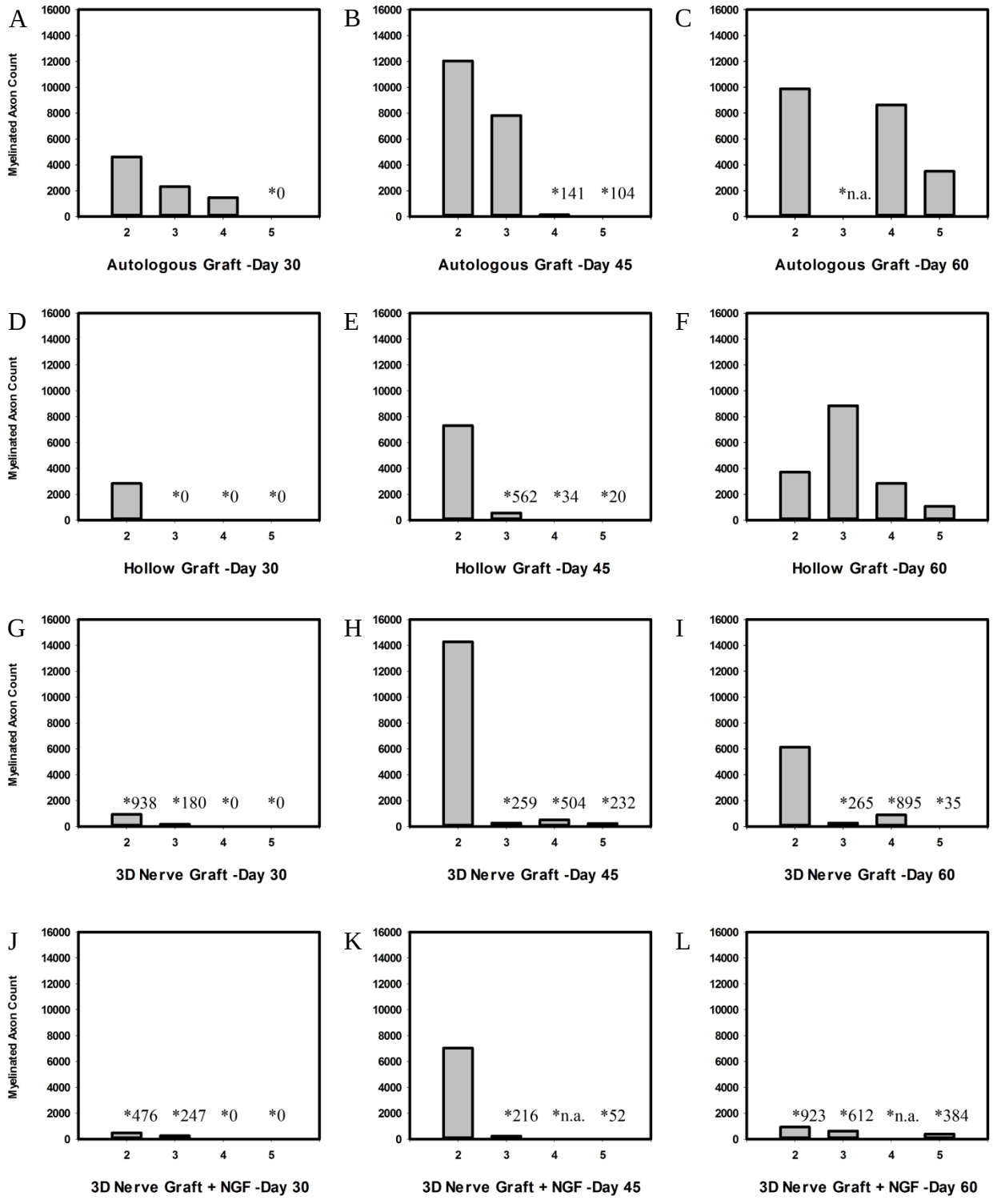

Figure 6.7: Morphometric analysis.

Figure 6.7: Morphometric analysis. Myelinated axon counts at different positions of the autologous graft (A-C), hollow graft (D-F), 3D graft (G-I), and 3D graft + NGF (J-L) on post-surgical day 30 (A, D, G, J), day 45 (B, E, H, K), and day 60 (C, F, I, L). The ticks on the X-axis of the plots indicate the domain of the graft under analysis where 2 = proximal segment of the graft, 3 = middle segment of the graft, 4 = distal segment of the graft, and 5 = segment of native nerve distal to the graft implanted. . *Data points coded as n.a. indicate samples where the entire cross-section of the nerve was not recovered, making a total axon count unavailable.

Electron Microscopy

Ultrastructural analysis (Figure 6.7) indicates that the functional recovery observed in animals treated with the 3D, and 3D + NGF grafts is mediated by multitude of small caliber (ranging up to perhaps 500 nm in cross-sectional diameter), un-myelinated axons. In domains caudal to the distal attachment site of the grafts (regenerated tissue in the remnants of the native epineurium), these axons were frequently observed in small clusters and in association with the basal laminae. While we did observe some axons clustered together that were surrounded by Schwann cells, we rarely encountered myelinated axons, and when we did, these axons were very small with a diameter of than 1000 nm.

In addition to the small caliber, unmyelinated axons that populated these grafts, we observed clusters of cells with cuboidal nuclei arranged in a roughly circular pattern. Examination of these clusters revealed that these cells express complex folds of what we presume to be thin processes of cytoplasm. The nature of these cells and these presumptive cytoplasmic folds remains to be defined. There is no clear evidence of a basal lamina surrounding these, suggesting that they are not Schwann cells.

Implants isolated from animals treated with grafts supplemented with NGF exhibited axons that expressed desmosomes and hemi-demsosomes like structures. These junctions have been observed in regenerating peripheral nerve in rodents treated with acetylcholinesterase inhibitors [98]. The significance of these junctions is not known currently.

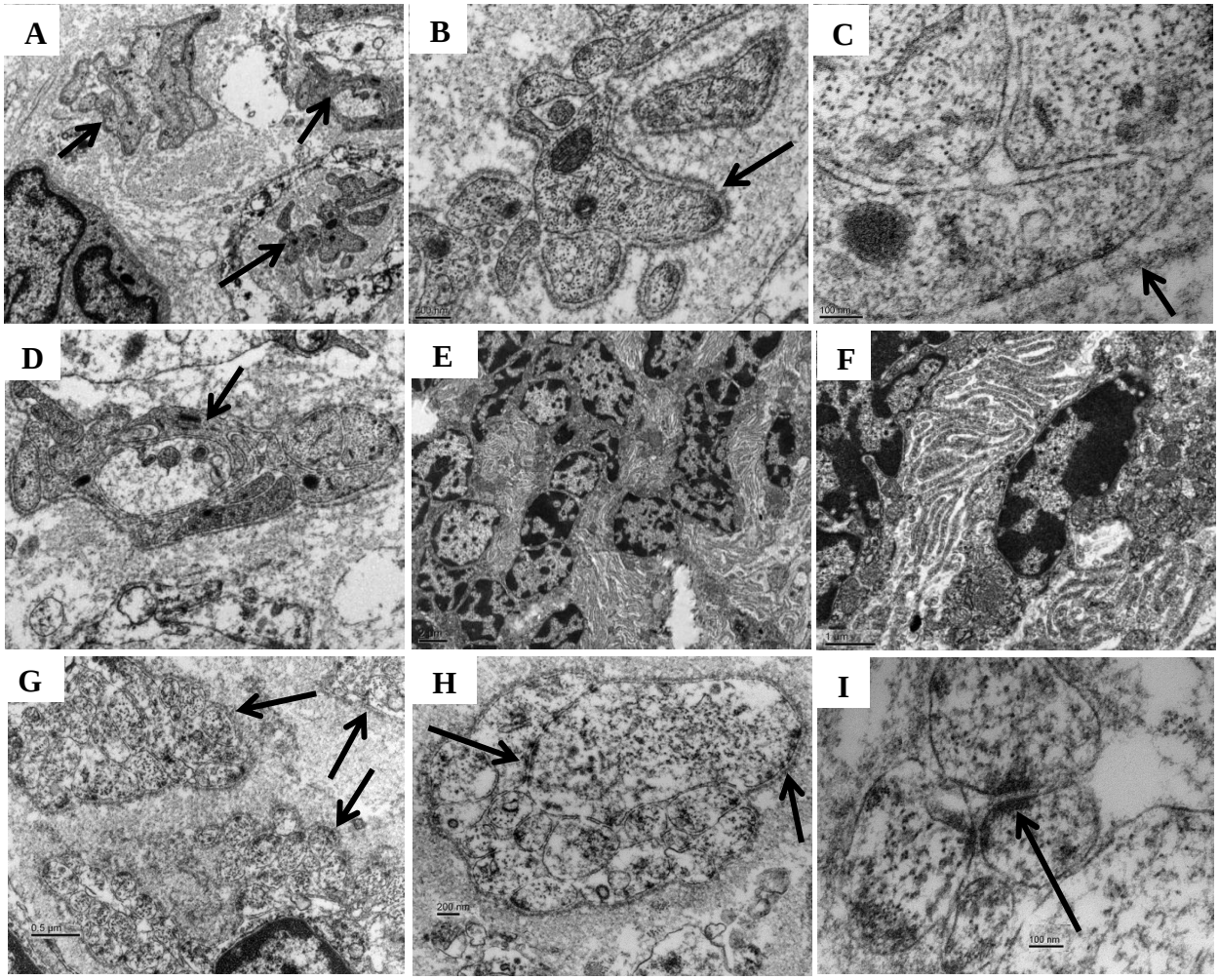

Figure 6.8: Electron microscopy. Electron micrographs from 3D nerve graft animal (A-F) and 3D + NGF nerve graft animal (G-I) on post-operative day 45. Section through the segment distal to the implant (distal native sciatic nerve) (A-D, G-I); section through the implant (E-F). Clusters of small diameter axons (arrows; A) growing within the basal laminae in 3D graft and 3D + NGF graft (arrows; B, C, G, H). Evidence of active myelination by Schwann cells is present (arrow; D). Peculiar to the 3D grafts & 3D + NGF grafts are domains that contain cells with elaborate processes present throughout the implant (E & F); identity of these cells remains unclear. Axons in 3D + NGF grafts expressed desmosomes and hemidesmosomes like structures (arrows; H & I). Scale bar in (G) for (A & G) = 0.5 µm, scale bar in (B & H) = 200 nm for (B, D & H), scale bar in (C & I) = 100 nm, scale bar in (E) = 2 µm, scale bar in (F) = 1 µm

DISCUSSION

Peripheral nerve injuries represent one of the most common causes of sensorimotor deficits and the evolution of subsequent functional limitations. Despite all the attempts developing alternative strategies, the autologous graft remains the gold standard treatment for this type of injury. Unfortunately, and regardless of the treatment strategy, functional recovery after this type of injury is rarely complete [99]. For all too many patients the extent of functional recovery is limited and in many respects nearly cosmetic in nature. For example, in median nerve lesions wrist and finger flexion is compromised. A patient with a lesion to this nerve of the upper extremity that has been surgically reconstructed with an autologous graft may appear normal upon superficial examination. However, he or she may lack the strength necessary to grasp and lift normal everyday objects.

Our goal is to develop a synthetic implant to supplant the autologous graft and develop treatment strategies to improve functional outcomes after traumatic nerve injuries. In this study, we have compared the efficacy of our unique 3D nerve grafts and 3D nerve grafts supplemented with NGF against the autologous graft and the conventional hollow core graft in peripheral nerve regeneration. We have incorporated a variety of structural and functional metrics into this study to characterize the performance of 3D nerve guides in the reconstruction of long defect nerve injuries.

The SFI assay for motor function indicated that our 3D guides (with / without NGF) promoted faster functional recovery over the first 30 days of our study than the autologous and hollow core implants. In addition, the SFI scores for animals treated with 3D guides +/- NGF improved in parallel with one another along nearly identical trajectories, suggesting the

exogenous NGF was not necessary to promote these early stages of recovery. The SFI uses changes in foot morphology and toe position as metrics of nerve function. The absence of normal staining patterns for the endplates of the first lumbrical at day 30 would suggest that regenerating axons have not yet reached these distal muscles at this early time point. The α-bungarotoxin positive features at day 30 appeared as scattered bright foci (a staining pattern that is very different than the staining pattern of motor endplates present in the control side). These critical structures must be in contact with nerve tissue in order to express a normal structural profile (we note that we attempted to double label the lumbricals with α-bungarotoxin and a nerve specific marker-unfortunately, this double labeling procedure produced inconsistent results. As the differences between day 30 and day 45 in the motor endplate staining patterns was so dramatically different we elected to not use this data). By day 30 gastrocnemius muscle mass appeared to be greatly improved in animals treated with the 3D nerve grafts (+/-NGF) with respect to the other treatment groups, suggesting this more proximal tissue had been re-innervated by day 30-at least to some extent. Given these results the improved functional recovery that we observed at day 30 in the SFI was most likely mediated by events taking place in the calf muscles (which are normally exclusively innervated by the sciatic nerve). The muscles of this posterior compartment act on the foot and mediate plantar flexion and toe flexion. Any recovery in these muscles can be expected to impact SFI scores.

Sensory recovery was also enhanced in animals treated with the 3D guides at day 30. Together, these data demonstrate that 3D guides promote faster rates of functional recovery in the motor and sensory neurons than the other treatment options. This functional recovery must be largely driven by small caliber unmyelinated axons; morphometric analysis failed to detect any myelinated axons in the native tissue distal of the implant site at this time point. Such an

unmyelinated population of axons would fall below the limits of detection in a light microscopic survey.

By day 45, the two animals treated with the 3D graft and the two animals treated with the 3D grafts supplemented with NGF continued to exhibit evidence of functional improvements in the SFI and both had increased muscle mass with respect to the other treatment groups. Motor endplate staining also underwent a dramatic change at this time point, each of the different treatment groups exhibited endplates that were substantially identical in structure in the experimental and contralateral control sides. This result would be expected to occur only after some critical number of axons had physically and functionally re-innervated these distal tissues.

At day 45 nerve-to-nerve signal amplitudes were very robust in the animal treated with the 3D guide and approached control values (17000 – 21000 μV), indicating the guides were densely populated with functional axons. And, nerve-to-muscle signal amplitudes between the proximal stump of the injured sciatic nerve and the gastrocnemius muscle were nearly ten-fold higher in this animal than observed in animals treated with the autologous or the hollow core grafts (technical limitations in instrumentation did not allow us to measure signal amplitudes till the lumbricals). In turn, and consistent with these electrophysiological results, our morphometric assays indicated that more myelinated axons were present in the native, regenerated tissue that was distal to the implant site in animals treated with the 3D guides with respect to any other treatment group.

While the 3D grafts did have increased signal amplitudes and an increased number of axons in the morphometric assay it seems likely that the bulk of the functional recovery observed at day 45 (as speculated for day 30) was mediated by small caliber unmyelinated axons. The 3D grafts had more axons but, the magnitude of the difference between this treatment group and the

other treatment groups does not appear to be enough to fully explain the functional recovery or the electrophysiological results. This disparity is particularly distinct when comparing the nerve-to-nerve signal amplitudes in the autologous grafts and our 3D grafts. The signal amplitudes in the 3D grafts are fully 15 fold higher than that observed in the autologous grafts yet the number of myelinated axons is only on the order of 2 fold different. An electron micrographic survey of the distal domains at this time point appears to support this conclusion and revealed numerous small unmyelinated axons in these domains, a more complete quantitative study will be necessary to confirm this hypothesis. There is precedence for this conclusion, results from Radtke and Vogt, 2009 [100] suggest that regenerating axons exhibiting smaller diameters, a thinner myelin sheath and shorter internodes can achieve rapid conduction.

There is no obvious explanation to account for the delayed onset of sensory recovery observed in animals treated with the 3D + NGF grafts that is manifest by day 45. NGF is a neurotrophic factor produced by the target organs of the sympathetic and sensory nerves. This growth factor stimulates neurite outgrowth and promotes survival of sensory ganglia, including those which give rise to spinal sensory nerves in the sciatic nerve [101]. Some reports show that NGF enhances regeneration in motor nerve as well [99]. It seems clear that there must be an optimal time course and concentration of NGF needed to promote regeneration across a long defect nerve injury [102]. NGF has two receptors trkA and p75NGFR. The trkA subtype, is a high-affinity NGF receptor with a K_d of ~1 ng mL^{-1}, is absent in the motor neurons [103]. This would appear to explain why there was no significant improvement in motor recovery (SFI tests) in animals treated with the 3D nerve grafts vs. the 3D + NGF grafts. Conversely, the p75NGFR is a low-affinity NGF receptor with K_d of ~40 ng mL^{-1}. At ***higher*** concentrations of NGF there is marked ***decrease*** in chemotactic effects and a repulsion of growth cones, even at a local

concentration of as little as 1.0 ng mL^{-1} [104, 105]. In a study by Gold, 1997 [106], the continuous intrathecal infusion of NGF delayed the onset of peripheral nerve regeneration, without compromising the rate of regeneration, possibly indicating that the initial loss of NGF following injury might act as signal for the onset of nerve regeneration [107]. We appear to have observed a similar result in our sensory function tests. We have been unable to precisely define the release kinetics of our NGF *in situ*. In part, this is because the NGF is delivered into a very confined space, which is sequestered by a PGA/PLA coating on the graft from the surrounding interstitium. We know from *in vitro* experiments that perhaps as much as 70% of the NGF released over the first several days in a 3D graft becomes associated with the fiber arrays. Based on our sensory metrics, it would seem that a relatively high local concentration of the NGF was present inside these grafts. It is also possible that the NGF present in the graft served as too effective of a chemo-attractant, regenerating axons may reach the domains containing NGF and essentially "stall" until the growth factor is dissipated.

We continued to observe evidence of functional recovery at day 60 in animals treated with 3D guides +/- NGF. In contrast the other treatment groups failed to progress much beyond the level of recovery observed at day 45, despite the observation that animals treated with the autologous and hollow core grafts had far more myelinated axons in the tissue distal to the lesion site. This result indirectly implies that the enhanced functional recovery observed in animals treated with the 3D grafts continues to be driven by small caliber un-myelinated axons. In addition to this consideration the 3D grafts may also be supporting enhanced targeting efficiency. Either scenario or a combination of the two may ultimately underlie the improved functional recovery observed in these animals. We speculate that the unique architecture of the 3D graft could enhance targeting efficiency by confining regenerating axons to a tissue plane that

approximates their position within the nerve prior to injury. The axons would then emerge from the distal end of the graft near the vicinity they existed prior to injury. It would be theoretically possible to test this hypothesis by conducting targeting assays.

.

CONCLUSION

The architecture of our novel 3D grafts is designed to mimic the anisotropic structure of the connective tissue present within the intact peripheral nerve. A synthetic graft with this type of highly anisotropic architecture has been presented as a theoretical replacement for the autologous graft as it should provide the guidance cues necessary to drive the regeneration [41]. In tissue culture experiments two-dimensional surfaces of aligned electrospun fibers prove to be very effective at directing axon elongation along a defined axis in a fashion analogous to the autologous graft [42]. Our present study extends the results of these tissue culture experiments and demonstrates clear evidence that similar results can be achieved *in vivo* using three-dimensional arrays of aligned fibers as a template to drive regeneration.

We observed substantially increased potential for functional recovery when the rodent sciatic nerve was reconstructed with our unique 3D nerve guide. It is curious that the robust functional recovery that we obtained appears to be driven largely by small caliber, unmyelinated axons that were not detectable in our light microscope-based morphometric analysis of the regenerated tissue. An electron microscopic survey was necessary to detect this population of axons. The results of this study are in contrast to our previous results in which we reported that our 3D grafts supported the regeneration and myelination of axons in our rodent model of sciatic nerve injury using a 10 mm lesion gap. It remains to be determined if this discrepancy represents a model specific technical issue or a truly inherent limitation in the design of our device. This issue awaits further investigation. However, we note that regardless of the underlying events that mediated the regenerative response, the extent of functional recovery that we observed in the four animals that remained in the study at 45 days (2 each +/-NGF), and the two (1 each +/-NGF)

animals that remained at 60 days was more rapid and extensive than that observed in animals treated with the ***gold-standard autologous*** implant. In addition, the progress of functional recovery demonstrated by the SFI analyses in our study in the animals treated with the 3D graft was unprecedented with respect to a variety of published results using autologous grafts and various permutations of synthetic and hybrid implants [92-97].

CHAPTER 7

Chapter 7: Conclusions and Future Research

CONCLUSIONS

Regenerative medicine has continued to gain importance in the research enterprise and holds great promise in the treatment of a variety of injuries and disease processes. The goal of this strategy is to stimulate endogenous repair mechanisms and / or to replace damaged or missing tissues and organs by reconstructing or augmenting the structure and function of those damaged tissues. Tissue engineering is an evolving component of the regenerative medicine initiative. This discipline applies the principles of engineering and life sciences to the development of biological substitutes that restore, maintain, or improve tissue function or a whole organ [108]. The tissue engineering technique of electrospinning has gained much prominence due to its ability to produce nano– to micron–scale diameter fibers, a fiber size scale that approaches the scales observed in native tissue. The process of electrospinning affords considerable control over fiber dimensions and the architecture, pore dimensions, and material properties of a tissue engineering scaffold, making it possible to mimic many structural and functional aspects of the native ECM [109].

Electrospinning potentially has a wide variety of potential applications as discussed in Chapters 2 and 3 of this dissertation. Most of the electrospinning applications mentioned in these chapters utilize conventional electrospinning systems where a charged polymer solution source is used to produce a jet of fibers that is directed towards an oppositely charged collecting plate (for randomly oriented fibers) or a rotating mandrel (for aligned fibers). One limitation to these

conventional electrospinning systems concerns the observations that the resulting electrospun fibers are deposited as two-dimensional sheets of material.

There is clearly a place for scaffolds with a two-dimensional configuration in the tissue engineering paradigm. For example, this type of construct clearly mimics the structure of the dermis and the walls of hollow organs such as the esophagus, stomach and intestinal track and the vessels of the cardiovascular system. Data presented in Chapter 3 illustrates how a two-dimensional sheet of electrospun collagen can be effectively be used to reconstruct dermal wounds and its efficacy in the construction of hollow cylindrical tubes for muscle fabrication. While electrospun collagen has unique biological activity in a variety of applications, the architecture of a two-dimensional sheet of material limits its utility. For example, electrospun collagen appeared to induce the differentiation of osteoblasts; however, it is very difficult to envision how the thin two-dimensional sheets of collagen used in these tissue culture experiments might be translated into structures suitable for bone reconstruction. A more three-dimensional architecture is needed for this type of tissue engineering application. Data presented in Chapter 3 also illustrates how critical it is to consider not only the architecture of a scaffold but also how its composition must also be considered in the design of a scaffold for any given application.

It is possible to roll and / or compress a two-dimensional sheet of material into a three-dimensional configuration. However, it can be difficult to reliably reproduce a given structure with this approach and the resulting construct may exhibit poor structural qualities overall. Nor does this approach make it possible to control the distribution and organization of a large population of nano-scale fibers within the final construct. Fiber orientation and distribution play a central role in directing cell migration and determining the mechanical properties of an

electrospun construct [13, 25, 42, 45, 59, 60]. In order to deposit large numbers of nano-scale fibers into the unique structural organization needed to mimic the three-dimensional space occupied by a solid tissue, it would appear to be necessary to fabricate this type of construct at the level of fiber spinning. This allows for subtle and a far higher level of control over the physical properties of a tissue engineering device.

As a component element of this study, we explored the use of two pole electrospinning to develop tissue engineering scaffolds that have been specifically designed to promote the regeneration of peripheral nerves after injury. This tissue presents several distinctive challenges. Peripheral nerve is uniquely structured; it is composed of acellular and cellular elements that are organized into a hierarchical three-dimensional array. Individual axons are surrounded by the endoneurium, a delicate connective tissue layer composed of laminin and Type IV collagen [101]. The investing Schwann cells participate in producing this connective tissue compartment [96, 99]. Bundles of axons are bound together by the perineurium, this layer is composed of Type I collagen. A population of fibroblasts synthesizes and maintains this compartment [93]. Finally, the entire nerve is surrounded by an epineurium, a very tough connective tissue sheath of Type I collagen. Blood vessels lie on the surface of this structure and periodically penetrate into the nerve to provide nourishment. A network of small arterials and capillaries are present within the axonal arrays along the epineurium.

After injury, peripheral axons will readily regenerate. And, even when the process is directed by a hollow tube construct that lacks any discernible guidance cues, a considerable number of axons can be guided to traverse an injury gap [50]. An examination of the regenerated tissue that is present within such a construct indicates that crucial aspects of nerve architecture are recapitulated even in this type of simple device, indicating that the information necessary to

restore the basic structure of nerve is present in the tissue adjacent to the injury. Cross talk between the Schwann cells and axons undoubtedly drives this process [96, 99, 103, 110, 111]. However, based on our comparative study of the nerve guides in Chapter 6, we can say that the rate of regeneration is not very efficient in these devices resulting in limited functional recovery. This limited recovery can be attributed to a number of factors including a poor regenerative response in which only a subpopulation of axons grow across the lesion and / or the subsequent failure of those axons to efficiently target to the appropriate peripheral tissues. A more insidious limitation is the onset of degenerative changes that begin with the loss of nerve function in the peripheral tissues; if nerve function is not restored within a poorly defined window of time (estimates vary as to the length of this critical window, certainly 12 months is adequate for these changes to become entrenched) these degenerative changes may become entrenched. These irreversible changes have been documented in both the motor and sensory target organs [112-114]. Once these degenerative changes are fully entrenched the prospects of functional recovery are essentially non-existent. This observation indicates that it is important to develop strategies to accelerate the return of axons to these distal target tissues and thereby improve the extent of functional recovery that can be achieved after injury.

Two-dimensional sheets of aligned electrospun fibers are very effective at promoting neurite outgrowth to occur along the principle axis of fiber orientation [42-44]. Key to developing a nerve guide is the translation of this fundamental observation into a structure suitable for use *in vivo*. From the onset, our goal was to produce a seamless nerve guide that exhibited a cylindrical structure comprising of fibers that were as uniformly as possible oriented along the longitudinal axis of the construct. Hollow nerve guides fabricated by electrospinning have aligned fibers [50], however, the alignment of the fibers that compose the walls of these constructs is 90^{o} off the

primary axis of axonal growth. As a result of this type of architecture, the hollow device provides limited guidance cues to direct axons towards the distal stump of the injured nerve. Additionally, these hollow devices may be susceptible to crush injury associated with normal everyday activity.

In addition to the criteria that our next generation nerve guide should be composed of nano-scale fibers aligned in parallel with the long axis of the construct, we next we elected to produce a guide with a semi-solid design. This structural design feature is designed to mimic the anisotropic structure of intact nerve. To achieve this goal, we developed and characterized a innovative and novel form of electrospinning denoted as two pole air gap electrospinning. Our studies with this electrospinning technique indicate that high degrees of fiber alignment can be induced with this approach, substantially independently of fiber size (conventional systems that produce 2D sheets of material work best with larger diameter fibers) [2]. We were able to fabricate cylindrical guides composed of aligned fibers that ranged from less than 100 nm to about 2500 nm using the process of two pole air gap electrospinning. Given our architectural constraints, it was essential that our candidate construct exhibit adequate porosity to support axonal penetration into the stacked fiber arrays. Our cell culture and liquid intrusion studies clearly indicated, at least on a theoretical basis, that the 3D design can support axonal growth and elongation into and between the fiber arrays. Those studies (Chapter 4) demonstrated that axonal elongation was supported by scaffolds composed of three very different fiber diameters (approximately 400-2,000nm). We also calculated that the 3D guides exhibited what appeared to be very good overall void space volumes that range from 55% to 95%. In conjunction with these basic structural and functional characteristics, we also wanted the final construct design to exhibit mechanical properties that were sufficient to withstand the forces encountered during

surgical placement (handling and suturing) and the post-implantation movements of the patient. This final selection criteria, that broadly defined the material properties of the final device, narrowed our choices to scaffolds produced to contain fiber diameters of approximately 1 μm. Scaffolds with smaller fiber diameters had substantially less mechanical strength. The semi-solid design was designed with the assumption that axonal growth could be accelerated by a multi-tiered array of individual fibers; essentially the fibers are intended to confine regenerating axons from straying from a linear pathway. In turn this could be expected to increase the efficiency of the outgrowth process and thereby accelerate the regeneration process.

From these selection criteria, we conducted preliminary implant studies in the rodent sciatic nerve using an electrospun guide composed of 1 μm diameter fibers; this construct had material properties that approximated native rodent sciatic nerve, void volumes of approximately 95% and supported directional axonal growth in tissue culture experiments. Using 3D nerve guides with this design we were able to show evidence of sciatic nerve regeneration in rodents subjected to a 10 mm sciatic nerve lesion. The animals in the study group exhibited a 100% survival rate, showed no evidence of overt inflammation or the formation of fibrosis in association with the implants, and developed near-normal gait patterns in the experimental limb by 7 weeks post-surgery. At 7 weeks post-surgery, immunohistochemistry and TEM analysis showed the presence of myelinated and unmyelinated axons, Schwann cells, associated fibroblasts and blood vessels. Morphometric analysis indicated that about 25% of the myelinated axons present at the proximal stump of the injury were directed by the 3D nerve guide to the distal stump of the severed sciatic nerve in the 7 week interval. This study established the efficacy of this 3D nerve guide design.

This initial study, based upon the published sources [39, 93, 115], used what may be considered a sub-critical length lesion of 10 mm. A 15 mm lesion presents a more challenging defect and is clearly considered a long defect nerve injury in the rodent sciatic nerve. The results of the pilot study using the 10 mm lesion indicates that there were sufficient endogenous sources of neurotrophic factors like NGF, BDNF, and / or CTNF throughout the 3D nerve guide, originating from the proximal and distal nerve stumps, to support vasculogenesis, axonal regeneration, axon growth and myelination. By nature, a short defect injury has a smaller distance between the two ends of the severed axon; nutrients and ancillary supportive factors, including Schwann cells, appeared to be able to provide a sufficiently robust regenerative environment to support axon development and myelination.

Our second study (15 mm lesion) produced unexpected results given the outcome of our initial experiments (10 mm lesion) using the 3D guide to reconstruct sciatic nerve lesions. The second expanded study was designed to compare and contrast the performance of our 3D design with the autologous implant, and conventional hollow core nerve guide designs. Based on functional metrics, regeneration in the motor and sensory beds was faster and more extensive in animals treated with the 3D guides with respect to the other designs in the first 30 days after surgery. Consistent with this result, the animals treated with the 3D guides had more axons in the distal nerve stump than the other treatment groups at day 45. As the study progressed, animals treated with the 3D guides continued to display evidence of functional recovery; however, our morphometric analysis indicated that the total number of myelinated axons present in the distal native tissue actually declined with respect to the other treatment groups. TEM analysis of the distal tissues suggested the continued recovery was mediated by a population small caliber, unmyelinated axons. If the extent of functional recovery that we observed in animals treated

with the 3D grafts was unprecedented, so too was the paucity of myelinated axons that we detected in the regenerated tissues.

In the second study using a long defect injury, there are several factors to consider in the analysis of our results. First, and obviously foremost, a longer defect requires the endogenous elements to travel further to provide the signals necessary to drive regeneration. In an injury, the most "effective" regenerative environment may be limited to the first few millimeters of an implant and in the immediate vicinity of the native tissues. The middle section of the 3D guides might be relatively devoid of endogenous nutrient support (i.e. diffusion barriers). Hybrid nerve guides composed of conventional hollow silicon tubes interspersed with native autologous tissue have been used to explore this potential limitation [95]**.** No specific benefits were ascribed to the hybrid nerve guide described in that study. We considered this "distance" limitation in the design of our long defect study described in Chapter 5 and developed a therapeutic reagent delivery platform that could be incorporated into our nerve guides. Unfortunately, the incorporation of NGF into our nerve guides did not appear to increase axonal outgrowth or myelination.

A second possible source of our results concerns the actual amount of "donor tissue" that is present after we have removed a 15 mm section of tissue to prepare the lesion site. Removal of this much tissue much certainly reduce the total number of endogenous Schwann cells that are present and that can contribute to the supply of endogenous factors necessary to support the development of a regenerative environment. This notion must be especially true in the distal sciatic nerve stump. With the removal of a 15 mm segment of the this nerve starting just after it has formed outside the vertebral column, the distal stump of the injured sciatic nerve left is very small in diameter and therefore essentially contains a smaller number of Schwann cells and endothelial cells to support regeneration. Shorter defect injuries have a distal stump with a much

larger volume and therefore a larger pool of cells to draw on to repopulate the lesion site. Curiously, if this was the sole factor in our reported results we would expect the hollow core designs to be subject to similar "population limitations". It may be that our 3D grafts have such a large internal surface area for cell growth that proliferating Schwann cells cannot divide sufficiently to populate this space. This argument basically states that Schwann cells continue to divide until the available surface area is occupied and could be used to explain why hollow core grafts do not seem to be subject to this population limitation.

One obvious way to address a regeneration limitation associated with a population barrier of Schwann cells is to incorporate this unique cell type directly into the graft prior to implantation. This approach has been used in the reconstruction of experimentally induced spinal cord injuries in rodents with some degree of success [60, 61]. Similar experiments in peripheral nerve injuries have generated conflicting results [96]. Our objective was to avoid the incorporation of Schwann cells in our devices; from a treatment paradigm we want to develop an off-the-shelf implant that does not require any further manipulation. We feel the incorporation exogenous Schwann cells would ultimately lead to additional regulatory barriers as we move this device into the clinical marketplace. It is also very difficult to precisely populate the 3D space of an electrospun nerve guide with a known number of cells. Our solution to the possible shortage of Schwann cells in a long defect nerve injury was to develop a method to trap therapeutic reagents, like NGF "into a thread" of alginate as detailed in Chapter 5. This platform can be used to deliver specific growth factors or mixtures of growth factors to our nerve guide environment.

In our expanded study described in Chapter 6, the functional outcomes for animals treated with 3D nerve guides supplemented with / without exogenous NGF were very similar. The trajectory of motor recovery was nearly identical over the entire time course of the study.

There was some evidence that animals treated with the 3D + NGF grafts failed to recover sensory function as quickly as the animals treated with the un-enhanced 3D nerve grafts. As discussed in Chapter 6 we have ascribed this result to the potential inhibitory effects of a relatively large and local dose of NGF during the early stages of nerve regeneration [106].

One technical aspect of the present study that distinguishes it from our initial pilot study in which we used the 10 mm lesion gap concerns the nature of the injury. At the time we did not fully appreciate the extent to which a 15 mm lesion might impinge on the overall blood supply of the rodent sciatic nerve. This nerve is nourished by a series of penetrating branches of the femoral artery. These branches reach the surface of the nerve at intervals along its length and penetrate through the epineurium to reach the deeper structures. By removing a 15 mm gap of nerve we have likely completely compromised this vascular network and believe the bulk of the blood supply is provided to the regenerating axons by arterioles present within the nerve itself that, in turn, originate from intact arterial branches still intact in sites above and below the lesion. This same condition would hold true for the autologous and hollow core grafts and should also limit regeneration in these constructs, suggesting that additional variables are impacting the regenerative environment of the 3D graft. Still, the poor state of preservation that we observed in some of our 3D nerve guides at recovery tends to support this hypothesis: perfusion fixation of intact animals is highly dependent upon an intact vascular supply. If the vascular network was marginal, the perfusion media will not adequately reach the tissue to cross link the tissue adequately for microscopic observation. This condition might also be expected to limit Schwann cell functionality and division [74] as well as the subsequent processes of axon growth and myelination [102]. Autologous grafts will at least contain a potential population of endothelial cells that can be recruited to establish a nascent vascular network and meet the metabolic

demand present within the hollow core grafts may not be sufficient to lead to the myelination defects we observed in the 3D grafts.

Finally, two other aspects of this study will require additional investigation to clarify our present reported results. We assume, in the absence of other evidence, that the number of axons present in the autologous and hollow core grafts that we have calculated by morphometric means accurately reflects the number of functional axons present in the tissue. But, it is possible that we have overestimated the number of axons present in these constructs. This could occur if the regenerating axons present in these grafts have undergone branching and or grown chaotically in such a way that we are counting the same axon more than once (axons have looped back and re-grown down the graft). Either scenario will result in an over estimation of total axon number. There are domains in the hollow core constructs where the axons are not in cross-section, suggesting they have deviated from growing exclusively down the long axis of the construct. The second issue that must be further considered concerns the overall efficiency of axon targeting to the distal tissues. If a particular graft design supports the regeneration of larger number of axons but they grow slowly or fail to properly target to the distal tissues, functional recovery will be limited due to the onset of secondary degenerative changes in the motor and sensory beds.

In conclusion: (1) the 3D nerve guide is a suitable candidate platform for the development of next generation nerve guide for the treatment of peripheral nerve injuries, (2) the regenerative environment afforded by the 3D graft will likely have to be manipulated through the addition of exogenous factors in order to drive the development of well myelinated axons. Animals treated with the 3D grafts failed to express a large number of myelinated axons in the tissues distal to the lesion site; however, they did display evidence of superior functional recovery. This enhanced functional recovery was observed despite the absence of exogenous

neurotrophic reagents or other biological cues (axon-adhesion proteins). Given that 3D grafts with and without exogenous NGF supported similar degrees of functional recovery, we argue that guidance cues provided by the unique architecture of these grafts represent the source of this result. Axons grow along the aligned fibers, or perhaps more accurately within the intrafibrillar spaces that are lined by the surrounding fibers, an architectural feature that must limit the lateral deviations of growth cones and thereby accentuate growth done the length of the graft. This would lead to more efficient axon elongation and ultimately faster growth across the lesion site.

FUTURE RESEARCH DIRECTIONS

The peripheral nervous system has a remarkable capacity to undergo regeneration; however this regenerative capacity is markedly challenged in long defect nerve injuries. Continued research will be necessary to provide for an optimized regenerative environment in this and other tissues. A more complete inventory of the various mechanisms underlying the response of the PNS to injury can be expected to lead to innovative treatment strategies to improve functional outcomes after these devastating injuries.

The 3D nerve guide developed and characterized in this study was designed to provide regenerating axons with an anisotropic environment that mimics the native tissue. The aligned fibers, and associated "aligned" intrafibrillar spaces, provide a substrate with guidance cues to direct regenerating axons to grow efficiently across a lesion site. We hypothesized that constructs designed to reduce the frequency and extent of lateral deviations that growth cones and regenerating axons take as the regeneration process takes place would serve to accelerate regeneration and improve functional outcomes. While we did observe evidence of improved functional outcomes in our rodent model of a long defect nerve injury using the sciatic nerve, this recovery appeared to be largely mediated by small caliber unmyelinated axons. This surprising result indicates that something potentially crucial is missing from our engineered regenerative environment (obliviously, additional longer term studies need to be carried out to more fully understand this process-is it a failed regenerative response or a response that was robust initially and then subsequently failed?).

Our overall objective is to develop a synthetic nerve guide that can supplant the use of the autologous nerve guide. At least in this series of preliminary studies, we have generated data to

suggest that this is possible using the strategies that we used to produce our graft. By replacing the autologous nerve guide, in addition to the eliminating the complications associated with the increased intra-operative time and donor site morbidity, we had hoped to limit the "time to regeneration" delays associated with the interval of time needed for the axonal fragments that are present in native tissue to undergo degradation. This debris must be removed before regenerating axons can penetrate into these native implants. There have been efforts to accelerate this process by physically or chemically removing this material from the donor tissue [90]; the efficacy of this approach remains to be fully demonstrated. There are limits to this approach; if the donor tissue is autologous you still cause functional deficits at the donor site. If it is sourced from cadavers there will be concerns of disease propagation and or adverse immune responses. There is consistently a shortage of donor tissues from cadavers (and living patients for that matter) nearly regardless of the tissue under consideration. This circumstance leads to potential supply issues in the marketplace. Together, these factors suggest that there is a viable market for a synthetic replacement for the autologous materials and / or donor implants regardless of their source or physical state.

Treatment regimes that accelerate axonal regeneration across the injury lesion represent an important gateway to improved functional outcomes. This is because degenerative events begin to take place within hours of nerve injury and the loss of innervation. These degenerative changes become increasingly profound over time in both motor and sensory beds [112-114]. There was clear physical evidence of this process in the lumbricals of the experimental limbs in our study; motor end plates were essentially completely lost in these muscles by day 30 after surgery. The observation that they returned to near normal appearance by day 45 indicates that all of the treatment groups had some degree of nerve restoration in these most distal muscles. A

consideration of the processes that surround regeneration in autologous tissues reveals several potential sites in which we believe that relatively simple manipulations can be used to improve the performance of our nerve guides

Myelinated and unmyelinated axons of the PNS are surrounded by Schwann cells which in turn are surrounded by basal lamina that faces the endoneurium. The Schwann cells produce and maintain the myelin sheath along the length of an axon, adjacent Schwann cells are separated from one another along the nerve by an intermodal gap, the site of the Node of Ranvier. In contrast, unmyelinated axons exhibit a continuous sheath of Schwann cells with no gaps between the adjacent cells. Thus, both the myelinated and unmyelinated axons of PNS reside within a continuous "tube" of basal lamina [101]. When the axon is severed from its cell body at injury, the distal aspect of the axon gradually degenerates and eventually disappears by the process of Wallerian degeneration. The Schwann cell, after losing contact with the underlying axon, starts to degrade the myelin associated with the remnants of the distal segments of the injured axon, leaving behind an empty tube of basal lamina. In an injury treated with an autologous graft, or at sites distal to the actual lesion gap (within the remaining in aspects of the native tissue), the regenerating axons grow into the (and in some cases onto the collapsed) hollow tubes of basal laminae and extend outward to reach the distal target tissues. Schwann cells after degrading and fragmenting the myelin, when macrophages infiltrate the tissue and begin to phagocytize the partially degraded myelin, begin to undergo proliferation and form a cell "strand" that is surrounded by the basal lamina tube, a structure called the Bands of Bungner [116]. The Bands of Bunger are considered to be an essential substrate and pathway for regenerating axons [79, 101]. If the axons fail to enter the compartment established by the Bands of Bungner or the original basal lamina, elongation ceases after only a few millimeters and a failed regenerative response takes

place. Autologous, acellular grafts take advantage of this observation and attempt to provide "hollow remnants" of these structures to support and direct the regeneration of the axons [117]. The "empty tunnels" of basal lamina in these native, yet engineered native grafts serve to provide guidance cues and a substrate for the adhesion and elongation of the regenerating axons and the migration of the Schwann cells towards the distal target organs [101]. Multiple axons can grow through these basal lamina tubes (an ultrastructural feature that we observed in tissues distal to the implant site for our 3D grafts-see TEM images Chapter 6; Figure 6.8). Subsequently and / or in parallel with the elongation of the axons they are surrounded by Schwann cells that ultimately myelinate the individual axons. Finally, investing Schwann cells produce a nascent basal laminae on the surface of the cell that faces away from the axon, and the old basal lamina is gradually degraded [99].

Of note, in this sequence of events is the observation that that regenerating axons prefer to grow through the remnants of the basal lamina and / or the Bands of Bungner formed by the Schwann cells. The common denominator in both of these supportive regenerative environments is that they both contain adhesion molecules which facilitate the formation of growth cones and the elongation of the axon. Schwann cells, in an injured peripheral nerve, express high levels of adhesion molecules from immunoglobulin superfamily (N-CAM and L1) and the cadherin superfamily (N-cadherin). Axonal adhesion to basal lamina is mediated by laminin [75, 118, 119]. Neural cell adhesion molecule (N-CAM) and L1 have been both been found to promote Schwann cell-mediated neurite outgrowth along the Bands of Bungner [99, 101, 110, 111, 116]. N-cadherin also mediates axon-Schwann cell adhesion and is strongly expressed in these attachment sites, indicating its role in the facilitation of axon outgrowth [101]. In many peripheral nerve injury cases (mostly small crush injuries) regenerating axons have been found to sprout from the proximal

stump of an injured nerve and grow into the distal basal lamina without being accompanied by the Schwann cells during the initial phases of axonal regeneration. This indicates the critical role of basal lamina in the support of axon growth. Basal lamina is rich in laminin, a glycoprotein which is a potent adhesion molecule to the integrins expressed at the growth cone of the regenerating axon [101, 120].

Considering these factors, the efficacy 3D nerve guide generated by two pole air gap electrospinning might be greatly improved by making the polymer fibers functionally active. Nerve guides fabricated from PCL at a concentration of 200 mg mL^{-1} having average fiber diameter of 1µm have proven to be highly biocompatible, exhibit low toxicity, have very high porosity (> 90% void spaces), and are biodegradable. This formulation has sufficient material properties to sustain the structures during manual manipulation and surgical placement and appear to be able to withstand crushing and or other mechanical damage once they are placed *in situ* [2, 50, 51, 121]. The addition of the external layer of PGA/PLA we used further enhances the mechanical properties of these constructs. However, PCL is a hydrophobic polymer [104]. This property must reduce and / or at least impair the early stages of axon elongation by limiting cell-fiber interactions (adhesion). The polymer itself, as a synthetic polymer, lacks physiological cell-adhesion sites [104, 122]. The absence of physiological binding sites, in addition to limiting axon-scaffold interactions, can also be expected to restrict the migration of endothelial cells and Schwann cells inside the nerve guide, events critical to stimulating and supporting axon regeneration and subsequent myelination [39]. The fibrillar structure of the electrospun 3D nerve guide mimics the macroscopic and anisotropic architecture of the native ECM present in peripheral nerve. However, manipulations that reduce the hydrophilic properties of the PCL polymer and serve to provide physiological binding sites can be used to further enhance

axon–scaffold and / or Schwann cell–scaffold interactions, thereby facilitating infiltration of regenerating axons and Schwann cells into the nerve graft.

Hybrid scaffolds can be fabricated by co-electrospinning two polymers to improve the hydrophilic nature of the scaffold and / or by directly incorporating adhesion proteins like laminin into the polymer solutions. For example, co-electrospinning natural polymers such as collagen or gelatin with PCL during electrospinning has been shown to reduce the hydrophilic nature of electrospun PCL and increase cell adhesion [104]. It is relevant to note that collagen has been used in other physical forms to fabricate nerve guides [123, 124, 125]. We elected to use PCL in the fabrication of our nerve guide, rather than electrospun collagen, to take advantage of the increased biostability of the synthetic polymer. The co-spinning of PCL with laminin is an attractive approach and should provide for a more physiologically relevant surface for Schwann cell migration and axon regeneration. One specific advantage to the co-spinning process is that it usually takes relative minute amounts (nano-gram quantities) of exogenous protein in the electrospinning solvent to enhance the biological properties of a synthetic polymer. There is excellent support in the literature for using laminin in our application; nerve regeneration in a variety of nerve guides has been enhanced with addition of the specific protein [64]. Other neurostimulatory proteins like LN-1, fibronectin and RGD domains also increase rates of axonal regeneration [126]. Thus, improving the functional capacity of the electrospun fibers present in a synthetic 3D nerve guide is a promising avenue for enhancing peripheral nerve regeneration.

Another limiting factor in the regeneration of long defect nerve injuries concerns the signaling environment afforded by growth factors. Neurotrophic factors are synthesized in target tissues and / or by the Schwann cells and these soluble factors are delivered to the nerve cell body via retrograde axonal transport [107]. Following nerve injury, disruption of the retrograde

transport of these neurotrophic factors can lead to neuronal cell death and limited regeneration. Neurotrophic factors include neurotrophins (NGF, brain derived neurotrophic factor (BDNF), NT-3, and NT-4/5), neurokines (ciliary neurotrophic factor (CNTF) and leukemia inhibitory factor (LIF)), and the transforming growth factor (TGF)-β family (TGF-β1, 2, 3) and glial cell line derived neurotrophic factor (GDNF). Exogenous administration of these trophic factors to the microenvironment of the injured nerve might compensate for the disrupted retrograde transport system. However, even a brief survey of the literature regarding the ***known*** trophic factors in the peripheral nervous system makes it clear that the native regenerative environment contains a very complex mixture of these factors. While it is theoretically possible to add any number of these reagents to a nerve graft, there is an increasing risk of immune response that is accompanied by increasing FDA regulatory burden as additional factors are added to the construct. Given these circumstances, it would seem appropriate to target very specific signaling events for enhancement by the exogenous addition of therapeutic reagents.

Key therapeutic reagents that have been examined, and show promise, and represent candidates for further investigation as therapeutic additions to our nerve guides include NGF, BDNF, CNTF, and GDNF. NGF protects sympathetic and sensory neuronal cells from injury-induced death [101, 127]. There is marked increase in the expression of this growth factor, and its receptors after axotomy [101, 116, 128]. In our studies, the incorporation of an NGF gradient along the length of our 3D nerve grafts failed to improve functional recovery beyond that observed with the un-enhanced version of this construct. One explanation for this result may lie not in the identity of the NGF, but rather in the dosages delivered and the time frame in which it is available in our constructs; optimal concentration of this factor appears to be critical [102]. BDNF expression is also up-regulated after peripheral nerve injury. It promotes survival and outgrowth

of sympathetic, sensory and motor nerves [101]. Exogenous BDNF administration has shown to improve functional recovery after peripheral nerve lesions [99, 107, 129]. CNTF is present in high levels in Schwann cells of intact adult nerves and is decreased after peripheral nerve injuries; supplementing the regenerative environment with this peptide arrests motor neuron and muscle degeneration in rodents, thereby promoting the survival of these cells following axotomy [99, 101, 107]. GDNF enhances DRG neurite elongation *in vitro* [130] and has a strong neurotrophic effect on Schwann cells [99]. It is also one of the most potent neuro-protectors of motor neurons [103].

In addition to the trophic factors, the incorporation of biological cues, such as Schwann cells and / or neural stem cells might also be used to enhance the efficacy of the 3D nerve guide design [50]. As noted, Schwann cells mediate myelination and express a variety of trophic factors, and axon adhesion molecules, including laminin, fibronectin, heparan sulfate proteoglycans, and tenascin [99, 101]. By providing this cell population, it may be possible to completely negate the need of for the addition of exogenous growth factors and / or other reagents. The caveat to this approach concerns identifying the source of the Schwann cells to be used and the associated regulatory hurdles imposed when cell-based therapies are considered.

Given our observation that our guides appear to develop a deficient vascular network, it is reasonable to propose to add VEGF (vascular endothelial growth factor) to our constructs. This peptide drives intraneural neo-vasculogenesis [131] and has neuro-protective effects above and beyond any therapeutic benefits associated with increased vascular development [132]. This makes this particular peptide a very attractive choice for further investigation. Poor vascular perfusion in our grafts may represent a key limiting factor in our regenerative environment.

Emergent science in the cell biology of peripheral nerve can be expected to provide new avenues for the treatment of nerve injury. We believe that efforts should be concentrated on

developing methods to accelerate axon regeneration and elongation across the lesion site. To this end, there are several much focused areas of interest for future investigation. For example, the addition of a physiologically relevant surface to the PCL fibers, in the guise of laminin, can be expected to enhance the performance of our basic nerve guide design. As noted, VEGF represents a very attractive candidate that may serve to address multiple regenerative barriers. We have not explored the use of chondroitinase ABC (chABC) as a supplement in this study. There is evidence from our morphometric study that axons penetrate into the fiber arrays of our 3D guides slowly during the early stages of regeneration (Chapter 6, Figure 6.7 G, J). This may be a consequence of growth inhibitory chondroitin sulfate proteoglycans (CSPGs) that accumulate in response to nerve injury [133]. Treating the vicinity of nerve injuries, over relatively short intervals of time (days) with the enzyme chondroitinase ABC has been shown to reduce the burden of these inhibitory factors and accelerate the onset of peripheral nerve regeneration. The acute nature of the time course needed to effectively administer this enzyme to an injury site makes it amenable for use in our alginate platform. Adjunct therapies designed to spare the distal tissues until they are re-innervated provide a secondary therapeutic target that can be exploited to improve functional outcomes. The electrospinning process and the nature of our novel 3D nerve guide make it possible to incorporate multiple and synergistic structural, biochemical, and / or cellular cues into these constructs to modulate the regenerative environment and maximize functional recovery.

LITERATURE CITED

LITERATURE CITED

1. Jha BS, Ayres CE, Bowman JR, et al. Electrospun collagen: A tissue engineering scaffold with unique functional properties in a wide variety of applications. *Journal of Nanomaterials*. Vol 2011, Article ID 348268, 15 pages, 2011. doi:10.1155/2011/348268.

2. Jha BS, Colello RJ, Bowman JR, et al. Two pole air gap electrospinning: Fabrication of highly aligned, three-dimensional scaffolds for nerve reconstruction. *Acta Biomater*. 2011;7:203-215.

3. Doshi J, Reneker DH. Electrospinning process and applications of electrospun fibers. *J Electrostatics*. 1995;35:151-160.

4. Matthews JA, Wnek GE, Simpson DG, Bowlin GL. Electrospinning of collagen nanofibers. *Biomacromolecules*. 2002;3:232-238.

5. Ayres CA, Jha SB, Sell SA, Bowlin GL, Simpson DG. Nanotechnology in the design of soft tissue scaffolds: Innovations in structure and function. *Nanomedicine and Nanobiotechnology.* 2009.

6. Ayres C, Bowlin GL, Henderson SC, et al. Modulation of anisotropy in electrospun tissue-engineering scaffolds: Analysis of fiber alignment by the fast fourier transform. *Biomaterials*. 2006/11;27:5524-5534.

7. Li D, Xia Y. Electrospinning of nanofibers: Reinventing the wheel? *Adv Mater*. 2004;16:1151-1170.

8. Taylor G. Electrically driven jets. *Proceedings of the Royal Society of London A Mathematical and Physical Sciences*. 1969;313:453-475.

9. Reneker DH, Yarin AL. Electrospinning jets and polymer nanofibers. *Polymer*. 2008;49:2387-2425.

10. Ayres C, Bowlin GL, Henderson SC, et al. Modulation of anisotropy in electrospun tissue-engineering scaffolds: Analysis of fiber alignment by the fast fourier transform. *Biomaterials*. 2006;27:5524-5534.

11. Ayres CE, Bowlin GL, Pizinger R, Taylor LT, Keen CA, Simpson DG. Incremental changes in anisotropy induce incremental changes in the material properties of electrospun scaffolds. *Acta Biomaterialia*. 2007;3:651-661.

12. Fong H, Chun I, Reneker DH. Beaded nanofibers formed during electrospinning. *Polymer*. 1999;40:4585-4592.

13. McClure MJ, Sell SA, Ayres CE, Simpson DG, Bowlin GL. Electrospinning-aligned and random polydioxanone-polycaprolactone-silk fibroin-blended scaffolds: Geometry for a vascular matrix. *Biomed Mater*. 2009;4:055010.

14. Ayres CE, Jha BS, Meredith H, et al. Measuring fiber alignment in electrospun scaffolds: A user's guide to the 2D fast fourier transform approach. *J Biomater Sci Polym Ed*. 2008;19:603-621.

15. Catherine P Barnes, Matthew J Smith, Gary L Bowlin, Scott A Sell, Tang Teresa, Jamil A Matthews, Jared C. Nimtz, David G Simpson. Feasibility of electrospinning the globular proteins hemoglobin and myoglobin. *Journal of Engineered Fibers and Fabrics*. 2006;1:16-28.

16. McManus M, Boland E, Sell S, et al. Electrospun nanofibre fibrinogen for urinary tract tissue reconstruction. *Biomed Mater*. 2007;2:257-262.

17. Rothwell SW, Sawyer E, Dorsey J, et al. Wound healing and the immune response in swine treated with a hemostatic bandage composed of salmon thrombin and fibrinogen. *J Mater Sci Mater Med*. 2009;20:2155-2166.

18. Boland ED, Coleman BD, Barnes CP, Simpson DG, Wnek GE, Bowlin GL. Electrospinning polydioxanone for biomedical applications. *Acta Biomater*. 2005;1:115-123.

19. Telemeco TA, Ayres C, Bowlin GL, et al. Regulation of cellular infiltration into tissue engineering scaffolds composed of submicron diameter fibrils produced by electrospinning. *Acta Biomaterialia*. 2005;1:377-385.

20. Sell SA, McClure MJ, Barnes CP, et al. Electrospun polydioxanone-elastin blends: Potential for bioresorbable vascular grafts. *Biomed Mater*. 2006;1:72-80.

21. Newton D, Mahajan R, Ayres C, Bowman JR, Bowlin GL, Simpson DG. Regulation of material properties in electrospun scaffolds: Role of cross-linking and fiber tertiary structure. *Acta Biomaterialia*. 2009;5:518-529.

22. Zeugolis DI, Khew ST, Yew ESY, et al. Electro-spinning of pure collagen nano-fibres – just an expensive way to make gelatin? *Biomaterials*. 2008;29:2293-2305.

23. Heydarkhan-Hagvall S, Schenke-Layland K, Dhanasopon AP, et al. Three-dimensional electrospun ECM-based hybrid scaffolds for cardiovascular tissue engineering. *Biomaterials*. 2008;29:2907-2914.

24. Yang L, Fitié CFC, van der Werf KO, Bennink ML, Dijkstra PJ, Feijen J. Mechanical properties of single electrospun collagen type I fibers. *Biomaterials*. 2008;29:955-962.

25. Simpson DG, Terracio L, Terracio M, Price RL, Turner DC, Borg TK. Modulation of cardiac myocyte phenotype *in vitro* by the composition and orientation of the extracellular matrix. *J Cell Physiol*. 1994;161:89-105.

26. Manis AE, Bowman JR, Bowlin GL, Simpson DG. Electrospun nitrocellulose and nylon: Design and fabrication of novel high performance platforms for protein blotting applications. *J Biol Eng*. 2007;1:2.

27. Weiner S, Traub W. Organization of hydroxyapatite crystals within collagen fibrils. *FEBS Lett*. 1986;206:262-266.

28. I. V. Yannas. Regeneration templates. In: *The Biomedical Engineering Handbook.* Vol 113. Boca Raton: CRC Press; 2000:1-18.

29. Agrez MV, Bates RC, Boyd AW, Burns GF. Arg-gly-asp-containing peptides expose novel collagen receptors on fibroblasts: Implications for wound healing. *Cell Regul*. 1991;2:1035-1044.

30. Davis GE. Affinity of integrins for damaged extracellular matrix: Avβ3 binds to denatured collagen type I through RGD sites. *Biochem Biophys Res Commun*. 1992;182:1025-1031.

31. Cisneros DA, Hung C, Franz CM, Muller DJ. Observing growth steps of collagen self-assembly by time-lapse high-resolution atomic force microscopy. *J Struct Biol*. 2006;154:232-245.

32. Stevens KR, Einerson NJ, Burmania JA, Kao WJ. *In vivo* biocompatibility of gelatin-based hydrogels and interpenetrating networks. *J Biomater Sci Polym Ed*. 2002;13:1353-1366.

33. Chen ZL, Yu WM, Strickland S. Peripheral regeneration. *Annu Rev Neurosci*. 2007;30:209-233.

34. Dubovy P. Schwann cells and endoneurial extracellular matrix molecules as potential cues for sorting of regenerated axons: A review. *Anat Sci Int*. 2004;79:198-208.

35. Lykissas MG, Batistatou AK, Charalabopoulos KA, Beris AE. The role of neurotrophins in axonal growth, guidance, and regeneration. *Curr Neurovasc Res*. 2007;4:143-151.

36. Ichihara S, Inada Y, Nakamura T. Artificial nerve tubes and their application for repair of peripheral nerve injury: An update of current concepts. *Injury*. 2008;39:29-39.

37. Johnson EO, Soucacos PN. Nerve repair: Experimental and clinical evaluation of biodegradable artificial nerve guides. *Injury*. 2008;39:30-36.

38. Battiston B, Geuna S, Ferrero M, Tos P. Nerve repair by means of tubulization: Literature review and personal clinical experience comparing biological and synthetic conduits for sensory nerve repair. *Microsurgery*. 2005;25:258-267.

39. Lundborg G, Dahlin LB, Danielsen N, et al. Nerve regeneration in silicone chambers: Influence of gap length and of distal stump components. *Exp Neurol*. 1982;76:361-375.

40. Utley DS, Lewin SL, Cheng ET, Verity AN, Sierra D, Terris DJ. Brain-derived neurotrophic factor and collagen tubulization enhance functional recovery after peripheral nerve transection and repair. *Arch Otolaryngol Head Neck Surg*. 1996;122:407-413.

41. Bellamkonda RV. Peripheral nerve regeneration: An opinion on channels, scaffolds and anisotropy. *Biomaterials*. 2006;27:3515-3518.

42. Chow WN, Simpson DG, Bigbee JW, Colello RJ. Evaluating neuronal and glial growth on electrospun polarized matrices: Bridging the gap in percussive spinal cord injuries. *Neuron Glia Biol*. 2007;3:119-126.

43. Corey JM, Lin DY, Mycek KB, et al. Aligned electrospun nanofibers specify the direction of dorsal root ganglia neurite growth. *J Biomed Mater Res A*. 2007;83:636-645.

44. Wang HB, Mullins ME, Cregg JM, et al. Creation of highly aligned electrospun poly-L-lactic acid fibers for nerve regeneration applications. *J Neural Eng*. 2009;6:016001.

45. Schnell E, Klinkhammer K, Balzer S, et al. Guidance of glial cell migration and axonal growth on electrospun nanofibers of poly-ε-caprolactone and a collagen/poly-ε-caprolactone blend. *Biomaterials*. 2007;28:3012-3025.

46. Ayres C, Bowlin GL, Henderson SC, et al. Modulation of anisotropy in electrospun tissue-engineering scaffolds: Analysis of fiber alignment by the fast fourier transform. *Biomaterials*. 2006;27:5524-5534.

47. Ayres CE, Bowlin GL, Pizinger R, Taylor LT, Keen CA, Simpson DG. Incremental changes in anisotropy induce incremental changes in the material properties of electrospun scaffolds. *Acta Biomaterialia*. 2007;3:651-661.

48. Newton D, Mahajan R, Ayres C, Bowman JR, Bowlin GL, Simpson DG. Regulation of material properties in electrospun scaffolds: Role of cross-linking and fiber tertiary structure. *Acta Biomaterialia*. 2009;5:518-529.

49. Telemeco TA, Ayres C, Bowlin GL, et al. Regulation of cellular infiltration into tissue engineering scaffolds composed of submicron diameter fibrils produced by electrospinning. *Acta Biomaterialia*. 2005;1:377-385.

50. Panseri S, Cunha C, Lowery J, et al. Electrospun micro- and nanofiber tubes for functional nervous regeneration in sciatic nerve transections. *BMC Biotechnology*. 2008;8:39.

51. Sun H, Mei L, Song C, Cui X, Wang P. The *in vivo* degradation, absorption and excretion of PCL-based implant. *Biomaterials*. 2006;27:1735-1740.

52. Pham QP, Sharma U, Mikos AG. Electrospun poly(epsilon-caprolactone) microfiber and multilayer nanofiber/microfiber scaffolds: Characterization of scaffolds and measurement of cellular infiltration. *Biomacromolecules*. 2006;7:2796-2805.

53. Dupree JL, Bigbee JW. Retardation of neuritic outgrowth and cytoskeletal changes accompany acetylcholinesterase inhibitor treatment in cultured rat dorsal root ganglion neurons. *J Neurosci Res*. 1994;39:567-575.

54. Sharma KV, Bigbee JW. Acetylcholinesterase antibody treatment results in neurite detachment and reduced outgrowth from cultured neurons: Further evidence for a cell adhesive role for neuronal acetylcholinesterase. *J Neurosci Res*. 1998;53:454-464.

55. Shenoy SL, Bates WD, Frisch HL, Wnek GE. Role of chain entanglements on fiber formation during electrospinning of polymer solutions: Good solvent, non-specific polymer–polymer interaction limit. *Polymer*. 2005;46:3372-3384.

56. Abrams RA, Butler JM, Bodine-Fowler S, Botte MJ. Tensile properties of the neurorrhaphy site in the rat sciatic nerve. *J Hand Surg*. 1998;23:465-470.

57. Stang F, Fansa H, Wolf G, Reppin M, Keilhoff G. Structural parameters of collagen nerve grafts influence peripheral nerve regeneration. *Biomaterials*. 2005;26:3083-3091.

58. Schmalbruch H. Fiber composition of the rat sciatic nerve. *Anat Rec*. 1986;215:71-81.

59. Johnson J, Nowicki MO, Lee CH, et al. Quantitative analysis of complex glioma cell migration on electrospun polycaprolactone using time-lapse microscopy. *Tissue Engineering Part C: Methods*. ;0.

60. Bunge MB. Novel combination strategies to repair the injured mammalian spinal cord. *J Spinal Cord Med*. 2008;31:262-269.

61. Bunge MB. Book review: Bridging areas of injury in the spinal cord. *Neuroscientist*. 2001;7:325-339.

62. Simpson DG. Dermal templates and the wound-healing paradigm: The promise of tissue regeneration. *Expert Rev Med Devices*. 2006;3:471-484.

63. Shah M, Foreman DM, Ferguson MW. Neutralisation of TGF-beta 1 and TGF-beta 2 or exogenous addition of TGF-beta 3 to cutaneous rat wounds reduces scarring. *J Cell Sci*. 1995;108 (Pt 3):985-1002.

64. Dodla MC, Bellamkonda RV. Differences between the effect of anisotropic and isotropic laminin and nerve growth factor presenting scaffolds on nerve regeneration across long peripheral nerve gaps. *Biomaterials*. 2008;29:33-46.

65. Wang N, Adams G, Buttery L, Falcone FH, Stolnik S. Alginate encapsulation technology supports embryonic stem cells differentiation into insulin-producing cells. *J Biotechnol*. 2009;144:304-312.

66. Tonnesen HH, Karlsen J. Alginate in drug delivery systems. *Drug Dev Ind Pharm*. 2002;28:621-630.

67. Kim YJ, Park HG, Yang YL, Yoon Y, Kim S, Oh E. Multifunctional drug delivery system using starch-alginate beads for controlled release. *Biol Pharm Bull*. 2005;28:394-397.

68. Ciofani G, Raffa V, Menciassi A, Micera S, Dario P. A drug delivery system based on alginate microspheres: Mass-transport test and *in vitro* validation. *Biomed Microdevices*. 2007;9:395-403.

69. Sun AM, O'Shea GM. Microencapsulation of living cells — A long-term delivery system. *J Controlled Release*. 1985;2:137-141.

70. Gombotz WR, Wee S. Protein release from alginate matrices. *Adv Drug Deliv Rev*. 1998;31:267-285.

71. Maysinger D, Jalsenjak I, Cuello AC. Microencapsulated nerve growth factor: Effects on the forebrain neurons following devascularizing cortical lesions. *Neurosci Lett*. 1992;140:71-74.

72. Sofroniew MV, Howe CL, Mobley WC. Nerve growth factor signaling, neuroprotection, and neural repair. *Annu Rev Neurosci*. 2001;24:1217-1281.

73. Lindsay R. Nerve growth factors (NGF, BDNF) enhance axonal regeneration but are not required for survival of adult sensory neurons. *The Journal of Neuroscience*. 1988;8:2394-2405.

74. Liu J, Wang C, Wang J, Ruan H, Fan C. Peripheral nerve regeneration using composite poly(lactic acid-caprolactone)/nerve growth factor conduits prepared by coaxial electrospinning. *Journal of Biomedical Materials Research Part A*. 2011;96A:13-20.

75. Adams DN, Kao EY-, Hypolite CL, Distefano MD, Hu W, Letourneau PC. Growth cones turn and migrate up an immobilized gradient of the laminin IKVAV peptide. *J Neurobiol*. 2005;62:134-147.

76. Jaquet JB, Luijsterburg AJ, Kalmijn S, Kuypers PD, Hofman A, Hovius SE. Median, ulnar, and combined median-ulnar nerve injuries: Functional outcome and return to productivity. *J Trauma*. 2001;51:687-692.

77. Daoutis NK, Gerostathopoulos NE, Efstathopoulos DG, Misitizis DP, Bouchlis GN, Anagnostou SK. Microsurgical reconstruction of large nerve defects using autologous nerve grafts. *Microsurgery*. 1994;15:502-505.

78. Battiston B, Geuna S, Ferrero M, Tos P. Nerve repair by means of tubulization: Literature review and personal clinical experience comparing biological and synthetic conduits for sensory nerve repair. *Microsurgery*. 2005;25:258-267.

79. Kim Y, Haftel VK, Kumar S, Bellamkonda RV. The role of aligned polymer fiber-based constructs in the bridging of long peripheral nerve gaps. *Biomaterials*. 2008;29:3117-3127.

80. Zuo J, Hernandez YJ, Muir D. Chondroitin sulfate proteoglycan with neurite-inhibiting activity is up-regulated following peripheral nerve injury. *J Neurobiol*. 1998;34:41-54.

81. Stroncek JD, Reichert WM. Overview of wound healing in different tissue types. In: Reichert WM, ed. *Indwelling Neural Implants: Strategies for Contending with the in vivo Environment.* Boca Raton (FL): Taylor & Francis Group, LLC; 2008.

82. Laskowski MB, Olson WH, Dettbarn W. Initial ultrastructural abnormalities at the motor end plate produced by a cholinesterase inhibitor. *Exp Neurol*. 1977;57:13-33.

83. Reynolds ML, Woolf CJ. Terminal schwann cells elaborate extensive processes following denervation of the motor endplate. *J Neurocytol*. 1992;21:50-66.

84. Miledi R, Slater CR. Electrophysiology and electron-microscopy of rat neuromuscular junctions after nerve degeneration. *Proc R Soc Lond B Biol Sci*. 1968;169:289-306.

85. Pellegrino C, Franzini C. An electron microscope study of denervation atrophy in red and white skeletal muscle fibers. *J Cell Biol*. 1963;17:327-349.

86. Hoffer JA, Stein RB, Gordon T. Differential atrophy of sensory and motor fibers following section of cat peripheral nerves. *Brain Res*. 1979;178:347-361.

87. Tidball JG, Quan DM. Modifications in myotendinous junction structure following denervation. *Acta Neuropathol*. 1992;84:135-140.

88. Pulliam DL, April EW. Degenerative changes at the neuromuscular junctions of red, white and intermediate muscle fibers. part 1. response to short stump nerve section. *J Neurol Sci*. 1979;43:205-222.

89. Fox MA, Sanes JR, Borza DB, et al. Distinct target-derived signals organize formation, maturation, and maintenance of motor nerve terminals. *Cell*. 2007;129:179-193.

90. Mackinnon SE, Doolabh VB, Novak CB, Trulock EP. Clinical outcome following nerve allograft transplantation. *Plast Reconstr Surg*. 2001;107:1419-1429.

91. Tung TH, Novak CB, Mackinnon SE. Nerve transfers to the biceps and brachialis branches to improve elbow flexion strength after brachial plexus injuries. *J Neurosurg*. 2003;98:313-318.

92. Bain JR, Mackinnon SE, Hunter DA. Functional evaluation of complete sciatic, peroneal, and posterior tibial nerve lesions in the rat. *Plast Reconstr Surg.* 1989;83(1):129-38.

93. Whitlock EL, Tuffaha SH, Luciano JP, et al. Processed allografts and type I collagen conduits for repair of peripheral nerve gaps. *Muscle Nerve*. 2009;39:787-799.

94. Meek MF, van der Werff JF, Klok F, Robinson PH, Nicolai JP, Gramsbergen A. Functional nerve recovery after bridging a 15 mm gap in rat sciatic nerve with a biodegradable nerve guide. *Scand J Plast Reconstr Surg Hand Surg*. 2003;37:258-265.

95. Francel PC, Francel TJ, Mackinnon SE, Hertl C. Enhancing nerve regeneration across a silicone tube conduit by using interposed short-segment nerve grafts. *J Neurosurg*. 1997;87:887-892.

96. Ansselin AD, Fink T, Davey DF. Peripheral nerve regeneration through nerve guides seeded with adult schwann cells. *Neuropathol Appl Neurobiol*. 1997;23:387-398.

97. Mohammadi R, Azizi S, Delirezh N, Hobbenaghi R, Amini K. Functional recovery of sciatic nerve through inside-out vein graft in rats. *Chin J Traumatol*. 2011;14:46-52.

98. Keymer JE, Gaete J, Kameid G, Alvarez J. Acetylcholinesterase and inhibitors: Effects upon normal and regenerating nerves of the rat. *Eur J Neurosci*. 1999;11:1049-1057.

99. Frostick SP, Yin Q, Kemp GJ. Schwann cells, neurotrophic factors, and peripheral nerve regeneration. *Microsurgery*. 1998;18:397-405.

100. Radtke C, Vogt PM. Peripheral nerve regeneration: A current perspective. *Eplasty*. 2009;9:e47.

101. Chizuka I. Peripheral nerve regeneration. *Neurosci Res*. 1996;25:101-121.

102. Chang CJ. Effects of nerve growth factor from genipin-crosslinked gelatin in polycaprolactone conduit on peripheral nerve regeneration--*in vitro* and *in vivo*. *J Biomed Mater Res A*. 2009;91:586-596.

103. Madduri S, Gander B. Schwann cell delivery of neurotrophic factors for peripheral nerve regeneration. *Journal of the Peripheral Nervous System*. 2010;15:93-103.

104. Ghasemi-Mobarakeh L, Prabhakaran MP, Morshed M, Nasr-Esfahani M, Ramakrishna S. Electrospun poly(ε-caprolactone)/gelatin nanofibrous scaffolds for nerve tissue engineering. *Biomaterials*. 2008;29:4532-4539.

105. Gallo G, Lefcort FB, Letourneau PC. The trkA receptor mediates growth cone turning toward a localized source of nerve growth factor. *The Journal of Neuroscience*. 1997;17:5445-5454.

106. B.G G. Axonal regeneration of sensory nerves is delayed by continuous intrathecal infusion of nerve growth factor. *Neuroscience*. 1997;76:1153-1158.

107. Terenghi G. Peripheral nerve regeneration and neurotrophic factors. *J Anat*. 1999;194:1-14.

108. Langer R, Vacanti J. Tissue engineering. *Science*. 1993;260:920-926.

109. Murugan R, Ramakrishna S. Nano-featured scaffolds for tissue engineering: A review of spinning methodologies. *Tissue Eng*. 2006;12:435-447.

110. Taniuchi M, Clark H, Schweitzer J, Johnson E. Expression of nerve growth factor receptors by schwann cells of axotomized peripheral nerves: Ultrastructural location, suppression by axonal contact, and binding properties. *The Journal of Neuroscience*. 1988;8:664-681.

111. Seilheimer B, Schachner M. Studies of adhesion molecules mediating interactions between cells of peripheral nervous system indicate a major role for L1 in mediating sensory neuron growth on schwann cells in culture. *The Journal of Cell Biology*. 1988;107:341-351.

112. Navarro X, Vivó M, Valero-Cabré A. Neural plasticity after peripheral nerve injury and regeneration. *Prog Neurobiol*. 2007;82:163-201.

113. Lee SK, Wolfe SW. Peripheral nerve injury and repair. *Journal of the American Academy of Orthopaedic Surgeons*. July/August 2000;8:243-252.

114. Hodges P, Holm AK, Hansson T, Holm S. Rapid atrophy of the lumbar multifidus follows experimental disc or nerve root injury. *Spine (Phila Pa 1976)*. 2006;31:2926-2933.

115. Pettersson J, McGrath A, Kalbermatten DF, et al. Muscle recovery after repair of short and long peripheral nerve gaps using fibrin conduits. *Neurosci Lett*. 2011;500:41-46.

116. Stoll G, Müller HW. Nerve injury, axonal degeneration and neural regeneration: Basic insights. *Brain Pathology*. 1999;9:313-325.

117. Moore AM, Macewan M, Santosa KB, et al. Acellular nerve allografts in peripheral nerve regeneration: A comparative study. *Muscle Nerve*. 2011;44:221-234.

118. Bixby JL, Harris WA. Molecular mechanisms of axon growth and guidance. *Annu Rev Cell Biol*. 1991;7:117-159.

119. Letourneau P, Condic M, Snow D. Interactions of developing neurons with the extracellular matrix. *The Journal of Neuroscience*. 1994;14:915-928.

120. Zhou F, Snider WD. Intracellular control of developmental and regenerative axon growth. *Philosophical Transactions of the Royal Society B: Biological Sciences*. 2006;361:1575-1592.

121. Sinha VR, Bansal K, Kaushik R, Kumria R, Trehan A. Poly-ϵ-caprolactone microspheres and nanospheres: An overview. *Int J Pharm*. 2004;278:1-23.

122. Kim CH, Khil MS, Kim HY, Lee HU, Jahng KY. An improved hydrophilicity via electrospinning for enhanced cell attachment and proliferation. *Journal of Biomedical Materials Research Part B: Applied Biomaterials*. 2006;78B:283-290.

123. Archibald SJ, Krarup C, Shefner J, Li S, Madison RD. A collagen-based nerve guide conduit for peripheral nerve repair: An electrophysiological study of nerve regeneration in rodents and nonhuman primates. *J Comp Neurol*. 1991;306:685-696.

124. Archibald S, Shefner J, Krarup C, Madison R. Monkey median nerve repaired by nerve graft or collagen nerve guide tube. *The Journal of Neuroscience*. 1995;15:4109-4123.

125. Ceballos D, Navarro X, Dubey N, Wendelschafer-Crabb G, Kennedy WR, Tranquillo RT. Magnetically aligned collagen gel filling a collagen nerve guide improves peripheral nerve regeneration. *Exp Neurol*. 1999;158:290-300.

126. Tountas CP, Bergman RA, Lewis TW, Stone HE, Pyrek JD, Mendenhall HV. A comparison of peripheral nerve repair using an absorbable tubulization device and conventional suture in primates. *J Appl Biomater*. 1993;4:261-268.

127. Otto D, Unsicker K, Grothe C. Pharmacological effects of nerve growth factor and fibroblast growth factor applied to the transectioned sciatic nerve on neuron death in adult rat dorsal root ganglia. *Neurosci Lett*. 1987;83:156-160.

128. Snider WD, Zhou FQ, Zhong J, Markus A. Signaling the pathway to regeneration. *Neuron*. 2002;35:13-16.

129. Utley DS, Lewin SL, Cheng ET, Verity AN, Sierra D, Terris DJ. Brain-derived neurotrophic factor and collagen tubulization enhance functional recovery after peripheral nerve transection and repair. *Arch Otolaryngol Head Neck Surg*. 1996;122:407-413.

130. Madduri S, Papaloïzos M, Gander B. Synergistic effect of GDNF and NGF on axonal branching and elongation *in vitro*. *Neurosci Res*. 2009;65:88-97.

131. Hobson MI, Green CJ, Terenghi G. VEGF enhances intraneural angiogenesis and improves nerve regeneration after axotomy. *J Anat*. 2000;197:591-605.

132. Rosenstein JM, Krum JM. New roles for VEGF in nervous tissue—beyond blood vessels. *Exp Neurol*. 2004;187:246-253.

133. Udina E, Gold BG, Navarro X. Comparison of continuous and discontinuous FK506 administration on autograft or allograft repair of sciatic nerve resection. *Muscle Nerve*. 2004;29:812-822.

VITA

Balendu Shekhar Jha was born in Bihar, India on January 26, 1981. He was raised in New Delhi, India and graduated from Delhi Public School, R. K. Puram in 1998. He attended Delhi University where he was awarded his Bachelors of Science (Hons.) degree in Physical Therapy in 2003. Thereafter, he completed one year course of Bachelors of Science (Hons.) Physical Therapy – Bridge course at Delhi University from 2004 – 2005. In August 2005, he began his graduate work at Virginia Commonwealth University, where he pursued his doctoral degree in Anatomy and Neurobiology. He currently resides in Richmond, VA with his wife Vandana Jha.